Ultrafast properties of plasmonic nanorod metamaterial

Peruch, Silvia

Awarding institution:
King's College London

King's College London

Doctoral Thesis

Ultrafast properties of plasmonic nanorod metamaterials

Author:
Silvia Peruch MSci (Hons)

Supervisor:
Professor Anatoly Zayats

Thesis submitted for the degree of
Doctor of Philosophy (PhD)

in the

Experimental Biophysics and Nanotechnology group
Department of Physics

September 2015

Abstract

Plasmonic metamaterials have customized linear and nonlinear optical properties. This thesis investigates the properties of an anisotropic plasmonic metamaterial, consisting of aligned, interacting gold nanorods, to perform ultrafast light modulation, exploiting the intrinsic Kerr nonlinearity of gold. This effect is based on an illumination-intensity-dependent change in the gold's permittivity, which takes place on ultrafast timescales and induces the intensity-dependent change of the metamaterial's reflection and transmission. A comprehensive theoretical and numerical analysis of the linear and nonlinear response of various configurations of the metamaterial is performed and compared to experimental results. A new family of hyperbolic waveguided modes above the effective plasma frequency, enabled by spatial dispersion, is identified. The strong nonlinear response and the dynamic modulation capabilities associated with the excitation of the waveguided modes is investigated. The presence of strong electron temperature gradients in the nanorods induced by a control light is shown to determine a stronger nonlinear modulation and to influence the dynamic response, leading to subpicosecond time recovery components of the nonlinearity. Weak and strong coupling between molecular excitons and the metamaterial's modes can be achieved using core-shell nanorod geometries. The coherent interaction of molecular J-aggregates with core-shell nanorod arrays is analyzed in both the weak and strong coupling regimes. Subpicosecond components of the modulation are determined in the strong coupling conditions. The design of the optical response of the gold nanorod and core-shell metamaterials is studied through the near- to mid- Infrared, key spectral regions for molecular fingerprinting in chemical sensing and absorption spectroscopy. The applicability limits of the analytic approaches using the quasi-static and effective medium approximations is tested. The results show great potential of the plasmonic nanorod metamaterial for ultrafast nonlinear optics in free-space and integrated applications, in a broad spectral range.

Acknowledgements

I am very thankful to my supervisor, Professor Anatoly Zayats, for the opportunity he gave me to work at this project and his guidance. I am also very thankful to my second supervisor, Dr. Gergory Wurtz, for his constant support.

I am grateful to all the members of the plasmonics group, in particular Dr. Mazhar Nasir, for sharing his exceptional fabrication expertise with me, Dr. Wayne Dickson and Dr. Jean-Sebastian Bouillard.

I am grateful to my family, and to all the caring people that have been with me throughout these years, Alberto, Andres, Angela, Cillian, Davide, Giovanni, Paolo, Vanessa.

I am especially grateful to Claudia and Charles, who would have loved to share this moment with me.

For Claudia and Charles

Contents

List of Figures

Chapter 1

Introduction

Lightwave communication has undoubtably emerged in the last 50 years as one of the most valuable technology able to sustain a constantly increasing data transmission and processing capacity.

Information travels in the form of light through optical fibers, which are probably the most widespread adopted optical devices. Their basic structure consists of a high refractive index material core and a slightly smaller refractive index material cladding, allowing total internal reflection to occur at the walls of the inner constituent. Light can thus be confined inside the core and advances through a sequence of successive reflections [1].

Total internal reflection was first observed in 1842, when Jean-Daniel Colladon managed to guide light inside a curving stream of water as a visual aid for his experiments on fluid dynamics [2]. In Colladon's demonstration, water is the high refractive index medium, cladded by the lower refractive index air of the environment. Optical fibers of sufficient quality to be of practical use are a relatively recent invention, dating to the 1960s. One of the first reported use of low-loss fibre bundles was for imaging for medical purposes [3].

Optical fibers are unrivalled for covering large scale data transmission, being able to mantain the signal integrity and having theoretically unlimited bandwidth. They are in fact passive devices, i.e. they do not modify the optical wave travelling through them. Once the wavevector matches the requirements to undergo total internal reflection, the correspondent electromagnetic wave will not be modified.

For single mode fibers, used for most high speed optical networks, a limit to the distance that the wave can travel without significant distorsions is given by chromatic dispersion, that determines a broadening of the optical pulses. The typical node distance in Europe for a 10 Gbit s^{-1} transmission at 1.55 μm is around 60 km. Optical dispersion compensator fibers can then be employed.

A small amount of losses has always to be considered. The clearest optical fibers can transmit signals more than 100 km without amplification [4], much farther than copper wires. Optical amplifiers in the form of erbium-doped fibers are used to compensate for attenuation. The optical energy injected by the amplifier comes from an external laser pump, which is absorbed and subsequently re-emitted by the erbium atoms. With careful control, a string of dozens of optical fiber amplifiers can transmit signals thousands of kilometers across the ocean [4].

In order to maximize the amount of data transmitted, many separate signals have to be transferred simultaneously at different wavelengths, a technique called wavelength-division multiplexing. A certain total bandwidth, the total spectrum available, will be divided between the different channels. Multiplying the number of optical channels by the data transmission rate on each optical channel gives the total transmission capacity of a fiber.

Hollow-core fibers have shown a transmission of 37x40 Gbit s^{-1} channels, with loss of 3.5 dB km^{-1} and bandwidth of 160 nm, with a latency of only 1.54 μs km^{-1} [5]. However, commercial transmission rates typically do not exceed a few hundred Gbit s^{-1}. This transmission rate is anyway several orders of magnitude higher than that achievable with a copper cable [6].

The fundamental limit of optical fibers is determined by the fact that they cannot be miniaturized to less than half the size of the wavelength, the so-called diffraction limit. Thus, they cannot be adapted to the ultrahigh density integrated circuits in the short-scale data manipulation.

This drawback can be minimized by employing high refractive index materials, which can confine light over a volume with a characteristic size of λ/n, where n is the real part of the refractive index of the material used, usually a dielectric. Silicon photonics is in fact a well developed technology for short scale interconnections in

the telecom spectral window, around 1.55 μm, where losses of silicon are negligible and the real part of its refractive index is 3.48 [7]. A single-mode waveguide at 1.55 μm can have a diameter of only 450 nm. Moreover, fabrication techniques and instrumentation belonging to CMOS technology can be equivalently employed for the realization of silicon based optical chips [8]. Companies such as Intel and IBM have realized silicon optical chips able to achieve transfer bit rates in the order of 1 Tbit s^{-1} [9, 10]. Still, integrable silicon components cannot fit in a chip with a typical pitch of the order of 100 μm^2, that would normally allocate billions of electronic transistors. Furthermore, according to Moore's law [11], the number of transitors in an integrated circuit approximately doubles every two years.

All-optical signal processing would certainly offer numerous advantages also for the small scale transmission. It would allow to overcome some major issues deriving from the high density of electrical transistors and interconnect wires in integrated circuits, in particular the increase of resistance and capacitance and consequently of the delay time of electronic circuits. The RC time delay, product of the total resistance and total capacitance of an interconnect, is the time for the voltage at one end of a metal line to come to 63% of its final value, and it is the parameter used to evaluate the speed of transmission in the interconnect. The resistance is directly proportional to the length of the metal interconnect and inversely proportional to its cross section. Eventhough metal lines become thinner as the chip features are reduced in size, their length doesn't change, because of the complexity of the circuit. So the resistance and power consumption is increased. Moreover, the capacitance between parallel metal lines is inversely proportional to their relative separation, becoming the dominating factor in the delay for spacings below 0.5 μm. Current feature sizes are 0.25 μm or less.

While the increase in the number of transistors in integrated circuits makes computers faster and advances in optical fibers techniques make communication signals get faster, there is still the need to convert the optical signal into an electrical one and vice versa, at the interface between processors and cables. Light needs to be converted to electricity in order to be modulated, switched or amplified and the RC delay time puts a limit on the maximum processing speed achievable,

of the order of hundreds of GHz [12, 13].

It would be desirable to build an all-optical network, comprising optical transmitters and receivers, optical switches, modulators and amplifiers, with pitches comparable to current electronic circuitry. This would reduce the power consumption and increase the transmission and processing speed.

In order to mantain the size standard of electronic components, light must be squeezed effectively into subdiffraction volumes. This is possible converting it into waves that travel along the surface of metals, called plasmons.

A surface plasmon can be succinctly described as a quantised longitudinal oscillation of surface charge at a metal-dielectric interface. A surface plasmon polariton (SPP) is an extension of this phenomenon, in which a photon of specific polarisation is coupled to this surface charge oscillation. The plasmon polariton propagates along the metal-dielectric interface and decays evanescently along the direction perpendicular to it. This type of wave is thus able to confine the electromagnetic energy into volumes smaller than the free space wavelength of the photon. Local Surface Plasmon Resonances (LSPRs) are non-propagating oscillations of free electrons in metallic nanoparticles, in which the oscillation frequency matches that of the driving field [14–16]. The resonant frequencies at which SPPs and LSPRs are coupled depend strongly on the type of metal and dielectrics considered, and on the geometry of the system analyzed. Thus metal surfaces and nanoparticles, thanks also to the state-of-the-art fabrication technologies available, can be engineered in order to finely tune the plasmon resonance.

Plamsonics offers not only the possbility to scale down the size of optical devices, but also to perform active funcitonalities with minimal input power. The underlying operating mechanism of these active plasmonic optical devices is optical nonlinearity. In general, a material exhibits optical nonlinearity when it responds superlinearly to an applied electromagentic field. This superlinear response can be well represented by a polarizability comprising higher order susceptibility tensors. In essence, light modifies the optical properties of a material when interacting with it nonlinearly. One of the appealing characteristics of optical nonlinearities is that they are controllable via various control signals, as the incident light intensity or

an applied voltage, and reversible. This means that the structure of an optical component can be effectively dynamically changed by a nonlinear interaction in terms of its optical properties, without the geometry of the system being modified per se. Nonlinear optical interactions also happen on an ultrafast time scale, spanning from tens of femtoseconds to several picoseconds, depending on the origin of the nonlinearity and on the geometry of the structure considered.

There are some inherent limitations in the use of nonlinear optical devices though: first of all, the higher order susceptibility terms are tens of orders of magnitude smaller than the first order susceptibility, 15 in the case of the third order nonlinear suceptibility of gold. This means that a high intensity of the incident light is necessary for nonlinear effects to arise. There is then a trade-off between the intensity employed and the time response of the optical device. SPPs and LSPRs can reduce the intensity of light required to induce nonlinear optical interactions, due to the tight field confinement that they can provide. The temporal behaviour of the optical properties of metals is very fast, ranging from tens of femtoseconds to a few picoseconds in different regimes, depending on the electron plasma relaxation processes involved [17, 18]. Additionally, the spectral tunability of the plasmonic response gives the possibility to realize highly specific devices for different wavelengths of interest.

Plasmonics might be the only answer currently available that combines integrable devices size and dynamic performances for all-optical signal processing. Its main drawback are the losses that have to be inevitably considered in the presence of metallic nanostructures. The effect of losses can be minimized though, exploiting the great spectral tunability of plasmonic modes and the interaction of these modes with gain materials. The balance between losses and ultrafast, enhanced active performances can be adjusted modifying the nanostructuring and the volume ratio between metallic and dielectric components.

In this thesis, I will theoretically and mostly numerically characterize the nonlinear, ultrafast light modulation performed using plasmonic metamaterials. Plasmonic metamaterials are metal-dielectric, nanostructured composites, that

exhibit collective optical properties determined by the coupling between the plasmonic resonances of the individual metallic features.

In Chapter 2, I will outline the basic physical principles governing the behavior of SPPs and LSPRs, the optical response of plasmonic metamaterials based on arrays of vertically aligned gold nanorods, and the Kerr optical nonlinearity used to perform ultrafast modulation with this metamaterial.

In Chapter 3, I will describe the numerical modelling techniques used throughout this thesis, based on the Finite Element Method, to simulate the linear and nonlinear optical properties of the plasmonic nanorods metamaterial. The main element of novelty introduced in this Chapter is the modelling of the nonlinear dynamic behaviour of the nanorod metamaterial that enables to monitor the evolution of the spatial distribution of the electron's temperature and of the gold dielectric permittivity during a pump-probe experiment, and to combine any different control and signal light configurations.

In Chapter 4, I will present the modelling and experimental characterization of the optical response of the nanorod metamaterial in a substantially unexplored spectral region for artificial epsilon-near-zero metamaterials, the near-Infrared. This shows how the robustness of the fabrication technique allows to fully exploit the tunability of the metamaterial's optical response.

In Chapter 5, I will analyze the optical response of plasmonic metamaterials consisting of vertically aligned core-shell nanoparticles, extending the limits of applicability of the quasi-static and effective medium treatments.

In Chapter 6, I will extensively theoretically and numerically characterize the ultrafast response of the gold nanorod metamaterial, controlled by an ultrashort optical pulse. The analysis of the nonlocal response of the metamaterial shows the presence of hyperbolic modes also above the local epsilon-near-zero condition, observed for the first time. The most important novel result obtained is the identification of inhomogeneities in the electrons temperature distribution as enhancing factors in the nonlinear optical extinction modulation and in its time response. I prove that the coupling of signal metamaterial resonances allows to sample selectively the regions with the fastest electron temperature dynamics.

In Chapter 7, I will characterize numerically the ultrafast optical modulation performed with a gold core, J-aggregate shell metamaterial, in the strong and weak coupling regimes between the plasmonic modes and the molecular excitons supported by the aggregate. This is the first time the all-optical control of the strong coupling between molecules and metamaterials is demonstrated.

In Chapter 8, I will summarize the main results achieved with this work and the future outlook.

Chapter 2

Elements of theory of plasmonic metamaterials and optical nonlinearities

This chapter provides an outline of the physical theories which are employed to perform ultrafast modulation of light with a nonlinear, plasmonic nanorod metamaterial. The theoretical framework of Surface Plasmon Polaritons (SPPs), Local surface Plasmon Resonances (LSPRs) and plasmonic modes of metamaterials follows [15, 19], while the theoretical description of the third order nonlinear optical effects follows closely [13].

2.1 Metamaterials

The optical, electrical and magnetic macrosopic properties of materials are determined by their dielectric permittivity, generally indicated as ϵ and linked with the material's conductivity and resistivity, and their magnetic permeability, generally indicated as μ. In fact, the dynamical response of aggregates of atoms of a material to an electric and magnetic field is summarized in the constitutive

relations

$$\begin{aligned} \vec{D} &= \epsilon \vec{E} \\ \vec{J} &= \sigma \vec{E} \\ \vec{B} &= \mu \vec{H} \end{aligned} \tag{2.1}$$

for an isotropic, permeable, conducting dielectric [20], where $\vec{D}$ is the electric field displacement, $\vec{E}$ is the electric feld, $\vec{J}$ is the current density measured in units of positive charge crossing unit area per unit time, the direction of motion of the charges defining the direction of $\vec{J}$, $\vec{B}$ is the magnetic flux density or magnetic induction and $\vec{H}$ is the magnetic field. One of the most important predictions of Maxwell's equations is the exsistence of electromagnetic waves, since the electric and magnetic field satisfy the wave equation that can be derived from them:

$$\frac{\partial^2 \vec{E}}{\partial^2 t} - \frac{c^2}{\epsilon \mu} \nabla^2 \vec{E} = 0 \tag{2.2}$$

where $\frac{c^2}{\epsilon \mu}$ is the velocity with which the wave is propagating in the medium. Thus ϵ and μ determine the characteristics of the propagation of an electromagnetic wave in the material considered.

Metamaterials are structured, composite materials, realized by assembling elementary inclusions in some host medium. The greek word "meta" means "beyond", and indicates the key feature of these composites, the fact that their ϵ and μ can be artificially modified, allowing to obtain opto-electronic properties that are not present in naturally available materials. Their response to an applied electromagnetic field will be the result of the superposition of the responses of the individual components, such that it is possible to define collective opto-electronic properties, that characterize the metamaterial as a whole. These properties can be taylored precisely by changing the constituent materials, the shape of the elementary units and their relative arrangement. The collective optical response of a metamaterial will arise in a wavelength region that exceeds the size of the individual features.

The first intuition of the potential of artificially modifying the electromagnetic properties of materials by assembling different individual components can be found in the work of Kock, that realized the first artificial dielectrics. He also studied the response of customized metallic particles to electromagnetic fields. In particular, he studied theoretically and realized a metallic dielectric, constructed by arraying conducting elements in a three-dimensional lattice structure. This structure displayed an effective dielectric constant for wavelengths long with respect to the size and spacing of the elements, and was designed to focus microwaves and longer radio waves as a glass lens focusses visible light [21, 22].

Victor Veselago was another pioneer of metamaterials and in the 1960s studied theoretically the potential of optically customized materials, in particular isotropic and anisotropic negative refractive index materials, showing that they wouldn't violate any fundamental physical law [23].

John Pendry then studied the possibility of using negative refraction to obtain lenses capable of overcoming the diffraction limit [24]. The capability of resolving subwavelength details is given by the fact that the wavevector of the evanescent components of the light emitted by a source, are within the light cone in the negative refractive index metamaterial, and thus can be collected and recovered in the image.

The first experimental measurement of the negative refractive index of a metamaterial was performed by David Smith and collaborators [25], which used a metamaterial consisting of a two-dimensional periodic array of copper split ring resonators and wires on a fiber glass circuit board material. A prism was formed assembling several interlocking boards, and the refraction of a light beam passing through the sample was measured and allowed to assign an effective negative refractive index to the metamaterial. It was the experimental proof of a structured, composite material behaving as a homogeneous material, with negative refraction in the microwave region.

2.2 Plasmonic metamaterials

Nanostructured, metal/dielectric metamaterials are plasmonic metamaterials. They benefit from the strong interaction between light and the conduction electrons of the metallic components, which can support SPPs or LSPRs. The electromagnetic interaction between the individual metallic features determines a collective plasmonic response. The plasmonic modes of the metamaterial have a well defined spatial distribution of tightly confined, enhanced electromagnetic field and associated resonant features at specific spectral positions in their far field optical extinction and reflection. The size of the individual features in plasmonic metamaterials is of several tens of nanometers, and so they exhibit a collective electromagnetic behavior in the visible and near-Infrared region of the electromagnetic spectrum. Their optical properties can be taylored by changing the individual constituent materials and the nanopatterning.

2.2.1 Surface Plasmon Polaritons and Localized Surface Plasmons

An SPP is an electromagnetic excitation propagating along the interface between a dielectric with real, positive dielectric permittivity ϵ_1, and a conductor with negative real part of the dielectric permittivity ϵ_2, and evanescently decaying in the direction perpendicular to the interface. This electromagnetic field is the result of the coherent electron density oscillation at the conductor surface. The wavevector of such an excitation along the interface between two semiinfinite slabs, β, can be determined by imposing its evanescent character along the perpendicular direction and considering the appropriate boundary conditions for the harmonic electric and magnetic fields, $\beta = k_0\sqrt{(\epsilon_1\epsilon_2)/(\epsilon_1+\epsilon_2)}$.

An SPP on a flat interface can be obtained only for TM polarized waves. The metallic character of the conductor is determined by the real part of its dielectric constant, that is negative, and a real metal will have some losses, so that the propagation wavevector β is in general complex, leading to attenuation of the SPP also in the direction of propagation. Figure 2.1 (a) shows the schematic of

the SPP electric field at a metal/dielectric interface. The SPP is coupled with a prism (n=1.5), so that it is possible to couple a wavevector bigger than the wavevector of light in air, and thus have a confined mode. Figure 2.1 (b) shows the wavevector dispersion relation of an SPP at the interface between a semiinfinite air slab and a semiinfinite lossless Drude gold slab. Confined modes, for which the propagation vector along the interface is greater than that of light in the dielectric medium, exist only below the plasma frequency, and for the lossy metal, β saturates to a finite value approaching the plasma frequency. The travelling wave is able to cover a distance of $(2Im(\beta))^{-1}$ before reducing its intensity of a factor $1/e$. This so-called propagation length for the SPP is typically between few tens and few hundred microns in the visible and in the near-Infrared spectral range, respectively.

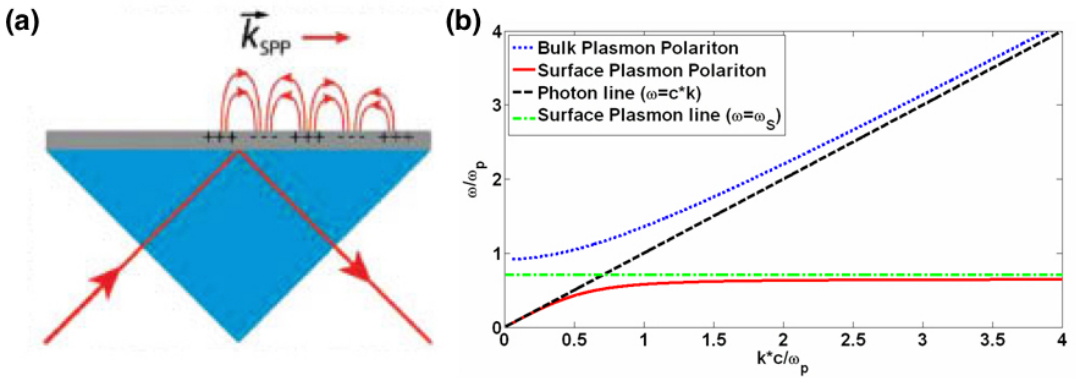

FIGURE 2.1: (a) Schematic cartoon of the electric field lines of an SPP at the interface between a metal film and air, excited using a prism. The field is evanescently decaying in the direction perpendicular to the interface and attenuated in the direction of propagation. This figure is taken from [26]. (b) The red line shows the dispersion relation $\omega(k_x)$ of an SPP at the interface between a semi-infinite lossless Drude gold layer and air. All units are normalized to the plasma frequency of gold.

The evanescent components of the SPP can significantly enter the two semi-infinite slabs for a penetration depth of k_z^{-1}, where k_z is the component of the wavevector in the direction perpendicular to the interface, $k_z = \sqrt{\beta^2 - \epsilon_i \omega^2 c^2}$.

The SPP can thus probe the dielectric medium, in which the penetration depth is typically of the order of the wavelength in the material, much more than the metallic one, in which it decays in few tens of nanometers. The energy of

the electromagnetic excitation can be thus confined in the metal over a distance smaller than the wavelength in free space interacting with the materials.

The propagation constant of bound SPPs is always going to be bigger than the wavevector of the radiation in both materials, so in order to couple these modes we need a coupling prism or any type of scatterer that would compensate for the momentum difference [15].

Individual metallic nanoparticles sustain Localized Surface Plasmon Resonances, non-propagating coherent oscillations of the conduction electrons coupled with an incident electromagnetic field. Similarly to SPPs, they provide subdiffraction field confinement, of the order of the size of the nanoparticle for dipolar LSPRs and also enhancement, typically of the order of 10.

This resonant enhancement can be understood considering a particle with size within the quasistatic limit, i. e. sufficiently smaller than the wavelength in free space of an incident electromagnetic field. The problem is that of determining the dipole moment of the particle induced by the electrostatic field. For convenient geometries [19], it is possible to derive a resonant polarization for the nanoparticles. In the case of a sphere of dielectric permittivity ϵ_1, embedded in a medium of dielectric permittivity ϵ_2, the dipolar polarizability is

$$\alpha = 4\pi a^3 \frac{\epsilon_1 - \epsilon_2}{\epsilon_1 + 2\epsilon_2} \tag{2.3}$$

A metallic sphere will have a negative real part of the dielectric permittivity and so it is possible to find a resonant condition, called the Frölich condition, for the dipolar polarizability, Re[ϵ_1]=-2ϵ_2.

In the case of a perfect sphere it is possible to determine an exact solution for the field scattered by the nanoparticle using Mie theory [19, 27]. Figure 2.2 shows the extinction cross sections of an isolated gold sphere with varying radius normalized to the geometrical cross sections, calculated using Mie theory [19]. The dielectric permittivity of the sphere is taken from [28]. For spheres of considerable radius the dipolar Frölich condition is not the only resonant condition found. Other multipolar resonances can de identified.

Similarly, in the case of an ellipsoid with principal semixes a_1, a_2, a_3, it

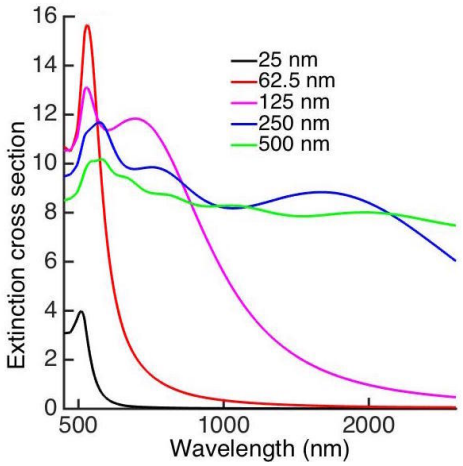

FIGURE 2.2: Extinction cross sections of isolated gold spheres of increasing radius with dielectric permittivity taken from [28]. The environment is assumed to be air (n=1). The extinction cross section for each particle is normalized to the geometrical cross section.

is possible to derive a dipolar polarizability. We choose the Cartesian reference system to coincide with the principal axes of the ellipsoid. Figure 2.3 shows an ellipsoid with its semiaxes and reference system, together with the wavevector and electric field of the plane wave interacting with it.

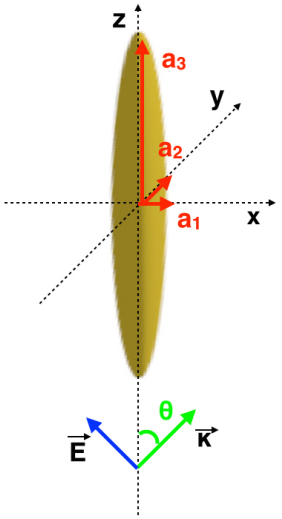

FIGURE 2.3: Schematic of an ellipsoidal particle and of the wavevector and electric field of a plane electromagnetic wave interacting with it. The cartesian reference system is chosen to coincide with the principal axes of the particle.

Again, the dipolar description is sufficiently accurate to reproduce the scattering of the particle as long as the characteristic dimensions of the ellipsoid are

much smaller than the wavelength of the light interacting with it

$$a_1, a_2, a_3 << \lambda \tag{2.4}$$

If this condition holds we are in the quasi-static regime, so retardation effects of the electromagnetic field over the volume of the nanoparticle can be neglected and it can be treated as a dipolar resonator. The ellipsoid's polarizability is

$$\alpha = 4\pi a_1 a_2 a_3 \frac{\epsilon - \epsilon_m}{3\epsilon_m + 3L_i(\epsilon - \epsilon_m)} \tag{2.5}$$

where ϵ is the dielectric permittivity of the ellipsoid, ϵ_m is the dielectric permittivity of the embedding medium. L_i is the geometrical factor

$$L_i = \frac{a_1 a_2 a_3}{2} \int_0^\infty \frac{dq}{(a_i^2 + q) f(q)} \tag{2.6}$$

The subscript i indicates the geometrical factor along the principal axes of the ellipsoid, which coincide with the cartesian axes. $f(q) = \sqrt{(q + a_1^2)(q + a_2^2)(q + a_3^2)}$. The condition $\sum_{n=1}^{3} L_i = 1$ has to be always satisfied, so for a sphere this geometrical parameter reduces to 1/3. The geometrical factors are linked to the depolarization factors, $L_{dep,i}$ via

$$L_{dep,i} = \frac{\epsilon - \epsilon_m}{\epsilon - 1} \frac{L_i}{\epsilon_0 \epsilon_m} \tag{2.7}$$

In the special case of a prolate spheroid, obtained revolving an ellipse around its major axis, there will be only one independent equation for the geometrical factors, relative to the small axes. When expressing it as a function of the eccentricity $e = 1 - \frac{a_1^2}{a_3^2}$

$$L_1 = \frac{1 - e^2}{e^2}(-1 + \frac{1}{2e} ln \frac{1 + e}{1 - e}) \tag{2.8}$$

The quantity a_3/a_1, the ratio between the long and short semiaxis of the prolate spheroid, is the aspect ratio. The result obtained for the polarizability of the prolate spheroid allows three resonant conditions, one per principal axis (two of these are degenerate, due to the fact that the short axes of a spheroid are identical),

that can be physically interpreted as the oscillation of the conduction electrons along the short and long axis of the nanoparticle. Figure 2.4 shows the extinction cross sections of isolated gold prolate spheroids with different eccentricities, i.e. aspect ratios, normalized to the geometrical cross section of the nanoparticles.

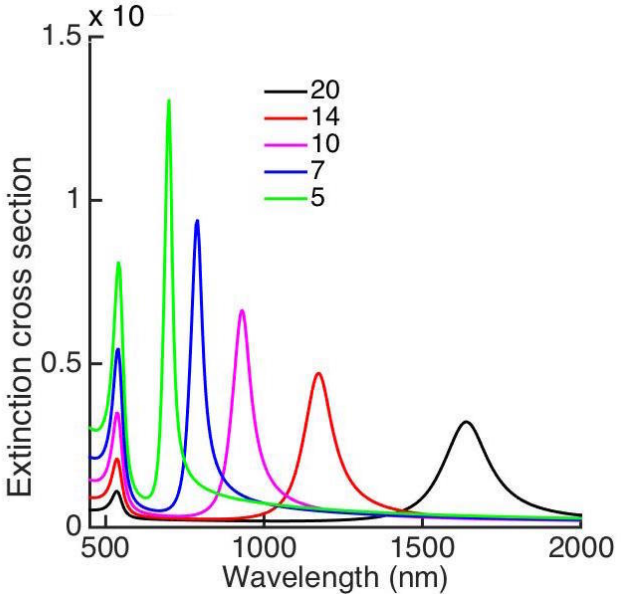

FIGURE 2.4: Extinction cross sections of isolated gold prolate spheroids with varying aspect ratios, normalized to the geometrical cross sections. The environment is supposed to be air (n=1) and the dielectric permittivity of the spheroids is taken from [28].

LSPRs can be excited with any wavevector of the incident light, as long as the wavelength dependent dielectric permittivity of the metallic nanoparticle satisfies the Frölich condition. There is no need of phase-matching techniques as in the case of SPPs, since this requirement is essentially satisfied by scattering. The field enhancement provided by LSPRs can be interpreted as the resonant enhancement of the field of the radiating dipole induced in the nanoparticle by the incident electromagnetic field. It has been shown both for spheres and spheroids that the geometrical parameters play a fundamental role in the amplitude, linewidth and spectral position of the resonances. These characteristics can be tuned by changing the radius in the case of metallic spheres and the aspect ratio in the case of prolate spheroids.

2.2.2 Nanorod plasmonic metamaterials

The plasmonic resonant modal structure of metamaterials can be derived conceptually from the electromagnetic coupling between the LSPRs of the individual metallic constituents. In this thesis I will examine a particular type of metamaterial, a square array of vertically aligned gold nanorods embedded in an anodized aluminum oxide (Al_2O_3) matrix (AAO).

Electrochemical deposition, a reliable and extremely versatile fabrication process, is used. The nanorods are electrodeposited into the nanoporous AAO templates. The templates are formed by the self-organization of an aluminum film, sputter-deposited onto a multilayered conducting substrate, during anodization. The substrate is made of a glass slide, a 10 nm thick tantalum pentaoxide base layer for adhesion (Ta_2O_5) and a 5 nm thick gold film supporting the AAO film [29].

The geometrical parameters of the array, i. e. the diameter and period of the pores in the AAO film, are determined by the voltage applied and the characteristics of the chemical solution used in the anodization process. The duration of the electrodeposition determines the length of the rods.

The typical dimensions are several hundreds of nanometers for the length and tens of nanometers for the centre to centre distance and diameter of the rods. Figure 2.5 shows a schematic of the system.

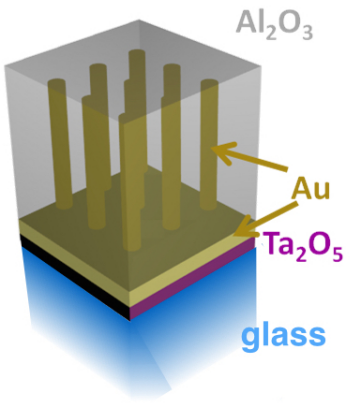

FIGURE 2.5: Schematic of the gold nanorod metamaterial examined in the present work.

In the remaining of this Chapter, as well as in Chapter 5, 6 and 7, the multilayer structure of Figure 2.5 will be simplified, i. e. the Ta_2O_5 and gold underlayers will not be considered in the theoretical and numerical modelling. This doesn't affect the analysis of the linear and nonlinear properties of the metamaterial. The complete structure will be considered in Chapter 4.

Sufficiently small nanorods can be approximated as prolate spheroids, in which an electrostatic field can induce enhanced scattering at specific wavelengths corresponding to the resonant conditions for the dipolar polarizability derived in 2.2.1.

Given the subwavelength separation between them, the individual dipoles are able to interact. The modes of an assembly of resonant particles will be spectrally shifted with respect to the isolated particle response, and this can be intuitively explained considering the Coulomb interaction between the radiating dipoles, as pictured in Figure 2.6.

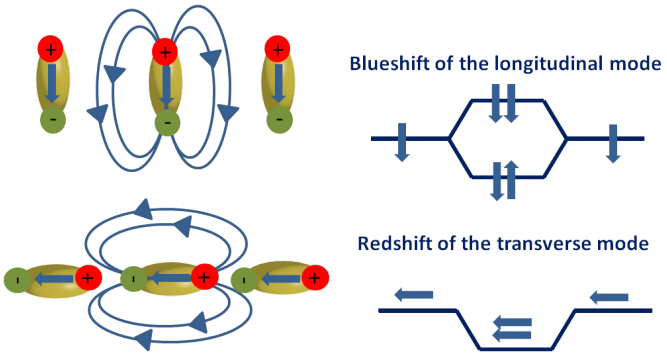

FIGURE 2.6: Schematics of the dipolar interaction between aligned metallic nanoparticles sustaining LSPRs.

The restoring force acting on the oscillating electrons of each particle in the chain is either increased or decreased by the charge distribution of neighbouring particles. When light is polarized along the short semiaxes of the spheroids, the dipoles generated by the electrons oscillation will determine a collective redshifted transverse mode of the metamaterial with respect to the individual particle resonance (T-mode). When light is polarized along the long semiaxis of the spheroids, the dipoles generated by the electrons oscillation will determine a collective blueshifted longitudinal mode of the metamaterial with respect to the individual particle resonance (L-mode). A more rigorous microscopic picture of

the origin of the collective modes is the interaction of cylindrical surface plasmons (CSP) supported by individual nanorods forming the metamaterial.

As outlined in the introduction to section 2.2, the uniqueness of metamaterials consists in the fact that they exhibit collective opto-electronic properties, that can be described with an effective dielectric permittivity. I am now going to derive it for the nanorod metamaterial just described. Figure 2.7 shows the approximations used to treat the nanorod metamaterial as a homogeneous medium. The cylinders are approximated as prolate spheroids, and the spheroids are vertically aligned with respect to their rotation symmetry axis. The cartesian reference systems at the bottom of the Figure show also the wavevector of a TM polarized plane wave interacting with the nanorod metamaterial. I will be exclusively interested in the behavior of the metamaterial exposed to TM polarized waves with respect to the glass/nanorod interface. The reference systems on the top right indicate the identification that will shortly be made between the cartesian axes and the directions parallel, $||$, and perpendicular, $\perp$, to the nanorod symmetry axis. The L-mode of the metamaterial will be accessed only when there is a non-vanishing component of the electric field along the rods symmetry axis, so only for a non-normal incidence of the TM polarized wave.

One of the first and most enduring models to describe the permittivity of random composites is the Maxwell-Garnett approximation. The metal nanorod array can be considered as a set of inclusions embedded in a matrix. Both the inclusions and the matrix are assumed to be individually homogeneous. In the most general derivation of the effective dielectric permittivity of our metamaterial slab, the inclusions are identical in composition but may be different in volume, shape, and orientation. The average electric field $< \vec{E} >$ over a volume V of the metamaterial surrounding the point $\vec{r}$ is defined as [19]

$$< \vec{E}(\vec{r}) >= \frac{1}{V} \int_V \vec{E}(\vec{r} + \vec{\zeta}) d\vec{\zeta} \tag{2.9}$$

V is composed of the matrix volume and the volume of all the inclusions around $\vec{r}$. The integral of equation 2.9 is calculated separately in the matrix and in the

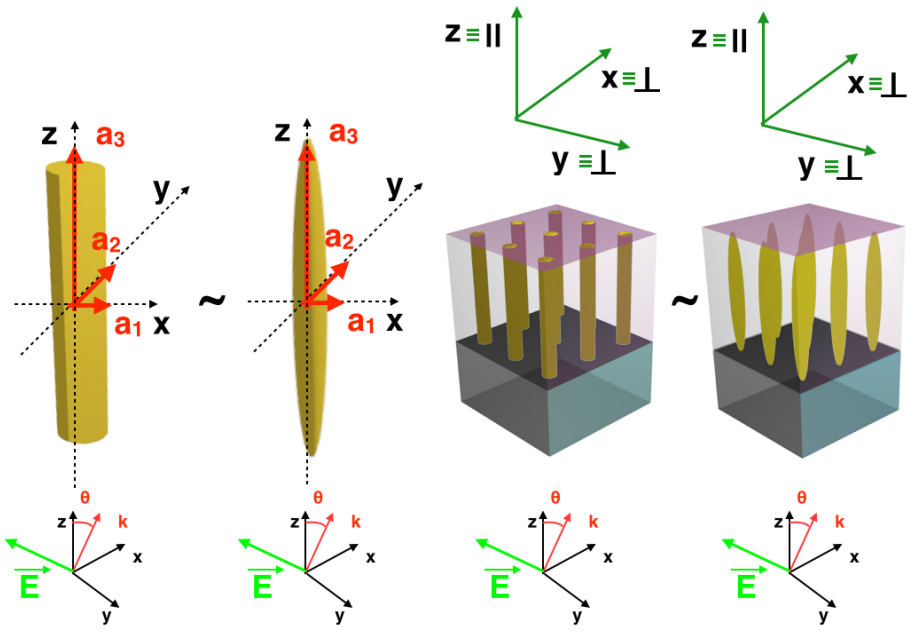

FIGURE 2.7: Schematic of the approximation of gold cilynders (nanorods) to prolate spheroids. The cartesian reference system is aligned with the principal axes system of the spheroids.

inclusions

$$< \vec{E}(\vec{r}) >= (1-f) < \vec{E_m}(\vec{r}) > +f \sum_i w_i < \vec{E_i}(\vec{r}) > \tag{2.10}$$

where $< \vec{E}(\vec{r}) >$ is the average field in the metamaterial, $< \vec{E_m}(\vec{r}) >$ is the average field in the matrix, $< \vec{E_i}(\vec{r}) >$ is the average field in the i^{th} inclusion, f is the total volume fraction of the arbitrary inclusions, w_i is the fractional volume of each type of inclusion i divided by f. The average polarization is given by

$$< \vec{P}(\vec{r}) >= (1-f) < \vec{P_m}(\vec{r}) > +f \sum_i w_i < \vec{P_i}(\vec{r}) > \tag{2.11}$$

where

$$\begin{aligned} < \vec{P}(\vec{r}) >= [\epsilon_{average}] < \vec{E}(\vec{r}) > \\ < \vec{P_m}(\vec{r}) >= [\epsilon_m] < \vec{E_m}(\vec{r}) > \\ < \vec{P}(\vec{r}) >= [\epsilon_i] < \vec{E_i}(\vec{r}) > \end{aligned} \tag{2.12}$$

if the metamaterial, the matrix and the inclusions are assumed to be linear materials. $[\epsilon_{average}]$, $[\epsilon_m]$ and $[\epsilon_i]$ are the dielectric permittivity tensors of the constituents.

The tensors of the inclusions, spheroids in this case, and of the matrix are all diagonal, having chosen the coordinate reference system to coincide with the principal axes of the inclusions.

The effective permittivity should not depend on the position, since the process being performed is exactly that of homogenizing the metamaterial. This implies that the average electric fields in the matrix and in the inclusions have to be linearly related. The linear dependence of the field in the inclusions on the field in the matrix is

$$< \vec{E_i}(\vec{r}) >= [\lambda] < \vec{E_m}(\vec{r}) > \tag{2.13}$$

where the diagonal components of the tensor $[\lambda]$ are

$$\lambda_k = \frac{\epsilon_m}{\epsilon_m + L_k(\epsilon_i - \epsilon_m)} \tag{2.14}$$

where L_k is the geometrical factor of the inclusion, seen previously in 2.6. It is crucial to assume that the field in the matrix is, as well as the incident field, uniform. Actually in this case the incident field and the field in the matrix coincide, due to the fact that the array is isotropic. Combining equation 2.11 and equation 2.12, 2.13 and 2.14, the tensor equation for the effective dielectric permittivity is

$$(1-f)([\epsilon_{average}] - [\epsilon_m]) + f([\epsilon_{average} - \epsilon_i])[\lambda] = 0 \tag{2.15}$$

The diagonal components of the effective permittivity tensor can then, starting from equation 2.15, be derived in terms of the spheroids polarizability tensor components α_{jj}

$$\epsilon_{eff,jj} = (1 + \frac{f\alpha_{jj}}{1 - \frac{f/3}{\alpha}_{jj}}) \tag{2.16}$$

Due to the symmetry of the spheroids, it is easier to identify the cartesian axes with the directions parallel and perpendicular to the spheroids symmetry axis. The direction parallel to the nanorod and spheroid symmetry axis is z, and the corresponding $\epsilon_{eff,zz}$ will be called $\epsilon_{||}$. The directions perpendicular to the nanorod and spheroids symmetry axis are x and y, and the corresponding $\epsilon_{eff,xx}$ and $\epsilon_{eff,yy}$ will be called $\epsilon_{\perp}$.

This metamaterial behaves as a uniaxial material, with an anisotropic permittivity tensor. The components of the tensor corresponding to the directions perpendicular to the nanorod and spheroids symmetry axis, which are the ordinary axes of the metamaterial, coincide, but are different from the tensor component corresponding to the direction parallel to the nanorods and spheroids symmetry axis, or extraordinary axis.

For nanorods which are several hundreds of nanometers long, we can approximate the metamaterial as infinite along all directions [30]. If the inclusions are placed in a uniform incident electric field, that we can identify with $\vec{E}_m(\vec{r})$ using the same notation as in the previous treatment, a polarization field $\vec{E}_i(\vec{r})$ is created inside them, having the same direction of $\vec{E}_m(\vec{r})$. Thus $\vec{E}_i(\vec{r})$ must satisfy the boundary conditions at the surface of the nanorods. Considering the incident electric field to be along the symmetry axis of the nanorods, the only boundary condition that needs to be satisfied is that the tangential components of the electric field are continuous at the rod surface, that is $< \vec{E}_m(\vec{r}) >=< \vec{E}_i(\vec{r}) >$. The average electric field is then

$$< \vec{E}_{||}(\vec{r}) >= N < \vec{E}_i(\vec{r}) > +(1-N) < \vec{E}_m(\vec{r}) > \tag{2.17}$$

where N is the volume fraction of the inclusions. The average displacement field is

$$< \vec{D}_{||}(\vec{r}) >= N\epsilon_i < \vec{E}_i(\vec{r}) > +(1-N)\epsilon_m < \vec{E}_i(\vec{r}) > \tag{2.18}$$

Therefore the effective permittivity along the symmetry axis of the nanorods is

$$\epsilon_{||} = N\epsilon_i + (1-N)\epsilon_m \tag{2.19}$$

I will refer to the description of the metamaterial using this effective dielectric permittivity as Effective Medium Theory (EMT) treatment. I have shown how the geometrical parameters of the metamaterial, contained in the spheroids polarizability through the geometrical factors L_k and in the porosity through the volume fraction N, determine changes in its collective optical properties.

In general a ray of light passing through a uniaxial material will be split into

two components, an ordinary and an extraordinary ray. The ordinary ray will propagate like in an isotropic medium with the ordinary dielectric permittivity, while the extraordinary ray will see an equivalent, direction dependent refractive index

$$n_e = \sqrt{\epsilon_\perp + \epsilon_i sin^2\theta_i (1 - \frac{\epsilon_\perp}{\epsilon_{||}})} \tag{2.20}$$

where θ_i is the angle of incidence of a plane wave at the interface between an isotropic medium with permittivity ϵ_i and our anisotropic metamaterial.

2.2.3 Modal structure of the nanorod metamaterial

It is possible to understand the occurrence of the L-mode from an effective medium prospective. Figure 2.8 shows the wavelength dependencies of $\epsilon_{||}$ and $\epsilon_\perp$ for a typical nanorod metamaterial geometry.

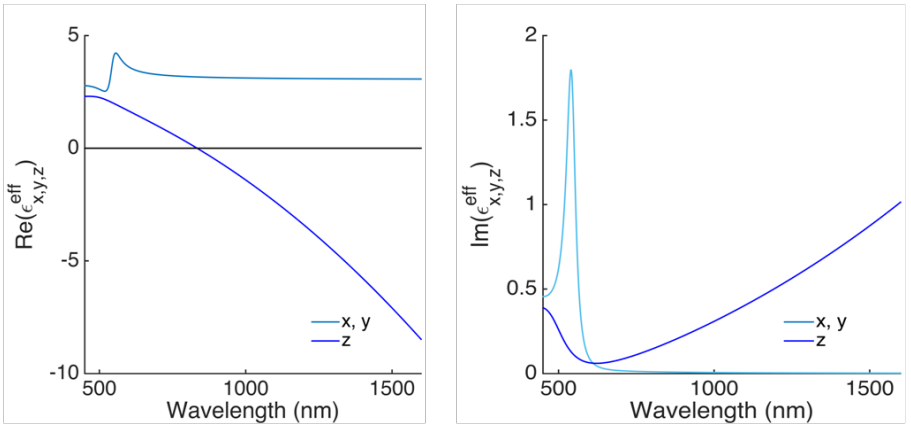

FIGURE 2.8: Effective parameters of the gold nanorod metamaterial. (a) shows the real part of the effective permittivity tensor components, (b) the imaginary part. The geometrical parameters used are 350 nm for the length, 30 nm for the rod diameter and 90 nm for the inter-rod spacing.

$\epsilon_{||}$ has a value between 1 and zero for wavelengths between 750 and 830 nm, meaning that a condition of total internal reflection is achievable at a specific non-zero angle of incidence also with a plane wave coming from the lowest refractive index medium, which is the air on top of the nanorod metamaterial. This condition of total internal reflection accounts for the resonant L-mode feature in the metamaterial's optical extinction spectrum.

The complex modal structure of the metamaterial can be derived analyzing the polarization-dependent propagation of plane waves in this medium, considering its effective dielectric permittivity tensor components. In vacuum, the linear dispersion of a plane wave is

$$k_x^2 + k_y^2 + k_z^2 = \frac{\omega^2}{c^2} \tag{2.21}$$

So that the isofrequency surface at every frequency ω is a sphere. Let's assume a plane wave interacting with a uniaxial material, with the electric field along the direction perpendicular to the nanorod axis, that is, along the ordinary axis of the uniaxial material, $\vec{E} = (E_x e^{(i(k_x x + k_y y + k_z z)}) \vec{i_\perp}$. The dispersion relation of the ordinary wave is then

$$k_x^2 + k_y^2 + k_z^2 = \epsilon_\perp k_0^2 \tag{2.22}$$

where k_0 is the wavevector in free space. This dispersion is the same as that of a wave propagating in an isotropic medium. With a plane wave polarized along the direction of the nanorod symmetry axis, $\vec{E} = (E_y \vec{j} + E_z \vec{k}) e^{i(k_x x + k_y y + k_z z)}$, the dispersion relation becomes

$$k_x^2 + k_y^2 + \frac{\epsilon_{||}}{\epsilon_\perp} k_z^2 = \epsilon_{||} k_0^2 \tag{2.23}$$

This is the dispersion relation of the extraordinary wave. The behavior of the real part of the effective dielectric permittivity along the extraordinary axis in our nanorod system determines two different disperson regimes for the slab, with different characteristics of the resonant modes. These different dispersion regimes correspond to different topologies of the isofrequency surfaces determined by the dispersion relation. If $\epsilon_{||}$ and $\epsilon_\perp$ have the same sign, the isofrequency surface is a closed ellipsoid and the dispersion regime is elliptic. While if the two have opposite signs, the isofrequency surface is an hyperboloid and in this case we talk about a hyperbolic dispersion regime. The isofrequency surfaces are shown in Figure 2.9. The frequency at which the component of the effective permittivity along the nanorod symmetry axis vanishes, that marks the transition between the elliptic and hyperbolic regime, is the effective plasma frequency of the metamaterial.

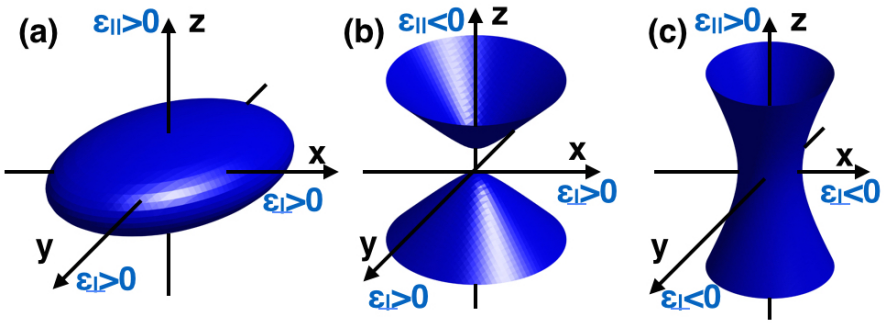

FIGURE 2.9: Topology of the isofrequency surfaces for an extraordinary wave propagating in the anisotropic nanorod metamaterial in the effective medium approximation. (a) is a closed ellipsoid, while (b) and (c) are type I and type II hyperbolic dispersions, respectively.

The most important property of hyperbolic media is related to the behavior of waves with large magnitude wavevectors. In vacuum, such large wavevector waves are evanescent and decay exponentially. However, in hyperbolic metamaterials (HMM) the open form of the isofrequency surface allows for propagating waves with infinitely large wavevectors in the idealistic limit. Since the spatial extent of a wave is inversely proportional to its wavevector, these waves will be characterized by high confinement. Type I HMMs have one component of the dielectric tensor negative ($e_{||} < 0\ e_{\perp} > 0$) while Type II HMMs have two components negative ($e_{||} > 0\ e_{\perp} < 0$). If all components are negative we obtain a metal, while if all components are positive we have a dielectric medium. One striking difference between the Type I and Type II hyperbolic metamaterials is that the hyperboloidal surfaces are two-sheeted and single-sheeted, respectively. The Type II metamaterial is highly reflective since it is more metallic than the Type I counterpart.

The homogeneized slab of nanorods within the semi-infinite glass substrate and air superstrate can be treated as part of a flat interface, multilayer structure. The optical transmission and reflection can be thus calculated with the Transfer Matrix Method (TMM) [31–33]. Each of the layers acts linearly on the fields components parallel to the planar interfaces in the form of a 2x2 matrix. In the case of P-polarized light, the method is analytically derived for a 3-layers system as in Figure 2.10.

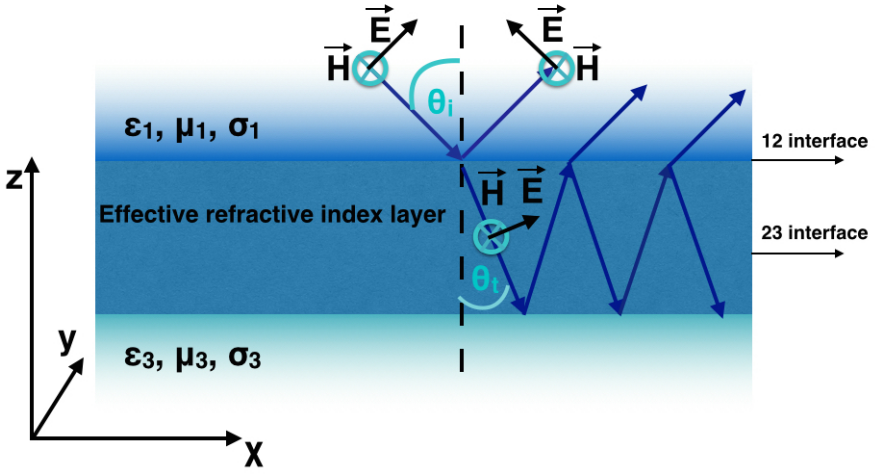

FIGURE 2.10: Schematic of a two interface system with a TM polarized plane wave undergoing reflection and refraction.

The 3-layers case of Figure 2.10, where the homogenized rod layer is embedded between two semi-infinite materials, can be easily generalized for an arbitrary number of layers above and below the metamaterial slab [31].

The finite thickness of the metamaterial slab constitutes a constraint for the possible values of the z-component of the wavevector of the modes supported by the metamaterial. In the same way as in an anisotropic waveguide [34], the modes are quantized as $k_z = q(\pi/l)$, where l is the slab thickness and q is an integer. The wavevectors have to still satisfy the dispersion relation in the metamaterial treated as a uniaxial crystal, so for TM polarized waves, the propagation constant along the x-axis in Figure 2.10 becomes

$$k_x = \epsilon_{||} k_0^2 - \frac{\epsilon_{||}}{\epsilon_\perp}(\pi \frac{q}{l})^2 \tag{2.24}$$

[35] where k_0 is ω/c. The modes with this quantized wavevector show negative group velocity with high effective refractive indices and have an unusual cut-off from the high-frequency side where the group velocity vanishes. The group velocity $\partial\omega/\partial k$ is negative provided the condition [35]

$$\epsilon_\perp \partial\epsilon_{||}/\partial\omega > \epsilon_{||}\partial\epsilon_\perp/\partial\omega \tag{2.25}$$

This condition is always satisfied in the hyperbolic dispersion region, where

the right hand side of the inequality is negative, being $\epsilon_{||}$ negative by definition in the hyperbolic regime, and $\epsilon_{\perp}$ increasing with frequency. The left hand side is positive, being $\epsilon_{\perp}$ positive and $\epsilon_{||}$ increasing with increasing frequency. The occurrence of these modes, also for frequencies above the effective plasma frequency of the metamaterial, will be examined in Chapter 6.

2.3 Optical nonlinearities

Materials in general interact linearly with an externally applied electric field. If we simplify at first the notation, assuming the electric field to be a scalar, the linear response of the material can be represented by a scalar polarizability which is proportional to the perturbing field via the linear susceptibility $\chi^{(1)}$, as $P(t) = \chi^{(1)}E(t)$. The linear susceptibility $\chi^{(1)}$ characterizes the "ordinary" optical behavior of a material. But when the electric field is sufficiently intense, with a threshold that depends on the specific material considered, this optical characteristics are changed by the interaction, and the response of the system depends on higher powers of the applied electric field strength.

Optical nonlinearities can give rise to a wide variety of effects, gain or amplification, conversion between wavelengths, generation of new wavelengths or frequencies. There are two main types of nonlinearities, those that arise from scattering (stimulated Brillouin scattering and stimulated Raman scattering) and those that arise from optically induced changes in the refractive index, and result either in phase modulation (self-phase modulation (SPM) and cross- phase modulation (XPM)) or in the mixing of several waves and the generation of new frequencies (modulation instability (MI) and parametric processes, such as four- wave mixing (FWM)). Frequency generation is used in LASERs applications, as well as self-focusing for laser beam reshaping. In the context of optical transmission systems, solitons are solutions of the nonliner wave equation in optical fibers, and consist of optical pulses which propagate undistorted. This is due to the fact that the SPM and group velocity dispersion effects cooperate in such a way as to cancel each other in solitons propagation. This makes them extremely useful in long-haul transmission.

I will be focusing on the nonlinear optical Kerr effect, that determines an illumination-intensity-dependent change in the refractive index of a material due to its interaction with light, in formulas

$$n = n_0 + n_I < E^2 > \tag{2.26}$$

where n is the total refractive index of the material, n_0 is the linear refractive index and n_I is the nonlinear correction, proportional to the time averaged electric field intensity $< E^2 >$. Nonlinear electric field-matter interaction can be expressed by expanding the polarizability as a power series in the electric field strength, with additional susceptibility terms. If we consider again a scalar electric field and polarizability:

$$P(t) = \chi^1 E + \chi^2 E^2 + \chi^3 E^3 + ... \tag{2.27}$$

This expression is useful in order to understand how a nonlinear light-matter interaction leads to new sources of electromagnetic radiation in the material considered, so to a nonhomogeneous wave equation

$$\nabla^2 E - \frac{n^2}{c^2}\frac{\partial^2 E}{\partial t^2} = \frac{4\pi \partial^2 P^{NL}}{c^2 \partial t^2} \tag{2.28}$$

The nonlinear polarization P^{NL} drives the electric field in the material [13]. Using a rigorous formalism, we can represent the electric field vector of an optical wave as the discrete sum of a number of frequency components as

$$\vec{E}(\vec{r}, t) = \sum_n \vec{E}_n(\vec{r}, t) \tag{2.29}$$

where we are summing among positive and negative frequencies. Expressing the frequency and time dependence of the components explicitly, the terms become

$$\vec{E}_n(\vec{r}, t) = \vec{A}_n e^{i\vec{k}\vec{r}} e^{-i\omega_n t} \tag{2.30}$$

so that the slowly varying complex amplitude of the field is $\vec{E}(\omega_n) = \vec{A}_n e^{i\vec{k}\vec{r}}$. We also need to impose a real condition on $\vec{E}(\vec{r}, t)$, in order for it to represent a physical

field: the negative frequency component is equal to the complex conjugate of the corresponding positive frequency component. Using the notation $\vec{A_n} = \vec{A_n}(\omega_n)$

$$\vec{A_n}(-\omega_n) = \vec{A_n}^*(\omega_n) \tag{2.31}$$

we obtain

$$\vec{E}_{-n}(\vec{r}, t) = \vec{E}^*_{+n}(\vec{r}, t) \tag{2.32}$$

and so we are ensured that the imaginary components of the field will cancel out summing over all frequencies, so

$$\vec{E}(\vec{r}, t) = \sum_n \vec{A}_n(\omega_n) e^{i(\vec{k}\vec{r} - \omega_n t)} \tag{2.33}$$

In the same fashion, it is possible to express the polarization as the sum of the responses associated with the different frequencies of the electric field components

$$\vec{P}(\vec{r}, t) = \sum_n \vec{P}(\omega_n) e^{-i\omega_n t} \tag{2.34}$$

As seen previously in Eq. (2.27), the polarizability can be expanded as a sum of terms in increasing powers of the filed strength $|\vec{E}(\vec{r}, t)|$, so the frequencies ω_n in Equation (2.34) are actually a combination of the elementary frequencies in the electric field decomposition

$$\vec{P}(\vec{r}, t) = \sum_i \vec{P}_i(\vec{r}, t) \tag{2.35}$$

with

$$\vec{P}_f(\omega_f) = \vec{P}(\sum_{n_f} \omega_{n_f}) \tag{2.36}$$

where the n_f runs over the number of different frequencies mixed by the electric field products. We can derive the susceptibility tensor components as the

constants of proportionality between the polarizability and the electric field amplitudes components, starting with the second order terms

$$P_i = \sum_{jk} \sum_{nm} \chi^2_{ijk}(\omega_n + \omega_m, \omega_n, \omega_m) E_j(\omega_n) E_k(\omega_m) \tag{2.37}$$

The indices ijk refer to the cartesian components of the fields and the sum over the indices m and n means that the quantity $\omega_n + \omega_m$ is kept fixed, while the indices m and n can vary accordingly. These amplitudes are associated to a temporal variation $e^{-i\omega_n t} e^{-i\omega_m t}$, so the second order nonlinear polarization component will oscillate with a frequency $\omega_n + \omega_m$. The summation over the field frequncies can be generalized as

$$P_i(\omega_n + \omega_m) = D \sum jk \chi^2_{ijk}(\omega_n + \omega_m, \omega_n, \omega_m) E_j(\omega_n) E_k(\omega_m) \tag{2.38}$$

where D is the degeneracy factor, the number of distinct permutations of the applied field frequencies ω_n and ω_m. From this algebraic result it is possible to analyze two second order effects, sum frequency generation and second harmonic generation. Sum frequency generation is a nonlinear process consisting in the annihilation of two photons of different frequency ω_1 and ω_2 with the consequent creation of a photon of frequency equal to the sum of the previous two, ω_3. The nonlinear polarizability of this process, assuming the symmetry of the susceptibility with respect to permutations of the field frequencies and considering the electric field to be polarized along the x axis, is

$$P_i = 2\chi^2_{ixx}(\omega_3, \omega_1, \omega_2) E(\omega_1) E(\omega_2) \tag{2.39}$$

In the case in which the two fundamental frequencies are the same, the process is second harmonic generation, when two identical photons are converted into a photon with twice the energy. The polarizability in this case, considering again the electric field to be polarized along the x axis, is

$$P_i = \chi^2_{ixx}(\omega_3, \omega_1, \omega_1) E^2(\omega_1) \tag{2.40}$$

These new frequency components of the electromagnetic field act, as mentioned previously, as sources of the electromagnetic field. The expression (2.38) for the second order polarizability term can be generalized for higher order interactions as (for three frequencies)

$$P_i(\omega_m + \omega_n + \omega_o) = D \sum_{jkl} \chi^{(3)}_{ijkl}(\omega_m + \omega_n + \omega_o, \omega_m, \omega_n, \omega_o) E_j(\omega_m) E_k(\omega_n) E_l(\omega_o) \tag{2.41}$$

The susceptibility in this case is a tensor of rank four, and the degeneracy factor is 6. A tensor of rank four is made out of 81 elements, but imposing symmetry conditions which hold in most materials, the number of distinct elements can be significantly reduced. In fact there are only three independent elements for an isotropic material. In order to analyze the physical processes which are a consequence of this algebraic result, it is useful to simplify the tensor form and consider an electric field polarized along the x axis. The nonlinear, third order polarizability term becomes

$$P_x(\omega_m + \omega_n + \omega_o) = D\chi^{(3)}_x(\omega_m + \omega_n + \omega_o, \omega_m, \omega_n, \omega_o) E_x(\omega_m) E_x(\omega_n) E_x(\omega_o) \tag{2.42}$$

Having three equal frequencies ω, the nonlinear polarizability corresponds to the process of third harmonic generation. Having two frequencies equal to ω and one equal to $-\omega$, the nonlinear polarizability describes an intensity dependent refractive index of the material, also called Optical Kerr effect. We can first derive the expression for the intensity dependent susceptibility

$$P_x(\omega + \omega - \omega) = 3\chi^{(3)}_x(\omega, \omega, -\omega) E(\omega) E(\omega) E(-\omega) \tag{2.43}$$

and since $E(-\omega) = E^*(\omega)$

$$P_x(\omega) = 3\chi^{(3)}_x(\omega, \omega, -\omega) |E(\omega)|^2 E(\omega) \tag{2.44}$$

The total polarization of the system is then described by

$$P(\omega) = \chi^{(1)}_x E(\omega) + 3\chi^{(3)}_x(\omega, \omega, -\omega) |E(\omega)|^2 E(\omega) \tag{2.45}$$

so we have the effective susceptibility

$$\chi_{effective} = \chi_x^{(1)} + 3\chi_x^{(3)}(\omega, \omega, -\omega)|E(\omega)|^2 \tag{2.46}$$

We can now relate the susceptibility with the refractive index, using the relation

$$n^2(\omega) = 1 + 4\pi\chi_{eff}(\omega) = \epsilon(\omega) \tag{2.47}$$

Recalling the general expression for the intensity dependent refractive index, Eq. (2.26), the time average of the electric field norm, when the electric field is a sum of positive and negative frequencies, is written as

$$< E^2 >= 2E(\omega)E^*(\omega) = 2|E(\omega)|^2 \tag{2.48}$$

so the refractive index can be written as $n = n_0 + n_I 2|E(\omega)|^2$. Equating n^2 to its expression as a function of the effective susceptibility and keeping only the terms in $|E(\omega)|^2$, the refractive index is written as

$$n_0 = (1 + 4\pi\chi^{(1)})^{\frac{1}{2}}, n_I = \frac{3\pi\chi^{(3)}}{n_0} \tag{2.49}$$

It is thus proved how a particular third order nonlinear light-matter interaction and the third order susceptibility determine an intensity-dependence of the refractive index of a material.

2.3.1 Kerr nonlinearity of gold

We are interested in the ultrafast electronic contribution to the optical Kerr nonlinearity of gold. When exposed to an intense electromagnetic field, the electrons in the conduction and valence band of the metal will absorb photons and so the population of the different bands will be changed [36–40]. In particular, the electrons involved in this redistribution belong to the 5d valence band and the partially filled 6sp band [41]. The equilibrium distribution of electrons in energy space is described by a Fermi distribution function, which is characterized by a well defined equilibrium electrons temperature, T_e. In the previous section I have

derived the effective, third order nonlinear susceptibility of a material, which is linked to the dielectric permittivity by $\epsilon = 1 + 4\pi\chi_{eff}(\omega)$. It is possible to derive an analytic expression of the total nonlinear susceptibility in the context of the Random Phase Approximation (RPA) [13, 42–46]. The dynamic properties of an electron gas derived with this method take into account two types of electronic transitions and will be a function of the electrons equilibrium temperature. The first component is the intraband or free electrons contribution, that represents the electronic transitions within the partially filled 6s conduction band. These processes contribute with a Drude like component

$$\epsilon_{intra} = 1 - \frac{\omega_p^2}{\omega^2 + i\omega\gamma_{intra}} \tag{2.50}$$

where $\omega_p^2 = Ne^2/\epsilon_0 m$ is the square of the plasma frequency of the electron gas, $2.168 \times 10^{15} Hz$, ϵ_0 is the permittivity of free space, m and $-e$ are the mass and charge of an electron, and γ_{intra} is the intraband damping, due to electron-electron and electron-phonon scattering. γ_{intra} is the inverse of the energy decay time of electrons excited through intraband transitions, and can be written as

$$\gamma_{intra} = a_{intra}\gamma_{ph-e} + b_{intra}(4\pi^2(k_{beta}T_e)^2 + (\hbar\omega)^2) \tag{2.51}$$

a_{intra} and b_{intra} are fitting constants determined while reproducing the experimental gold dielectric permittivity at $T_e = 300K$ from [28], 0.0125/h Hz and 0.0827/h Hz/eV^2, respectively, with h, the Planck constant, equal to $2\pi 4.135 \times 10^{-15} eVs$. T_p is the phonon temperature and k_β is the Boltzamnn constant, $8.61 \times 10^{-5} eV/K$. The subscript $ph - e$ indicates the term accounting for the electron-phonon scattering, which is

$$\gamma_{ph-e} = \frac{2}{5} + 4\frac{T_p}{\theta}\int_0^{\frac{\theta}{T_p}} \frac{x^4}{e^x - 1}dx \tag{2.52}$$

where θ is the Debye temperature, 170 K. The second component is an interband contribution, that can be written as

$$\epsilon_{inter} = K\int_0^\infty \frac{\sqrt{\hbar x - E_g}}{x}(1 - f(x, T_e))\frac{(\gamma_{inter}^2 - \omega^2 + x^2) + 2i\omega\gamma_{inter}}{(\gamma_{inter}^2 - \omega^2 + x^2)^2 + 4\gamma_{inter}^2\omega^2}dx \tag{2.53}$$

Where E_g is the energy gap between the valence and conduction band in gold, 1.98 eV, and E_f is the interband transition energy, 2.4 eV. $f(x, T_e)$ is the Fermi distribution. The electron-electron and electron-phonon cross sections in γ_{inter} are summed to give

$$\gamma_{inter} = a_{inter}\gamma_{ph-e} + b_{inter}\frac{\pi^2(k_\beta T_e)^2 + (E_f - \hbar\omega)}{1 + e^{(E_f - \hbar\omega)/k_\beta T_e)}} \tag{2.54}$$

Again a_{inter} and b_{inter} have been fitted with experimental data and are $0.15/h$ Hz and $0.7/h$ Hz/eV^2. Figure 2.11 shows a schematic of the intraband and interband transitions in gold.

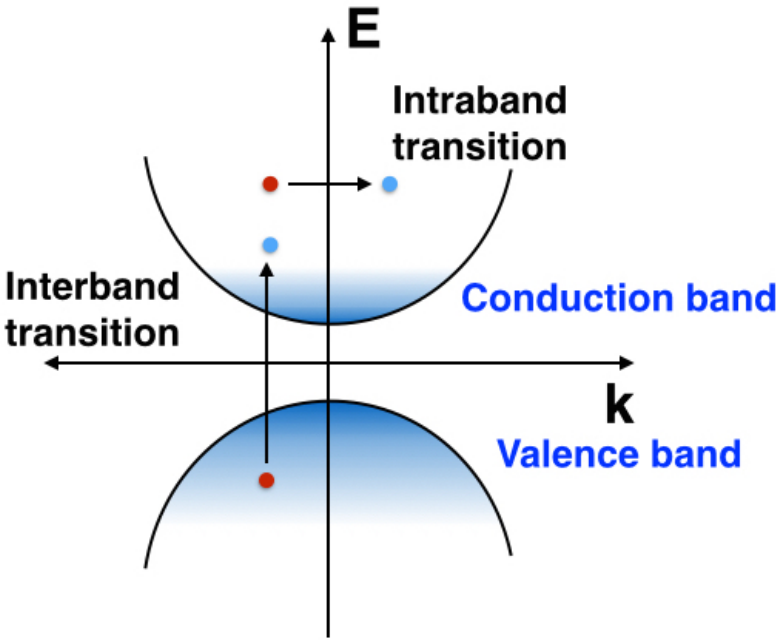

FIGURE 2.11: Graphical representation of interband and intraband transitions. The blue filling represents the states filled by electrons, red circles represent the creation of holes through the optical excitation of electrons.

The evolution of the electrons temperature can be followed using a two-temperature model (TTM). An optical wave dissipates power in the gold, leading to the increase in the electrons temperature. There are then two main relaxation pathways through which the electrons energy is released, electron-electron scattering and electron-phonon scattering [47–52]. The TTM can be derived from Fourier's equation for heat conduction, considering the conservation of energy in

the system. Indicating the electrons temperature as T_e and the phonons temperature as T_p, their evolution is described by the coupled parabolic equations

$$C_e\frac{\partial T_e}{\partial t} = \nabla\dot{(}k\vec{\nabla}T_e) - G(T_e - T_p) + \omega_0 Im[\epsilon] < \vec{E}(\vec{r},t)\vec{E}(\vec{r},t) > \qquad C_p\frac{\partial T_p}{\partial t} = G(T_e - T_p) \tag{2.55}$$

C_e is the electrons heat capacity, and depends upon the electrons temperature as $C_e = \gamma_e T_e$, where $\gamma_e = 67.96 J/m^3K$ [53, 54]. The heat diffusion of electrons depends as well upon the electons and phonons temperatures, being proportional to $k = 318[W/mK]T_e/T_p$. $G = 2^{16}[W/m^2K]$ [54] is the electron-phonon coupling, that determines the speed at which energy is exchanged between the two systems, and $< \vec{E}(\vec{x},t)\vec{E}(\vec{x},t) >$ is the time averaged electric field.

2.4 Summary

In this Chapter I have reviewed the theoretical foundations of the physical principles on which this work will be based. I have described how the nature of Surface Plasmon Polaritons and Local Surface Plasmon Resonances allows to obtain highly confined, enhanced electromagnetic fields associated with the resonances. In the case of LSPRs, I have shown how the spectral position of the optical response of metal nanoparticles can be taylored changing their geometrical parameters.

Isolated, nanometric metallic spheroids sustain two localized plasmon resonances, associated with the oscillation of the conduction electrons along their symmetry axis and along the two equivalent principal axes perpendicular to it. For sufficiently small particles, the resonance fields can be considered as those generated by radiating dipoles, and I have shown qualitatively how the dipole-dipole interaction in an ordered assembly of such nanoparticles leads to new, collective resonant modes, the T and L-mode.

The plasmonic metamaterial studied in this work consists of an array of vertically aligned gold nanorods, embedded in an alumina matrix. The nanorods can be approximated as prolate spheroids, and, similarly to a spheroids assembly,

this metamaterial exhibits collective T and L-modes. The nanorod array can be treated as an effective medium, and I have shown that its resonant optical response can be studied as that of a uniaxial, anisotropic crystal. Tuning the geometrical parameters of the array, the resonant optical response can be engineered across the visible and infrared spectrum.

I have then described the occurrence of nonlinear optical processes in the presence of high light intensities. The enhanced fileds characterizing the plasmonic modes of the metamaterial can be excellent mediators of nonlinear light-matter interactions. I have focused on the possibility to induce a Kerr-type optical nonlinear response in the gold nanorods, i.e. an intensity dependent change in their refractive index. In particular, I have described the ultrafast, electronic contribution to this nonlinear effect in gold in terms of a nonlinear dielectric permittivity, that depends on the temperature of the conduction electrons. This ultrafast variation of refractive index will allow to perform ultrafast light modulation using the gold nanorod metamaterial.

Chapter 3

Numerical modelling techniques

In this chapter I will describe the numerical modelling techniques adopted to reproduce the linear and nonlinear optical response of the nanorod metamaterial studied. In particular, the time evolution of the optical response when the system is exposed to an ultrashort laser pulse.

3.1 Linear optical properties of the nanorod metamaterial

Numerical modelling is essential in order to inspect the microscopic characteristics of the electromagnetic field interacting with the plasmonic metamaterial, together with other effects such as spatial dispersion [55], which are not accounted for in the Effective Medium treatment described in section 2.2.2. We have solved numerically Maxwell's equations inside the gold nanorod metamaterial using a Finite Element Method (FEM) based software, Comsol [56]. As explained in Chapter 2, the metamaterial considered in this thesis is an assembly of vertically aligned gold nanorods, electrochemically grown in an alumina matrix and sustained by a glass substrate. Although the fabrication technique requires the deposition of additional layers on top of the glass substrate, in particular a Ta_2O_5 layer for adhesion and a thin gold layer to be used as the anode for the gold electrodeposition, we have chosen to simplify the system. We consider only the glass substrate, the AAO/nanorod composite and the air superstrate. The presence of the thin

Ta_2O_5 and gold layers does not influence the core modal structure of the nanorod metamaterial. In particular, these layers don't have any effect on the optical extinction features and the gold layer enhances only some features observed through the system's optical reflection. The effect of the presence of a thin gold layer will be examined together with the results for the linear response of the nanorod metamaterial in section 6.1. Figure 3.1 shows, on the left, the schematic of the multilayer analyzed and, on the right, the correspondent system modelled numerically. We have focused on the optical response of our metamaterial to p-polarized light with respect to the glass/metamaterial slab interface, as can be seen from the wavevector and reference system diagram in Figure 3.1. Being in the presence

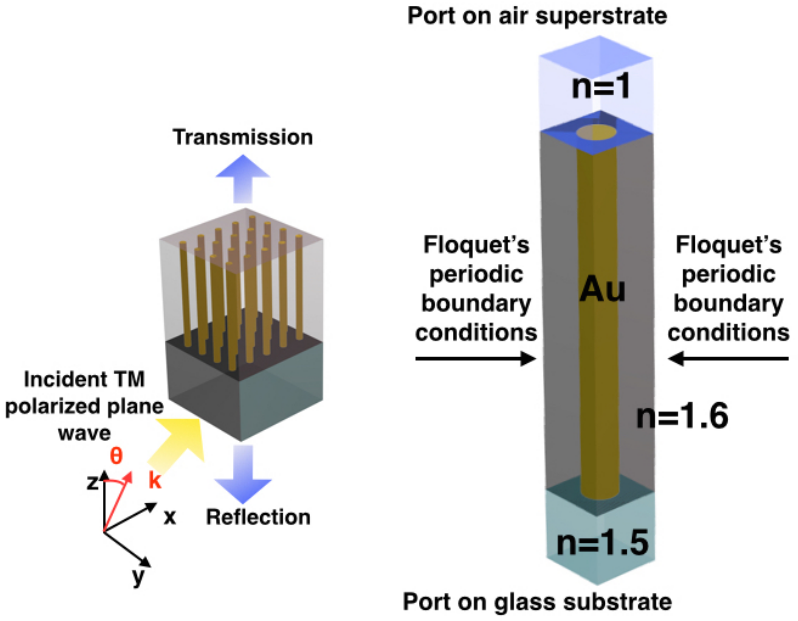

FIGURE 3.1: On the left, schematic of the nanorod/AAO layer modelled sustained by a glass substrate and wavevector of the incident TM polarizd wave. On the right, unit cell modelled numerically, with ports and Floquet's boundary conditions implemented.

of a regular arrangement of nanorods, we have chosen to simulate the unit cell of a square array. We have implemented Floquet's periodic boundary conditions on all sides of the unit cell, and the p-polarized plane wave excitation has been simulated using port boundaries, which allow to compute the optical transmission and reflection via the use of scattering matrix elements.

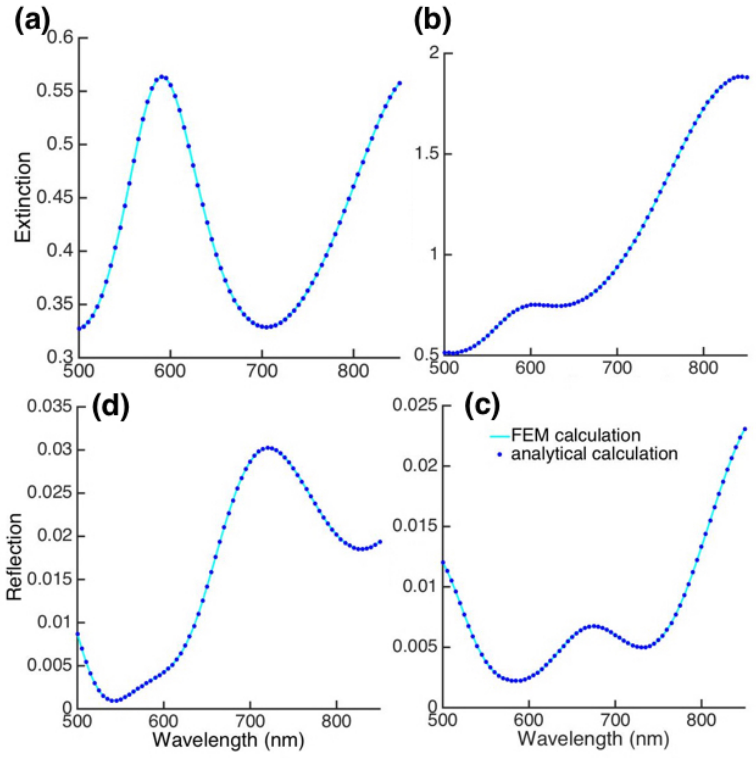

FIGURE 3.2: Comparison between the optical extinction and reflection computed with the FEM and the analytical TMM. The system consists of a homogeneous, anisotropic slab of thickness 350 nm with a refractive index equal to the effective dielectric permittivity calculated according to equation 2.16 and 2.19, with geometrical parameters of 30 nm for the diameter and 90 nm for the interrod distance. (a) and (b) are the optical extinction spectra at 20^o and 40^o incidence, respectively, and (c) and (d) are the optical reflection spectra at 20^o and 40^o incidence, respectively.

The actual nanorod sample is far from being periodic, but has shown to behave very well as an effective medium, so in the far-field, as long as the effective permittivity is the same, the arrangement of the rods in the layer is inconsequential [35].

The validation of the numerical method used has been performed by comparing the optical extinction and reflection obtained using the analytical Transfer Matrix method (TMM) and those obtained using the three-dimensional numerical, periodic model. The extinction of the metamaterial is calculated as -$\log_e$T, where T is the optical transmission through the nanostructure. Thus, the values of the extinction will exceed one.

This comparison has been done in two stages: first, the central layer in the FEM model has been set as a homogeneous, anisotropic layer characterized by a

dielectric permittivity obtained from the Effective Medium homogeneization described in section 2.2.2. This is actually the structure considered in the analytical TMM method. As can be seen in Figure 3.2, the optical response of the multilayer obtained with the numerical calculation matches very well the analytical one, for two significant angles of incidence of the incoming TM polarized plane wave, 20^o and 40^o. This good match has allowed to establish the optimal meshing conditions of the model boundaries and subdomains, enabling to preserve correctly the physics of the system and involving reasonable computational effort.

We have subsequently compared the actual nanorod/AAO composite layer in the numerical model with the analytical TMM computations, in which the metamaterial is still considered as a homogeneous anisotropic slab. We have obtained a very good correspondence between the two models also in this case, as can be seen in Figure 3.3.

The discrepancies between the results obtained with the numerical calculations of the nanostructured gold rod/AAO composite, and the analytical model arise primarily from the nonlocal corrections to the optical response due to the spatial dispersion effects in the plasmonic metamaterial, not captured in the local effective medium approximation [57–59]. These corrections depend on the metamaterial parameters and may be important in both elliptic and hyperbolic dispersion regimes.

3.2 Nonlinear optical properties of the nanorod metamaterial

The nonlinear optical Kerr effect is induced in the gold nanorods by an ultrashort optical pulse. As explained in Section 2.3.1, this ultrafast nonlinearity of the gold has an electronic origin, as the dielectric constant of the metal is dependent on the electron's temperature. The variation of this temperature is determined by the intensity of the control light, and so will be the gold permittivity. The electrons in the conduction and valence band of gold absorb the energy of the optical pump and thus redistribute in energy space, according to the equilibrium

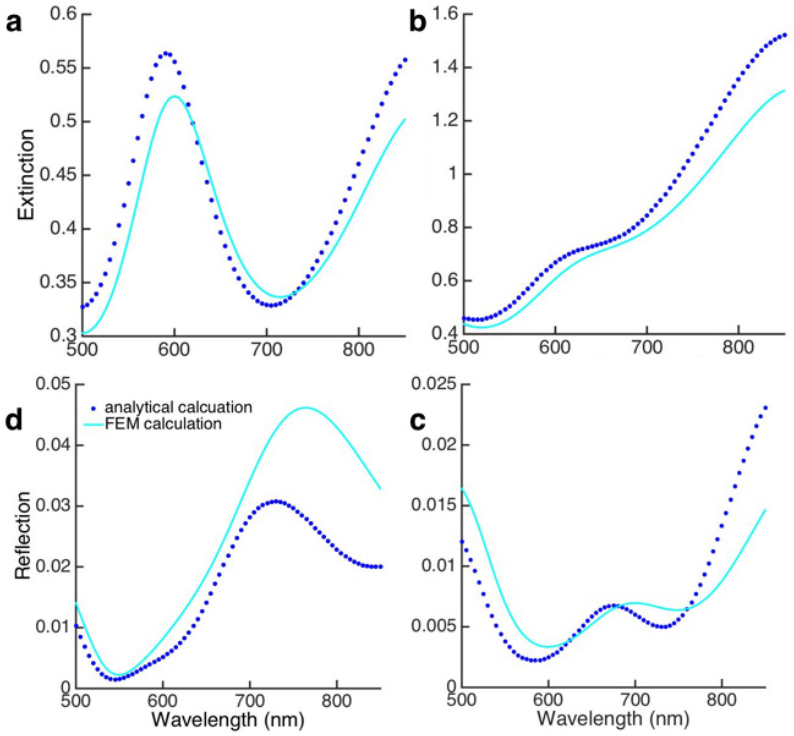

FIGURE 3.3: Comparison between the optical extinction and reflection computed with the Finite Element method (FEM) and the analytical TMM. The system consists of a gold nanorod in AAO for the numerical calculation, and in a homogeneous, anisotropic slab for the analytical calculation. The geometrical parameters of the nanorods, used also to calculate the effective permittivity, are 350 nm for the length, 30 nm for the diameter and 90 nm for the interrod spacing. (a) and (b) are the optical extinction spectra at 20^o and 40^o incidence, respectively, and (c) and (d) are the optical reflection spectra at 20^o and 40^o incidence, respectively.

distribution function at the increased temperature T_e. The dielectric permittivity of gold will change depending on T_e as has been described in section 2.3.1.

Using the same periodic electromagnetic environment described above, we have simulated the ultrashort optical pump pulse as a TM polarized plane wave with a time-dependent, Gaussian-shaped power,

$$P(t) = 0.1e^{\frac{(t-t_0)^2}{\sigma^2}} \tag{3.1}$$

The gaussian envelope is centred at t_0=100 fs, with half duration σ=50 fs.

The electromagnetic power density absorbed by the system is measured every 50 fs, and used as $s(\vec{r}, t)$, the heat source in the Two Temperature Model (TTM),

Equations 2.55. $s(\vec{r}, t)$ is the variable which couples the solver for Maxwell's equations with the numerical solver for the TTM, at increasing time delay from the start of the pump excitation in steps of 50 fs. The electrons temperature evolution is determined at every timestep solving the first of Equations 2.55 numerically. The phonon temperature is effectively kept constant, since phonons have a much higher heat capacity with respect to electrons, and as a consequence their temperature increase during the first few picoseconds is at least two orders of magnitude smaller. We are able to observe the electrons temperature space dependent distribution throughout the optical excitation and relaxation. This distribution is mapped into a space dependent nonlinear dielectric permittivity through equations 2.50 and 2.53. A white light continuum is used to probe the optical reflection and transmission determined by this dielectric permittivity distribution at increasing time delays after the excitation pulse.

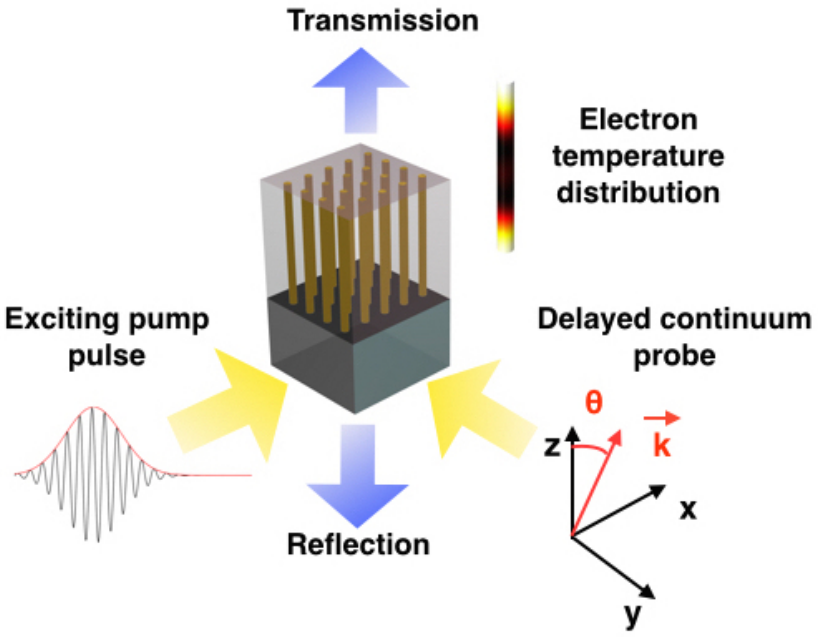

FIGURE 3.4: Schematic of the pump-probe calculation. The gold nanorod metamaterial is exposed to an ultrashort pump pulse, modelled as a TM polarized plane wave with a time dependent, gaussian shaped power. During the optical excitation and subsequent relaxation of the system, the space dependent electron temperature distribution is monitored and mapped into the nonlinear dielectric permittivity. The optical extinction and reflection are then probed at increasing time delay from the optical excitation with a white light continuum.

The thermalization of gold follows three main pathways: electron-electron scattering, electron-phonon scattering and phonon-phonon scattering. Thermalization caused by electron-electron interactions is predominant during a time scale of several hundreds of fs. Subsequently, electron-phonon scattering is the main relaxation process up to several picoseconds while phonon-phonon scattering is the principal process occurring on the timescale of hundreds of picoseconds. In the formulation of the TTM, the electron-electron scattering is considered as an instantaneous process, so the only relaxation channel considered in the model is electron-phonon scattering.

3.3 Summary

In this chapter I have described the modelling techniques used in this work. I have developed a 3D numerical model base on the Finite Element Method to simulate the linear optical response of the nanorod metamaterial to an incident plane wave. The model has been validated firstly comparing the numerical results for the optical response of a homogeneous, anisotropic slab, whith those obtained analytically from the local Effective Medium Theory (EMT), combined with the Transfer Matrix Method (TMM). In this case the results are identical. Considering the complete structure in the numerical simulation, the results for the optical response differ slightly from the analytical calculation, consistently with the increased scattering of the nanostructured material, and the presence of additional propagating modes and nonlocal effects, not captured by the analytical treatment.

I have also developed a three-dimensional model to simulate the nonlinear optical response of the nanorod metamaterial, in particular, to simulate a pump-probe experiment. This model computes the spatial distribution of the energy absorbed by the gold nanorods when exposed to an ultrashort laser pulse, and using the first of Equations 2.55, this distribution is mapped locally into the electrons temperature. The electrons temperature is then used to calculate the nonlinear permittivity of gold with Equations 2.50 and 2.53. The energy absorbed, temperature and dielectric permittivity distributions, and consequently the optical

response of the system are probed at increasing time delay from the pump excitation.

Chapter 4

Plasmonic metamaterials in the Infrared spectral region

In this chapter, I will describe the fabrication technique and illustrate the numerical and experimental, morphological and optical, characterization of a metamaterial consisting of gold nanorods with the effective plasma frequency in the near Infrared (IR) spectral region. The results that will be shown have been published in [60].

4.1 Plasmonics in the Infrared

The near and mid-IR are two extremely interesting spectral regions for a wide variety of applications. IR radiation is absorbed by organic molecules, such as $C_6H_12O_6$ and CO_2, and converted into energy of molecular vibration.

IR spectroscopy is an essential tool in organic chemistry in order to gather information about a sample's molecular composition and coordination and to assess its purity. Spectroscopic chemical sensing is of fundamental importance for environmental control, since greenhouse gases have distinctive absorption features in the IR. The mid-IR is also the key region for finger printing proteins and their abundance, with forseeable applications in personalized health care devices and industrial quality control [61].

Fourier Transform Infrared Spectroscopy (FTIR), widely used for chemical analysis, is characterized in general by a low signal from the analyzed sample. In order to increase the absorption signal, metallic surfaces can be employed. They can enhance the absorption of molecules in the IR (SEIRA) spectroscopy, although the enhancements are modest (10-100) compared to those of surface enhanced Raman spectroscopy (SERS, up to 10^{14}) [62].

SPPs and LSPRs can be also used to enhance the absorption of analytes which have a spectroscopic fingerprint in the IR. The amount of light absorbed by a sample can be increased in two ways using nanostructured plasmonic systems. Plasmons confine the optical field to the surface where the analyte is placed, increasing effectively the light-matter interaction length. Additionally, the nanopatterning maximizes the surface to volume ratio, increasing the number of molecules that can attach to the optically active surface. Extraordinary transmission through subwavelength holes in metallic films mediated by Surface Plasmons has been exploited to increase absorption of molecules in the IR [63]. The presence of Surface Plasmons on metallic meshes of various conformation has shown to facilitate the recording of the absorption spectra of self-assembled monolayers [64], phospholipid bilayers [65] and catalytic surface reactions [66].

Plasmonic systems can also be employed to improve IR detectors, increasing their signal-to-noise level and filtering the light hitting the detector. The signal-to-noise level in an IR detector is high because of its small band gap. Smaller volumes provide lower noise, and the tight field confinement of plasmonic modes can effectively reduce the detection area. Higher material absorption, on the other hand, results in a stronger output signal. The detection area can be minimized by coupling the incident light to surface plasmons and then focussing it with a plasmonic antenna [67]. Alternatively, noise can be lowered by using a quantum-dot detector, and coupling the incident light with a metallic grating [68]. Absorption can be increased by confining the dots in a waveguide and coupling the incident light into one of the waveguide modes. Finally, high effective index modes on the walls of deep subwavelength slots on the surface of a metal can enhance absorption over deep subwavelength volumes [69].

There are several other types of materials, other than plasmonic ones, which have been studied for detection applications and present an efficient optical response in the IR spectral region. For example, metamorphic InGaAs [70], GaSbBt quantum wells and type two superlattices. The plasmonic approach has the advantage of great spectral tuneability and extremely well developed fabrication techniques. Various types of metamaterials have been explored in radio-frequency, terahertz, IR and optical regions based on split-ring resonators, nanorod pairs, coaxial structures [71–73]. The adaptation of the above mentioned approaches at longer wavelengths is straightforward, while their scaling down to the visible spectral range is difficult due to challenging top-down fabrication required at the sub-wavelength scale. In the case of our metallic nanorod based plasmonic metamaterial, the bulk plasma frequency can be easily taylored in the visible spectral region. The gold nanorod metamaterial examined in this work has already shown a great potential in spectroscopic biosensing in the visible spectral region. Sensing of glycerine in acqueous solution and biotin has shown a sensitivity of 30000 nm per Refractive Index unit (RIU) [74], exploiting the tight field confinement of the waveguide modes of the metamaterial slab. The structure of the AAO embedded gold cylinders can be slightly modified by chemical etching, creating a void shell around them. Thus a molecular analyte can be inserted in the void, maximizing its exposure to the enhanced plasmonic field [75]. A sensitivity of 100 nm per RIU has been shown, with a figure of merit of 1. Furthermore, the distance between the nanorods can be selected to match the size of biological species of interest, giving access to a further size selectivity option. Coreshell metamaterials consisting of an ordered array of gold core, palladium shell nanorods have shown more than 30% change in both the reflection and transmission from the metamaterial layer that is observed when the layer is exposed to 2% hydrogen mixture, noticeable to the naked eye as a change in the brightness of light transmitted by the structure [76].

This metamaterial thus constitutes an ideal candiate to optimize IR surface chemical sensing and IR detection, being also compact and easily integrable in existing sensors and detectors. The losses of plasmonic materials are also significantly smaller in the near and mid-IR.

4.2 Fabrication technique

In order to shift the resonant response of the nanorod metamaterial towards the IR, it is essential to fabricate very high aspect ratio nanorods. The technique used to obtain high aspect ratio nanorods, with diameter that can be around 10 nm and 350 nm length, is the same as the one described in Chapter 2, electrodeposition. The gold nanorods are electrodeposited in porous anodic alumina oxide (AAO) templates, synthesized by a two-step anodization process. An aluminium film of 800 nm thickness is sputtered on a multilayer substrate comprised of a glass slide with a 10 nm thick adhesion layer of Ta_2O_5 and a 7 nm thick Au film acting as a weakly conducting layer. The porous alumina structures were synthesized by a two step-anodization in 0.3 M selenic acid at 40-48 V at 0^oC. The anodization conditions determine the diameter and interrod spacing of the AAO matrix, and as a consequence the geometrical parameters of the gold nanorod array. Common electrolytes used in the anodization process are sulfuric acid and oxalic acid, that determine a diameter/period ratio that leads to a response of the nanorods in the visible wavelength range [77–80]. Using selenic acid, the diameter is significantly reduced [79]. Figure 4.1 shows the top-view SEM and AFM images of the self - ordered porous alumina template formed in 0.3 M selenic acid at 48 V keeping the temperature at 0^oC. The minimum diameter of the pores observed in the samples considered in this Chapter is 25 nm with an interpore separation of approximately 115 nm. Figure 4.1 (c) shows the molecules of sulfuric and selenic acid. The low solubility of selenic acid accounts for the much smaller pore diameter observed here.

4.3 Modelling and experimental optical characterization

Two samples of Au nanorods embedded in AAO, A and B, have been fabricated, with different geometrical parameters. Both systems have been designed with the effective plasma frequency in the infrared spectral range. The two samples have the same interrod spacing, 115 nm, measured using SEM. The diameter

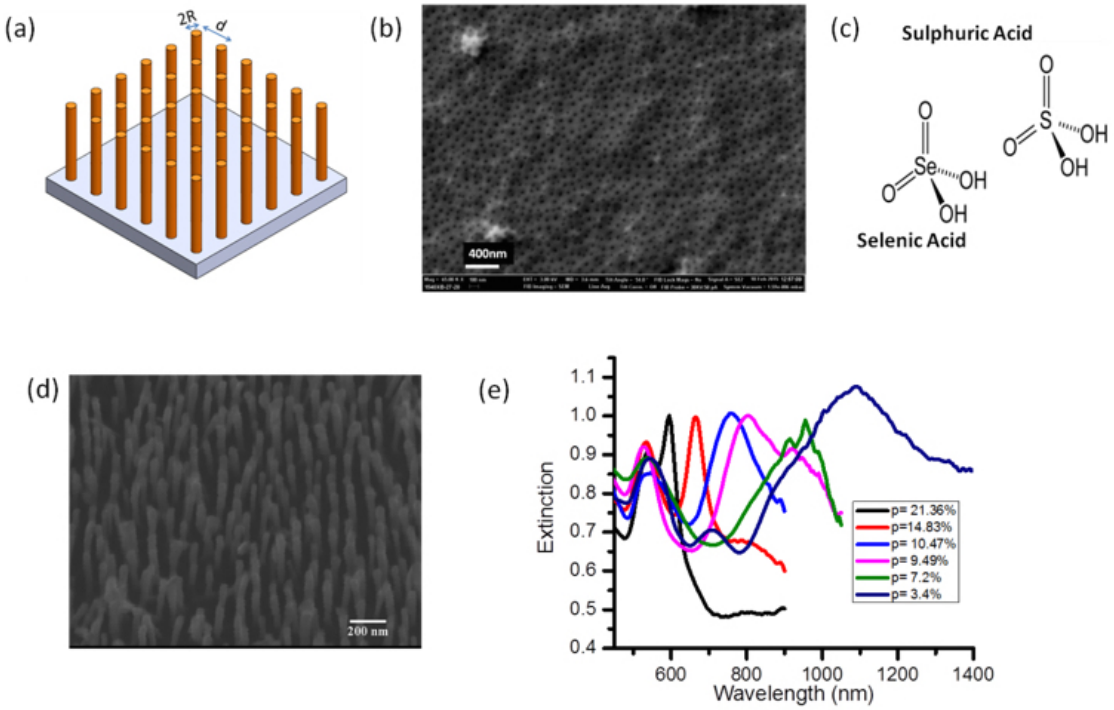

FIGURE 4.1: (a) Schematic of the metamaterial based on a nanorod array. (b) SEM image of porous alumina synthesized in selenic acid at 48 V (Sample B). (d) Comparison of sulfuric and selenic acid molecules. (d) SEM image of the nanorods after removal of alumina matrix (Sample B). Please note that disorder is introduced in the nanorod array after the matrix removal due to the reduced self-supporting properties of thin nanorods. (e) The effect of nanorod concentration on the extinction of the metamaterial (the Au nanorods in AAO matrix, p-polarized light, 40^o angle of incidence).

is 40 nm for sample A and 25 nm for sample B, also extracted from the SEM analysis.

Figure 4.3 (a) and (d) show the measurements of the optical extinction of sample A and B, respectively. The measurements have been performed using a confocal optical setup, fiber coupled with a CCD detector. Figure 4.2 shows a schematic of the experimental setup used. A camera is used to visualize the light beam's position on the sample. Measurements have been performed on two different setups, one for measurements in the visible spectral range and one for measurements in the IR spectral range, with the same structure. The first difference between the two consists in the CCD detector, which is optimized for the visible spectral range for the meausrements between 400 nm and 900 nm, and for the IR for the measurements between 900 and 1600 nm. The second difference consists in the presence of an infrared filter in between the iris and the polarizer,

in the IR setup. Finally, the objective is coupled to the detector via a fiber with transmission in the visible and IR, respectively.

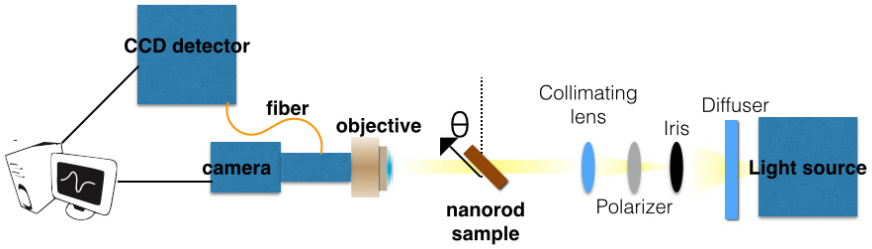

FIGURE 4.2: Schematic of the experimental setup used to perform the linear optical characterization on the nanorod metamaterial samples. The measurements have been performed in two different setups for the visible and IR spectral range. They differ in the CCD and fiber used, optimized for visible and infrared detection, respectively, and in the presence of an infrared filter between the iris and the polarizer.

For both sample A and B, the extinction spectra show the typical two dominating resonances, which are well separated from each other spectrally. The extinction of the metamaterial is calculated as usual as -$\log_e$T, where T is the optical transmission through the nanostructure. Thus the values of the extinction will exceed one. From the analytical and numerical modelling performed it has been possible to infer the height of the nanorods, 200 nm for sample A and 350 nm for sample B, and also the presence of a thick layer of porous AAO on top of the nanorod/AAO slab. Figure 4.3 (b) and (e) show the full vectorial numerical calculation of the metamaterial's optical extinction fitting the experimental measurements, while Figure 4.3 (c) and (f) show the EMT analytical calculation. The frequency dependent dielectric permittivity of the gold for these two samples has been modelled as explained in Chapter 2, and the experimental measurements have been fitted by adjusting the losses in the metal. This adjustment is possible by introducing a restriction for the mean free path of electrons in the gold nanorods with respect to the mean free path in the bulk material. The correction to the dielectric permittivity of the nanorods due to the restricted mean free path will be further explained in Chapter 6. For sample A, the restricted mean free path of electrons used in the modelled gold permittivity is of 23 nm, while for sample B it is of 8 nm.

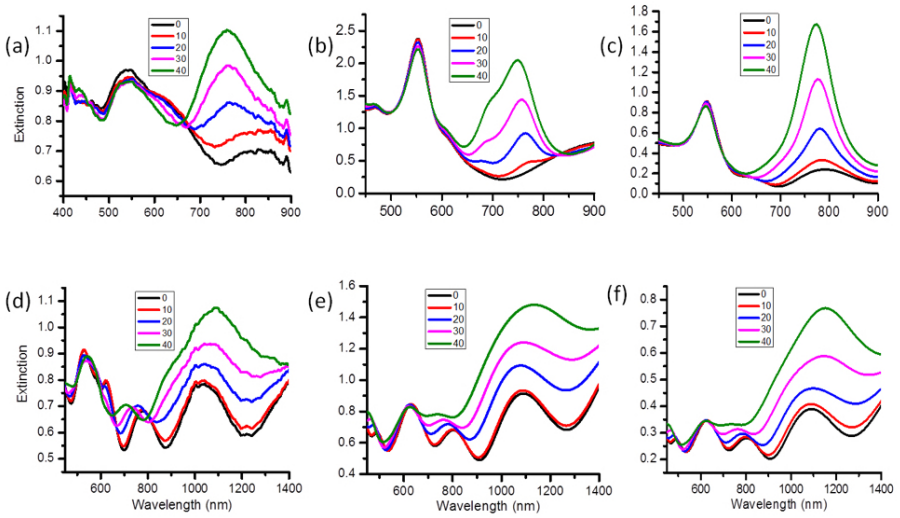

FIGURE 4.3: Extinction spectra of metamaterials A (nanorods of 40 nm diameter, 115 nm period, 200 nm height, embedded in AAO matrix) and B (nanorods of 25 nm diameter, 115 nm period, 350 nm height, embedded in AAO matrix) at different angles of light incidence: (a,d) experiment, (b,e) full-vectorial microscopic modelling, (c,f) EMT modelling. For Sample A an electron mean free path restriction of 23 nm was used for electrochemical Au; the metamaterial has a 7 nm thick Au underlayer and a 700 nm thick AAO overlayer. For Sample B the electron mean free path restriction is 8 nm for electrochemical Au; the metamaterial has a 7 nm thick Au underlayer and a 650 nm thick AAO overlayer.

For smaller nanorod diameters with the same period, the ENZ-related peak is shifted further in the IR spectral range to 1200 nm. This is related to simultaneous increase of the nanorod aspect ratio, thus, the shift of the individual cylindrical surface plasmons on the nanorods to the IR, and a reduction of the coupling between the cylindrical surface plasmons on neighbouring nanorods.

The experimental data is in good agreement with both numerical and EMT modelling, well reproducing the spectral position of the extinction peaks. This allows the extraction of the effective medium parameters of the metamaterial, shown in Figure 4.4.

The discrepancies between the analytical and numerical modelling, can be explained, the same as above, by nonlocality which is not considered in the local EMT used. In particular, for sample A, the restriction to the mean free path of electrons used is quite large, meaning that nonlocal effects are significant, since the losses in the metal are small. The numerical approach is able to capture

this nonlocal behaviour. In the case of sample B, this is less evident, because the restriction path used is much smaller, thus, the losses will reduce the impact of nonlocality. The real part of the effective permittivity components along the

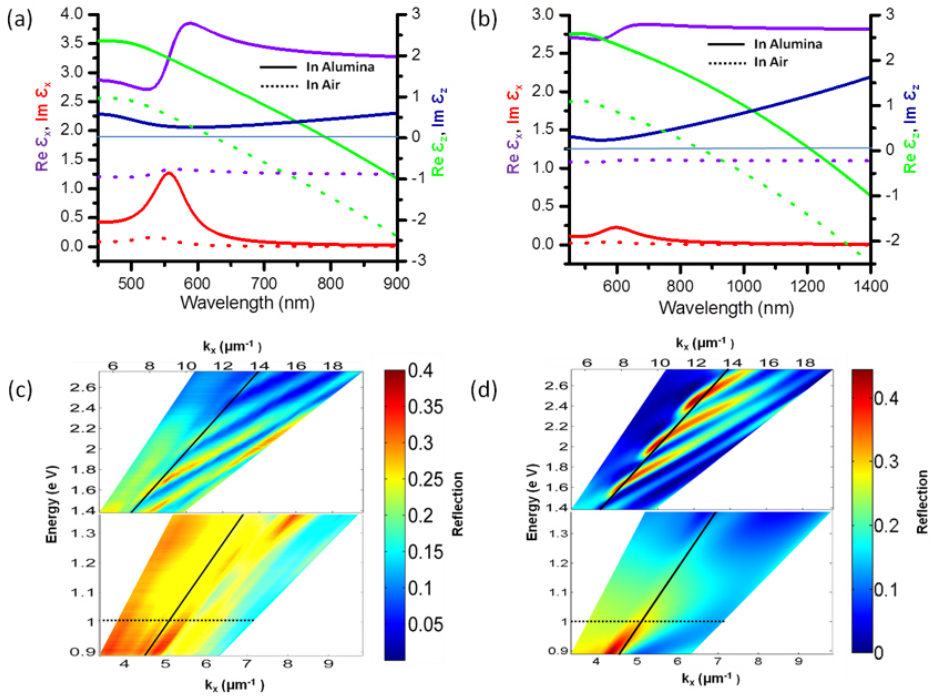

FIGURE 4.4: Effective medium parameters of (a) metamaterial A and (b) metamaterial B. Please note that Im(ϵ_z) curves in AAO and air overlap in (a). (c) Experimentally measured and (d) simulated reflectance dispersions of the metamaterial B. The apparent change of contrast in (c) is due to the change of the detector in the measurements from the visible to IR. The angular range corresponds to 30–70^o in glass. The light line in air and the effective plasma frequency are marked with lines.

ordinary axis of the metamaterial, $\epsilon_{x,y}$, and along the extraordinary axis of the metamaterial, ϵ_z, have the same sign for short wavelengths, where the metamaterials operate in the elliptical dispersion regime, while the effective plasma frequency is reached at wavelengths around 795 nm and 1280 nm for metamaterials A and B, respectively. For longer wavelengths, the metamaterials are hyperbolic, supporting bulk plasmon polaritons [35]. If the AAO matrix is removed so that the nanorods are in air, the bulk plasma frequency is shifted to shorter wavelengths of about 625 nm and 850 nm, for metamaterials A and B, respectively. Still the ENZ

frequency is sufficiently away from the absorption resonance of $\epsilon_{x,y}$. The leaky waveguide modes visible in the experimental measurements and EMT simulations of the optical reflection, visible in total internal reflection in Figure 4.4 (c) and (d), respectively, originate from the presence of the thick porous AAO overlayer. Below the effective plasma frequency, another set of the modes is also seen converging to this frequency from the low frequency range.

4.4 Summary

In this Chapter I have described the fabrication techniques, experimental characterization and theoretical and numerical modelling of a gold nanorod metamaterial with a resonant optical response in the InfraRed spectral region.

I have shown how it is possible to shift the optical response of this metamaterial from the visible to the IR by using high aspect ratio nanorods (with a diameter between 10 and 40 nm and a length between 200 and 350 nm), which have been obtained using selenic acid in the anodization solution.

The nanorod samples have been characterized both in the visible and IR spectral region using a confocal optical setup, depicted in Figure 4.2. The geometrical parameters of the nanorods have been extracted by the SEM images and cross-examined with the numerical and analytical simulations to fit the experimental results. The L-mode resonance for the first sample, sample A, has been measured at 0.8 μm, and the geometrical parameters determined are 40 nm for the diameter, 115 nm for the period and 200 nm for the height of the nanorods. The L-mode resonance for the second sample, sample B, has been measured at 1.2 μm and the geometrical parameters determined are 25 nm for the diameter, 115 nm for the period and 350 nm for the height of the nanorods. The possible applications of these structures are sensing for organic molecules which have their vibrational fingerprint in the IR.

Chapter 5

Core-shell plasmonic metamaterials

To obtain an even more flexible control on the optical properties of composite materials, in this Chapter I will discuss the reliability of the analytical description of the optical response of some configurations of core-shell nanoparticles based metamaterials. Metamaterials consisting of vertically aligned core-shell nanorods and nanotubes have shown a great potential for sensing, being able to selectively expose analytes to the optically active surfaces via changing the shell or wall thickness [81]. Core-shell structures can be easily fabricated with a chemical etching process [75]. Similarly to the case of bare gold nanorods, core-shell naonrods and nanotubes can be approximated as core-shell prolate spheroids. In fact, the analytical treatment that will be used in this Chapter defines a quasistatic polarizability for the individual core-shell nanostructures and uses the effective medium approximation described in Chapter 2 to compute the collective optical response, that will take into account frequency dispersion. The test will be performed comparing the analytical calculation of the optical properties of the core-shell metamaterials with the full numerical one.

I will show that there is a remarkable agreement between the two approaches, also with nanoparticle dimensions that exceed the quasistatic regime. Thus a fast, reliable analytical modelling technique is available over a wide range of geometrical parameters for core-shell nanostructured materials, able to reproduce correctly the

optical response also in the near-IR spectral region.

In the case of silicon-core/gold-shell nanoparticles, it is possible to identify an additional resonance, visible also at normal incidence, spectrally tunable by changing the thickness of the shell, with respect to bare nanorods. The correspondent electromagnetic field is confined in the subdiffraction volume of the inner nanorod, an effect that could be exploited to enhance nonlinear interactions with silicon.

5.1 Effective medium treatment of core-shell nanorod metamaterials

The analytical, quasistatic treatment used to describe arrays of metal nanoparticles embedded in a dielectric medium can be extended to coated particles, i.e. core-shell structures. Again, the attention will be focused on arrays of aligned core-shell nanorods and nanotubes, which will be approximated as prolate spheroids, and the cartesian reference system will coincide with the principal axes of the nanoparticles. I will also compare the optical response of arrays of actual coated spheroids computed with the two approaches. Let us consider an inner spheroid with semiaxes a_1, b_1, c_1 and a concentric outer spheroid with semiaxes a_2, b_2, c_2, embedded in a homogeneous matrix with dielectric permittivity ϵ_m. The outer spheroid has dielectric permittivity ϵ_2 while the inner spheroid has dielectric permittivity ϵ_1. Both are homogeneous and can be considered isotropic or anisotropic. Considering homogeneous and isotropic nanoparticles, the requirements that the scalar electric potential and its first derivative are continuous at the boundaries of the core-shell spheroid leads to the polarizability [19].

$$\alpha_{jj} = \frac{((\epsilon_2 - \epsilon_m)[\epsilon_s + (\epsilon_1 - \epsilon_2)(L_j^{(1)} - L_j^{(2)}] + f_{12}\epsilon_2(\epsilon_1 - \epsilon_2)}{([\epsilon_2 + (\epsilon_1 - \epsilon_2)(L_j^{(1)} - L_j^{(2)}][\epsilon_m + (\epsilon_2 - \epsilon_m)L_j^{(2)}] + f_{12}\epsilon_2 L_3^{(2)}(\epsilon_1 - \epsilon_2))} \tag{5.1}$$

The index jj indicates the diagonal component of the polarizability tensor. The factors L_j are the geometrical factors defined in section 2.2.1. This polarizability can then be used to calculate the isolated particle cross section and the multilayer

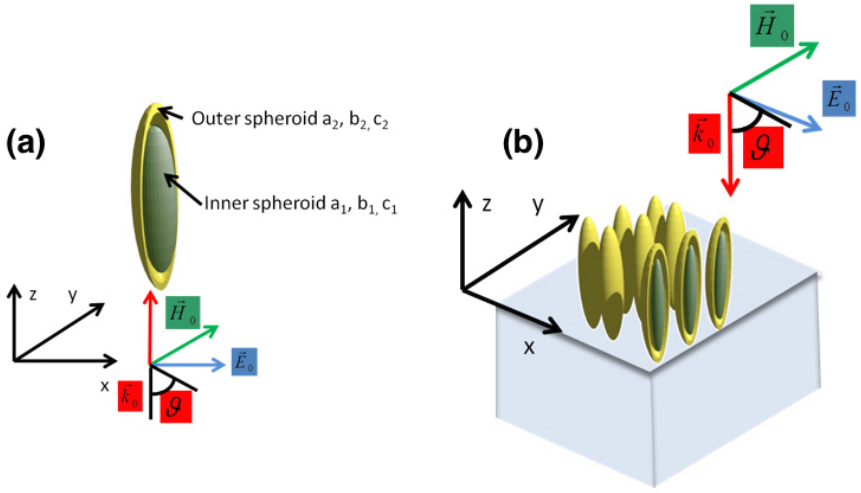

FIGURE 5.1: (a) shows the schematic of the core-shell spheroid approximating the coated nanorod in the Quasistatic regime. (b) shows the system simulated by the Effective Medium Approximation, a square array of core-shell ellipsoids sustained by a glass substrate and the incoming TM polarized plane wave.

structure reflection, transmission and absorption, substituting the polarizability into Equation 2.16. Figure 5.1 shows the schematic of an array of vertically aligned core-shell spheroids, that can be treated with the EMT described in section 2.2.2.

We have focused on the optical response of the core-shell nanoparticles assemblies to plane waves which are TM polarized with respect to the interface between the glass substrate and the slab containing the spheroids in Figure 5.1.

5.2 Silicon-core/gold-coated core-shell systems

Silicon-core/gold-coated structures can be very interesting in the near and mid-IR spectral region, where the intrinsic losses of silicon are effectively negligible. Silicon is also a highly nonlinear material.

The reliability of the effective medium approach has been tested for various arrays of silicon core, gold shell nanoparticles of different dimensions, in order to tune their resonant optical response from the visible to the near-IR spectral region.

The first structure considered is an array of silicon core, gold shell spheroids arranged as in Figure 5.1 and embedded in air, with a glass substrate (n=1.5) and an air superstrate. The geometrical parameters considered, classified as in Figure 5.1, are 20 nm for a_1, 5 nm for b_1 and c_1, 25 nm for a_2, 10 nm for b_2 and

c_2. The center-to-center distance between the spheroids has been changed from 30 nm to 100 nm. Given the dimensions of the nanoparticles, their individual electromagnetic response can be treated within the quasistatic regime. Varying the interparticle spacing, it is possible to test the applicability of the EMT to simulate the electromagnetic response of the core-shell nanoparticle assembly. Figure 5.2 shows the optical extinction of silicon core, gold shell, free standing vertically aligned spheroids, calculated with the analytical EMT just described and with the full numerical, FEM model. The periodic numerical model has been developed as explained in section 3.1, substituting the nanorod with the appropriate core-shell nanoparticle. There is a very good qualitative correspondence between the numer-

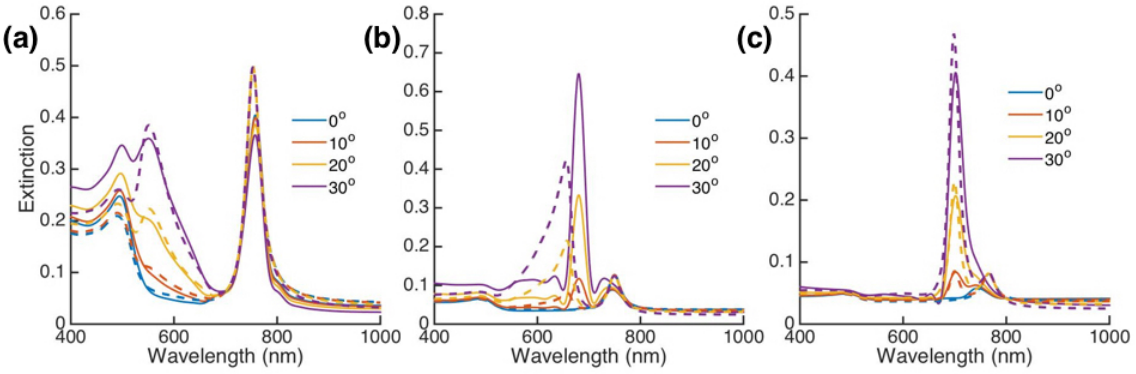

FIGURE 5.2: The solid lines are the numerical calculations of the optical extinction of an array of vertically aligned silicon core, gold coated spheroids, while the dashed lines are the results of the analytical, EMT calculation. The geometrical parameters of the spheroids are 20 nm for the major semiaxis, 5 nm for the minor semiaxis and 5 nm for the shell thickness. The interparticle spacing is 30 nm for (a), 60 nm for (b) and 100 nm for (c).

ical and analytical calculation in all three panels of Figure 5.2. The main resonant features of the extinction spectra calculated numerically are all reproduced by the analytical model. In particular, there are three distinctive features, two of which appear as well at normal incidence and are less affected by the change in the incident wavevector. Moreover, the spectral position of both resonances visible at normal incidence is not affected by the change in the interparticle spacing. On the contrary, the angle dependent resonance is redshifted as the interparticle spacing is increased, as in the case of bare metallic nanoparticles based assemblies.

The profile of the electric field norm corresponding to the resonances observed in the extinction spectrum at normal incidence is shown in Figure 5.3, for an interparticle spacing of 100 nm. The profiles are essentially unchanged for the other interparticle spacings. The profile of the mode around 746 nm is particularly interesting in order to exploit the optical nonlinearity of silicon, since the electromagnetic field is mainly confined into the subdiffraction volume of the inner spheroid. The spectral position of this internal resonance can be tuned by changing the shell thickness to inner diameter ratio of the nanoparticles. Decreasing this quantity, the internal resonance is redshifted.

The spectral position of the resonances calculated with the full numerical model is also very well reproduced by the analytical treatment in the case of an interparticle separation of 30 nm. In the case of larger interparticle spacings, the resonances at normal incidence calculated with EMT are spectrally well superimposed to the ones calculated numerically, while the peaks appearing at non-normal incidence are blueshifted.

The choice of the geometrical parameters of the spheroids in Figure 5.2 has been made in order to be able to treat the particles within the quasi-static limit, i.e. the particles are significantly smaller than the incoming wavelength (20 nm for the major semiaxis, 5 nm for the minor semiaxis and 5 nm for the shell thickness are significantly smaller than the minimum wavelength considered, 450 nm).

The applicability of the analytical approach can be extended outside the quasistatic regime, when the size of the spheroids is increased and the optical response of the assembly is pushed to the near-IR spectral region. I have optimized the size of the semiaxes of the silicon individual spheroids and the thickness of the gold shell in order to obtain a resonant response of the system at 1.5 μm. This wavelength is important because it is a strong absorption line of molecules such as acetylene, for sensing applications of these coreshell systems. Also, it is a very important spectral region for telecommunications and so active manipulation of optical signals. The set of parameters determined is 125 nm for the major semiaxis, 10 nm for the small semiaxes and 350 nm for the center-to-center distance between the spheroids. The shell thickness is of 5 nm. Figure 5.4 (a) shows the spectrum of the

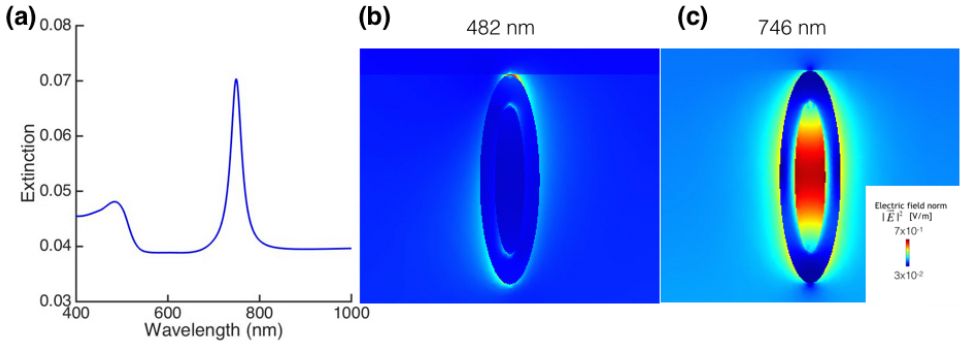

FIGURE 5.3: (a) is the numerically calculated extinction spectrum of an array of silicon core, gold coated spheroids with length of the major semiaxis of the core 20 nm and of the minor semiaxis of the core 5 nm. The angle of incidence of the TM polarized plane wave in the reference system of Figure 5.1 is 0^o. The shell thickness is 5 nm. The interparticle spacing is 100 nm. (b) is the electric field norm profile of a single unit cell of the array at a wavelength of 482 nm and (c) is the electric field norm profile of a single unit cell of the array at a wavelength of 746 nm. The value of the electric field norm at these wavelengths is plotted on a plane parallel to the z-x plane, and passing through the spheroids centre.

array of spheroids at normal incidence. The solid line is the numerical calculation, while the dashed line corresponds to the EMT treatment.

The two calculations match very well from the spectral position point of view. Figure 5.4 (b) shows the electric field norm profile corresponding to the resonance at 920 nm. Similarly to the case of the smaller spheroids, the resonance appearing also at normal incidence corresponds to a confinement of the electromagnetic field in the inner spheroid. Figure 5.5 shows the spectrum of the same system at non normal incidence. The correspondence between the numerical and analytical calculation is not as good as in the case of the normal incidence spectrum, but the EMT response can be corrected via increasing the interparticle spacing from 350 nm to 400 nm. The electromagnetic field norm corresponding to the resonant feature at 1.5 μm is shown in Figure 5.5 (b). The analytical approach is thus very reliable in reproducing the spectral position of the extinction features at normal incidence, and needs some geometrical tuning in the case of non-normal incidence illumination for particle sizes that exceed the quasistatic treatment.

The discrepancies between the analytical and numerical calculations in Figure 5.4 can be explained taking into account the different radiation damping considered

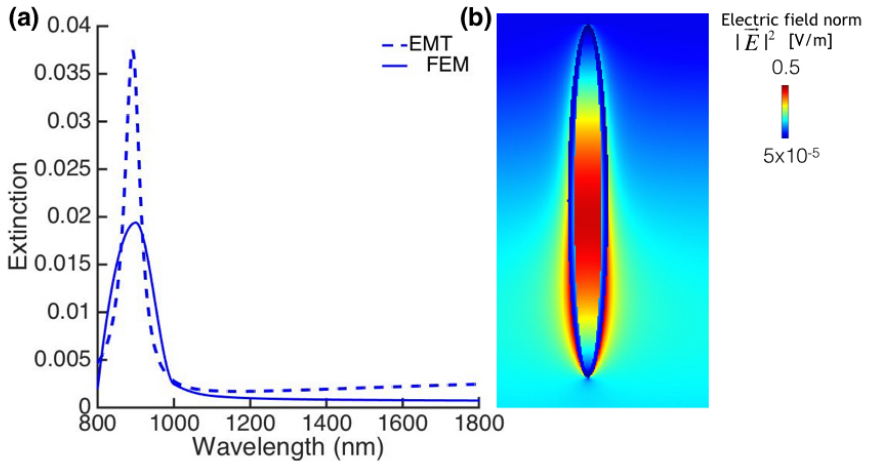

FIGURE 5.4: (a) is the comparison between the optical extinction of an array of silicon core, gold coated spheroids calculated with EMT and FEM. The geometrical parameters have been optimized to obtain a resonant feature at 1.5 μm with FEM at non-normal incidence of the illuminating plane wave, and are 125 nm for the major semiaxis of the core, 10 nm for the minor semiaxis of the core, 5 nm for the shell thickness and 350 nm for the center-to-center distance. The system in this figure is illuminated with a plane wave at normal incidence. (b) is the electric field norm profile at 900 nm for a unit cell of the array. The value of the electric field norm is plotted on a cross section of the spheroid, parallel to the z-x plane and passing through its centre.

in the two approaches. In the EMT, radiating dipoles are considered, with no size associated to them. The FEM takes into consideration the actual size of the particles, and the scattering, absorption and consequently radiation damping will be bigger.

The optimization of the coated spheroid can be a starting point to design a metamaterial consisting of silicon core, gold coated nanorods, with a resonant response in the near-IR. The fabrication technique of such a metamaterial is well developed, for example using Electron Beam Litography (EBL).

We have thus investigated a second core-shell morphology, a silicon core, gold coated nanorod array. The geometry is actually changed only in the numerical calculations, while the EMT still considers the inclusions as coreshell spheroids. The numerical and analytical calculations in the quasistatic regime match very well, as can be seen in Figure 5.6. Also in the case of a nanorod shaped structure, there are three resonant features in the optical extinction spectrum, which are identified both by the analytical and numerical calculation. The resonant features

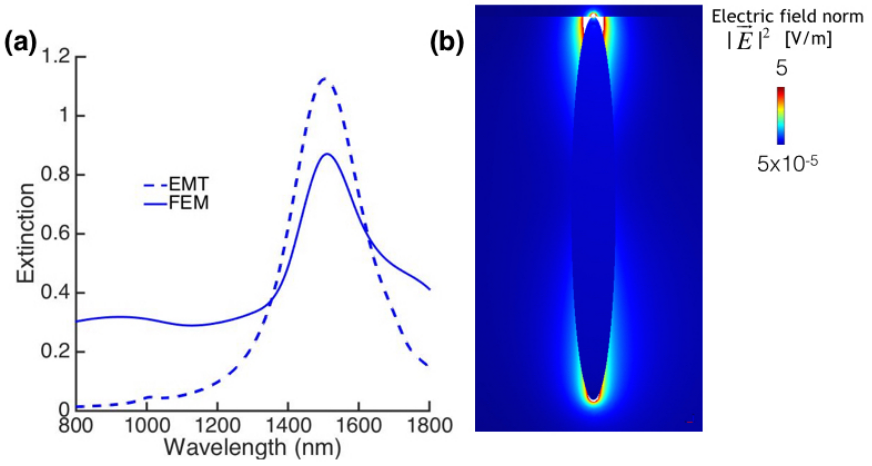

FIGURE 5.5: (a) is the comparison between the optical extinction of an array of silicon core, gold coated spheroids calculated with EMT and FEM. The geometrical parameters have been optimized to obtain a resonant feature at 1.5 μm with FEM, and are 125 nm for the major semiaxis of the core, 10 nm for the minor semiaxis of the core, 5 nm for the shell thickness and 350 nm for the center-to-center distance. The geometrical parameters have been changed in the EMT calculation to fit the numerical results, with the interparticle spacing changed to 400 nm. The system is illuminated with a plane wave at 30^o incidence. (b) is the electric field norm profile at 1500 nm for a unit cell of the array. The value of the electric field norm is plotted on a cross section of the spheroid, parallel to the z-x plane and passing through its centre.

at 520 nm and 800 nm appear at normal incidence, wihle the feature at 720 nm appears only at non-normal incidence. The field profiles corresponding to the resonances are different from those identified for the spheroid assembly. In particular, the electromagnetic field appears to be confined also to the silicon nanorod in the case of the resonance appearing at non normal incidence. With this particular choice of parameters though, the two resonances are effectively merged, as can be seen in the extinction spectrum of Figure 5.6 (a). We have calculated the optical extinction of a silicon core, gold coated nanorod with the same geometrical parameters used to tune the resonant response of the silicon core spheroid towards 1.5 μm. The optical extinction of the numerical calculation is shown in Figure 5.7 (a). The EMT calculation is again fitted reducing the shell thickness from 5 to 3.7 nm. The agreement in the spectral position of the resonance at 1.5 μm is good, but the EMT fails in identifying one of the features of the numerically calculated spectrum. The field of the resonance around 940 nm in the numerical spectrum, which corresponds to the internal resonance of

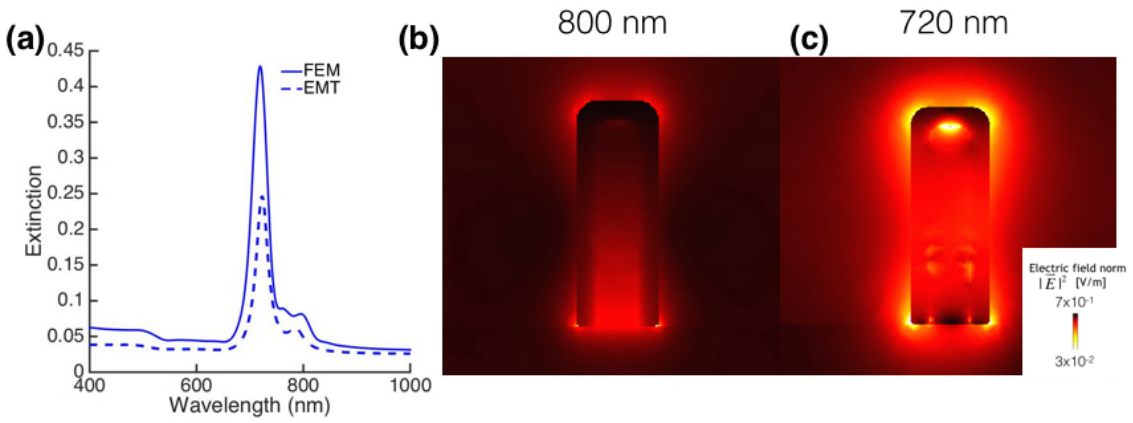

FIGURE 5.6: (a) Optical extinction of an assembly of vertically aligned coreshell spheroids calculated with EMT (dashed line) and of silicon core, gold coated nanorods calculated with the numerical model (solid line), for an illuminating TM polarized wave at 30^o incidence. (b) Electric field norm profile for the resonance at 800 nm for a unit cell of the array. (c) Electric field norm profile corresponding to the rsonance at 720 nm for a unit cell of the array. The value of the electric field norm at these wavelengths is plotted on a cross section of the spheroid, parallel to the z-x plane and passing through its centre. The geometrical parameters considered are 40 nm for the length of the nanorod and major axis of the spheroid, 5 nm for the radius of the nanorod and the minor semiaxis of the spheroid, 100 nm for the interparticle spacing and 5 nm for the shell thickness.

the spheroid, doesn't have the same strong confinement in the inner silicon core. It appears to be a higher-order multipolar resonance of the metallic shell. The discrepancies between the analytical and numerical calculation can in this case be mainly explained considering the different shapes of the systems considered. In the numerical calculations, the silicon nanorods have sharp edges, which determine increased scattering.

Finally, we have considered how the quasistatic polarizability description and the numerical modelling can describe a third type of core-shell structure, a silicon core, gold coated nanotube. The schematic of the structure is shown in Figure 5.12 (c). Again, we have initially considered nanotubes with dimensions within the quasistatic approximation. Figure 5.8 shows the extinction spectra of silicon core, gold shell nanotubes computed analytically and numerically, considering a length of 40 nm for the nanotube, equal to the major axis of the inner spheroid in the quasistatic approximation, a diameter of 10 nm, equal to the minor axis of the inner spheroid, and a shell thickness of 5 nm. The ellipsoids have a nonhomogeneous

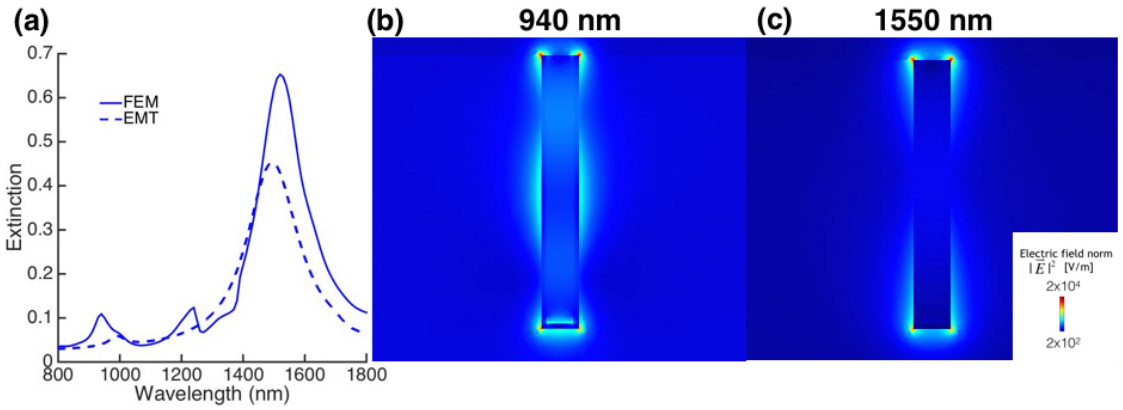

FIGURE 5.7: (a) Optical extinction of an assembly of vertically aligned core-shell spheroids calculated with EMT (dashed line) and of silicon core, gold shell nanorods computed with the numerical model (solid line), for an illuminating TM polarized wave at 30^o incidence. (b) Electric field norm profile for the resonance at 940 nm for a unit cell of the array. (c) Electric field norm profile corresponding to the resonance at 1550 nm for a unit cell of the array. The value of the electric field norm at these wavelengths is plotted on a cross section of the nanorod, parallel to the z-x plane and passing through its centre. The geometrical parameters considered are 250 nm for the length of the nanorod and major axis of the spheroid, 10 nm for the radius of the nanorod and the minor semiaxis of the spheroid, 350 nm for the interparticle spacing and 5 nm for the shell thickness.

shell in the EMT, so that the major axis of the outer ellipsoid is also set as 40 nm.

There is a good qualitative correspondence between the analytical and numerical calculations for all the three interparticle spacings considered. Again, the three features that could be identified also in the case of silicon core, gold coated spheroids are captured by the EMT treatment. A resonance in the extinction spectra at 747 nm is present at all angles of incidence for all the three geometrical configurations, and its spectral position and absolute value is not affected by the change in the wavevector. In the case of the 100 nm interrod spacing, it is merged with the dipolar-type resonance peak appearing at non-normal incidence. The field profile corresponding to the resonances present in the extinction spectra is shown in Figure 5.9, for an interrod spacing of 100 nm, although the characteristics of the field profiles can be generalized for all three configurations. Similarly to the case of the coated spheroid, the resonance appearing at 747 nm at normal incidence has a field confined mainly in the inner silicon core.

In the case of the 30 nm interrod spacing, the spectral position of both the

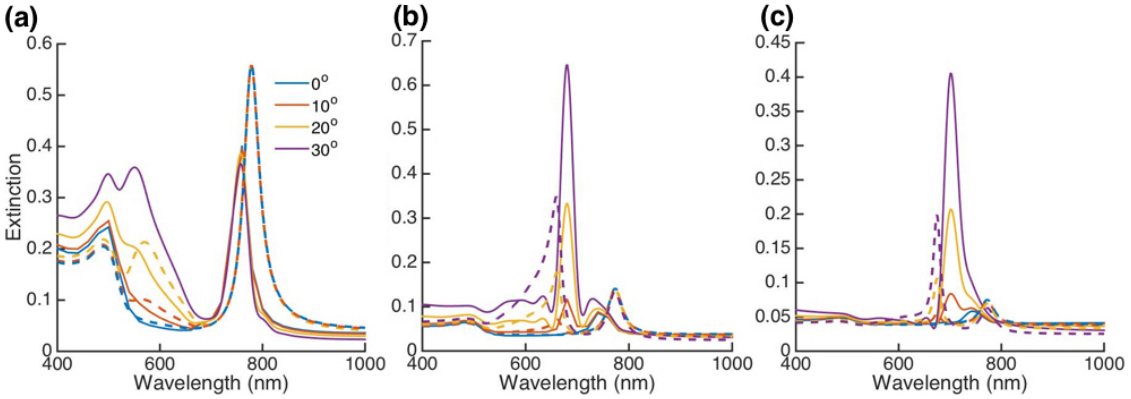

FIGURE 5.8: Square array of silicon core, gold coated nanotubes, with length of 40 nm, diameter 10 nm, shell thickness of 5 nm, variable period. The homogeneous medium between the particles is air, n=1. The array is assumed to be on top of a glass substrate. A plane wave is inciding from the air superstrate at 30 deg incidence. Here we compare the calculation of the extinction spectra for different periods, (a) 30 nm, (b) 60 nm, (c) 100 nm, obtained with EMT (dashed lines) and FEM (solid lines).

angle independent resonance and of the dipolar resonance computed with EMT is redshifted with respect to the numerical ones. In the case of the other two interrod spacings, the angle independent resonance spectral position computed analytically is redshifted with respect to the numerical one, but the dipolar resonance is blueshifted. The discrepancies between the analytical and numerical calculations in this case have to be analyzed in the context of the interaction between the nanostructures. The effect of the scatteirng from neighbouring particles is greater in the case of the numerical model.

Finally, we have analysed how the EMT can reproduce the optical response of an array of core-shell nanotubes with geometrical parameters that exceed the quasistatic limit. We have thus calculated analytically and numerically the optical extinction of an array of silicon core, gold coated nanotubes with a length of 300 nm, a diameter of 10 nm and a shell thickness of 5 nm. Figure 5.10 shows the results for three different interrod spacings. The EMT approximation reproduces very well the numerical results at normal incidence, while the spectral position of the logitudinal resonance calculated analytically is slightly redshifted with respect to the numerical one. The discrepancies can be explained with the different geometries considered in the analytical and numerical model (spheroids and tubes,

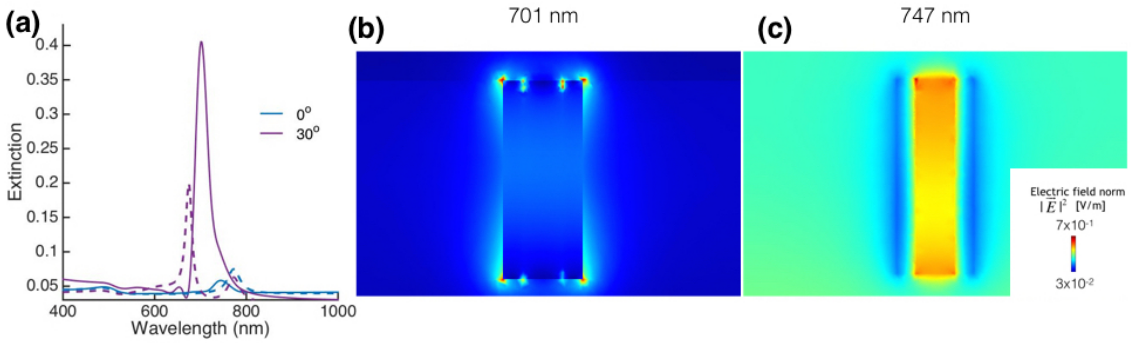

FIGURE 5.9: Square array of silicon core, gold coated nanotubes, with length of 40 nm, diameter 10 nm, shell thickness of 5 nm, period 100 nm. The homogeneous medium between the particles is air, n=1. The array is assumed to be on top of a glass substrate. A plane wave is inciding from the air superstrate at 30^o incidence. (a) shows the calculation of the extinction spectrum for a 100 nm period obtained with EMT (dashed line) and FEM (solid lines) (b) shows the field profile at 701 nm and (c) shows the field profile at 747 nm for a unit cell of the array. The value of the electric field norm at these wavelengths is plotted on a cross section of the spheroid, parallel to the z-x plane and passing through its centre.

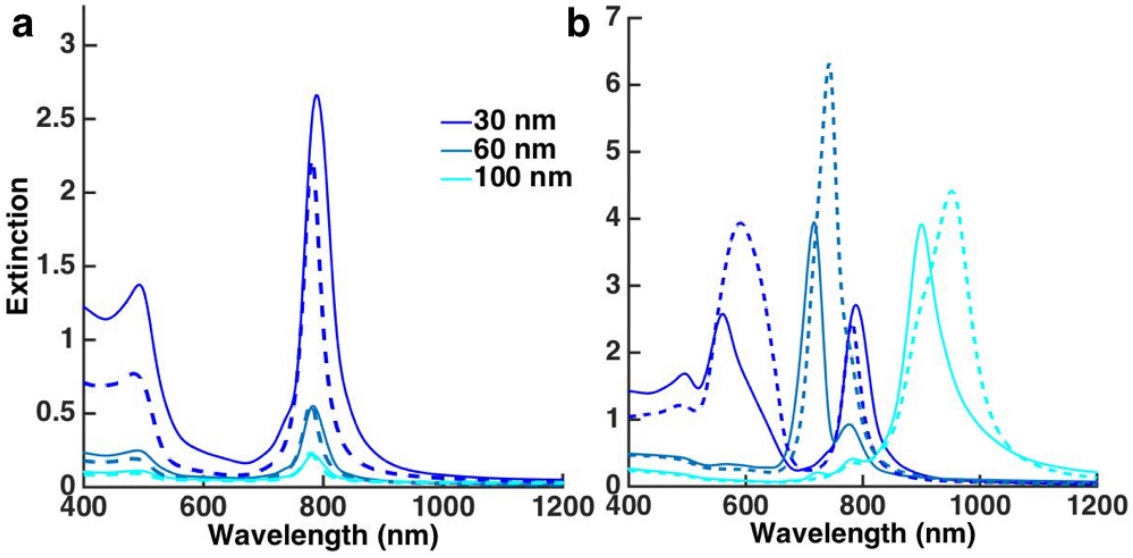

FIGURE 5.10: Comparison between the numerical calculation (solid lines) and the analytical calculation (dashed lines) of the optical extinction of a square array of silicon core, gold coated nanotubes. The geometrical parameters are 300 nm for the length of the tubes, 10 nm for the inner diameter and 5 nm for the shell thickness. The inter-rod spacings have been varied according to the legend. (a) shows the extinction of the system at normal incidence, while (b) shows the extinction of the system at 30^o incidence.

respectively).

5.3 Empty core-shell structures

The analytic, effective medium treatment of core shell assemblies can be extended to other coreshell structures. Figure 5.11 shows the optical response of an array of free standing air core, gold coated ellipsoids for three different interparticle spacings and various angles of incidence of the incoming TM polarized light. As mentioned in the introduction, concentric tubular coreshell structures can be

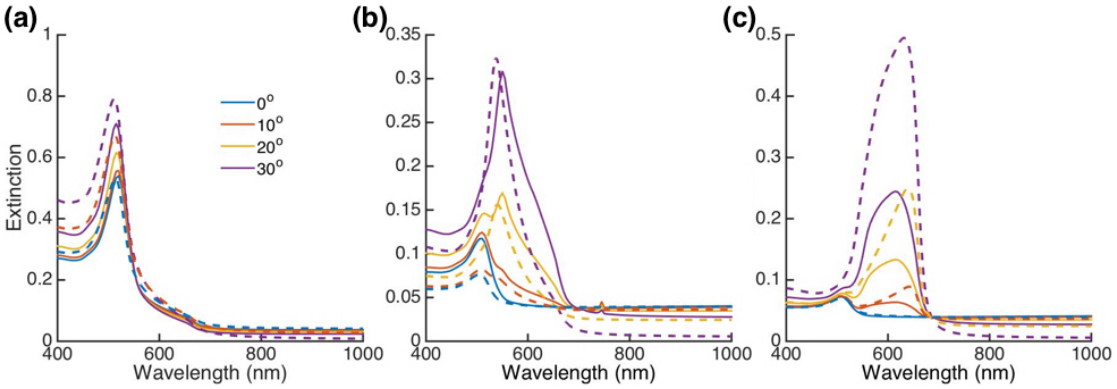

FIGURE 5.11: The solid lines are the numerical calculations of the optical extinction of an array of air core, gold coated vertically aligned spheroids, while the dashed lines are the results of the analytical, EMT calculation. The geometrical parameters of the ellipsoids are 40 nm for the major axis, 10 nm for the minor axis and 5 nm for the shell thickness. The interparticle spacing is 30 nm for (a), 60 nm for (b) and 100 nm for (c).

easily fabricated via chemical etching. Here, we consider two coreshell tubular structures, shown in Figure 5.12 (a) and (b). In the case of small nanotubes, that still can be treated within the quasistatic approximation, the features of the optical extinciton spectra are similar to those of the core-shell spheroids. Figure 5.13 shows the comparison between the analytical and numerical calculation of the extinction spectra of an array of small gold core, air shell nanotubes. Also in the case of longer nanotubes, which exceed the quasistatic treatment, the core-shell EMT reproduces very well the numerical calculations. Figure 5.14 shows the comparison between the numerical and analytical calculation of the extinction spectra of 300 nm long gold core, air shell nanotubes. Figure 5.15 shows the comparison between the analytical and numerical calculation of the extinction spectra of an

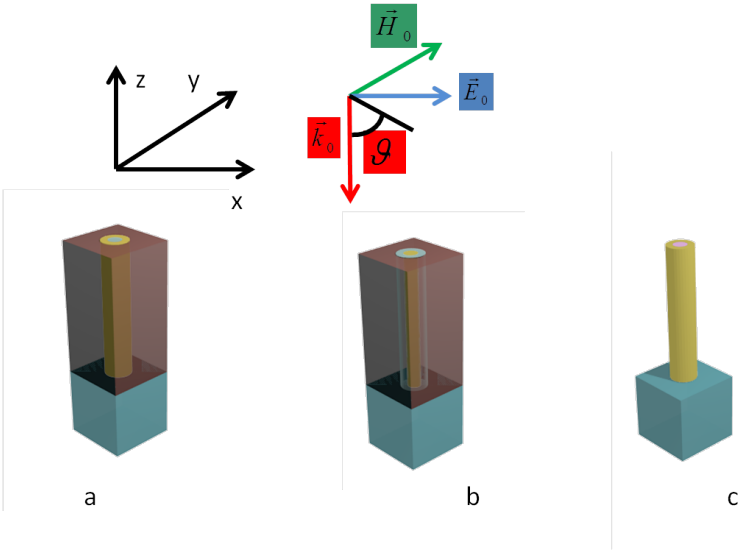

FIGURE 5.12: Schematic of the three core-shell structures considered. (a) is a hollow gold tube embedded in AAO, (b) is a gold nanorod surrounded by an air filled shell and embedded in AAO and (c) is a silicon core, gold coated nanotube. The reference system on top shows an incident TM polarized plane wave.

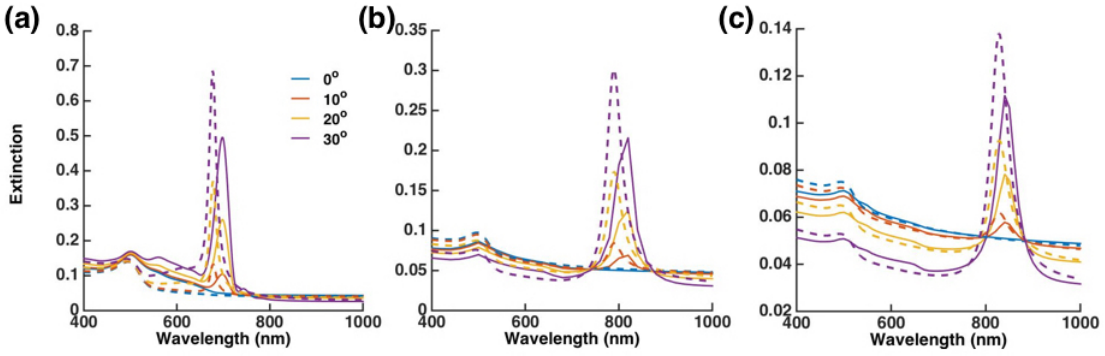

FIGURE 5.13: Square array of gold core, air shell nanotubes, with length of 40 nm, diameter 10 nm, shell thickness of 5 nm, variable period. The homogeneous medium between the particles is AAO, n=1.6. The array is assumed to be on top of a glass substrate. A TM polarized plane wave is inciding from the air superstrate. Here we compare the calculation of the extinction spectra for different periods, (a) 30 nm, (b) 60 nm, (c) 100 nm, obtained with EMT (dashed lines) and FEM (solid lines).

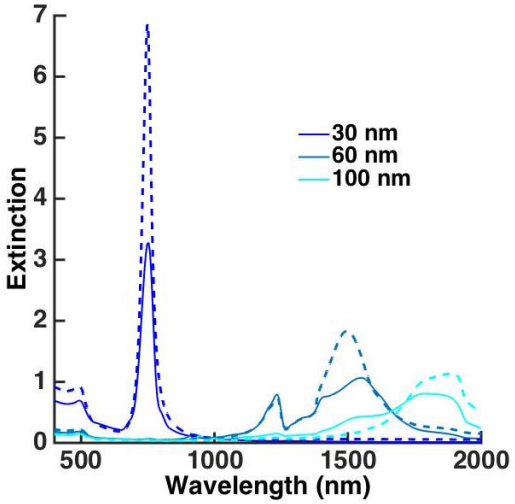

FIGURE 5.14: Comparison between the numerically computed (solid line) and analytically computed (dashed line) extinction of a square array of gold core, air shell nanotubes, for an incident TM polarized plane wave at an angle of 30^o. The geometrical parameters of the array are 300 nm for the tube length, 10 nm for the inner diameter and 5 nm for the shell thickness, for various interrod spacings indicated in the legend.

array of air core, gold shell nanotubes ambedded in AAO, for a 30^o incident TM polarized plane wave. The nanotubes are 300 nm long, and the interrod spacing is varied in order to show how the resonance can be easily shifted towards the near-IR. Core-shell structures allow to easily shift the resonant optical response

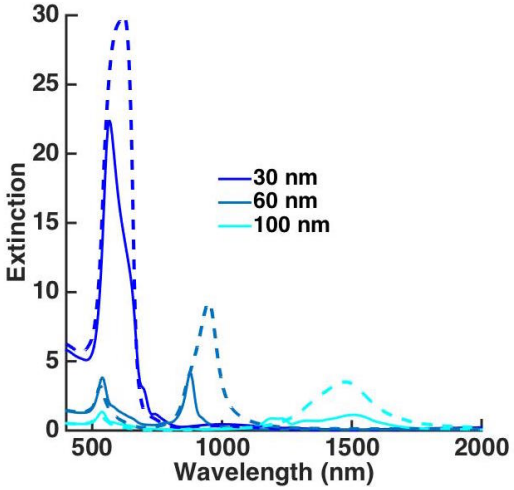

FIGURE 5.15: Comparison between the numerically computed (solid line) and analytically computed (dashed line) extinction of a square array of air core, gold shell nanotubes, embedded in AAO, for an incident TM polarized plane wave at an angle of 30^o. The geometrical parameters of the array are 300 nm for the tube length, 10 nm for the inner diameter and 5 nm for the shell thickness, for various interrod spacings indicated in the legend.

of the metamaterial towards the mid-IR, both decreasing the shell thickness to diameter ratio and increasing the separation between the nanotubes. This can be seen using a gold core, air shell nanorod metamaterial and also an air core, gold shell metamaterial. In the case of a plane wave illuminating the nanotubes array at normal incidence, the comparison between the numerical and effective medium treatment is excellent. In the case of non normal incidence, the agreement using the exact same geometrical parameters is as well significant. This has been tested for a wide variety of geometrical parameters and illumination conditions. This analytical approach is thus a reliable tool to design coreshell metamaterials with a resonant response in the near and mid-IR.

5.4 Summary

In this Chapter I have modelled the optical response of various core-shell nanorod plasmonic metamaterials, both numerically and using the effective medium approach.

The silicon core, gold shell structures have shown an additional resonance, visible also at normal incidence, with respect to the bare gold nanorod metamaterial. Considering the internal and external surfaces of the metallic shell as interacting dipoles, two resonances will occurr, one 'internal' and one 'external' resonance. The enhanced field profile corresponding to the internal resonance is confined in the core structure, and could be used to mediate nonlinear effects in silicon. Its spectral position is determined once the diameter to shell thickness ratio is fixed. The spectral position of the 'external' resonance, can be varied changing the parameters of the nanorod array as a whole, and thus has a similar origin to that of the L-mode in the bare gold nanoros system.

The structure of gold nanotubes and gold core, void shell nanorods is particularly suitable for sensing applications, since the optically active surface exposed to the analyte can be maximized. I have shown how the effective medium theory, modified for the coreshell structure, can reproduce remarkably well the features of the optical response of all these systems, and their spectral position, having compared the analytical results with the numerical calculations. Moreover, the

geometrical parameters of the metamaterial can be tuned in order to shift the resonant response towards the IR spectral region.

Chapter 6

Ultrafast nonlinear plasmonic metamaterials

As seen in the previous Chapters, plasmonic nanoparticles and metamaterials determine the enhancement of the electromagnetic field and its confinement over subdiffraction volumes. This characteristic is particularly suitable to enhance inherently weak nonlinear light-matter interactions, and exploit their reversible, ultrafast character.

In this chapter I will focus on nonlinearities that originate from the metallic components of the plasmonic structures. To achieve the optical signal modulation using these structures, either the plasmonic resonance can be shifted via an induced change in the refractive index of the metal, or absorption at the plasmonic resonance can be increased or decreased [82].

These effects take full advantage of the resonant behavior of plasmonic systems. For example, the resonant transmission of Surface Plasmon Polaritons (SPPs) modes in Al-Si waveguides was shown to reach modulation depths on the order of 7.5% on a timescale of around 200 fs. In this work, the propagation of a pulsed SPP, with a frequency corresponding to a 780-nm free-space wavelength, is modulated via an optical pump fluence on the order of 10 mJ/cm^2 that alters the metal's refractive index through an optical Kerr process. This modifies the SPP intensity and propagation length, leading to the observed signal modulation [83].

In another example, the coupling efficiency of an SPP to a thin gold film covered by a PMMA grating has been modulated between 10 and 60% on a timescale of 700 fs. The coupling efficiency is controlled by the SPP-mediated nonlinear changes in the gold film refractive index, and monitored by measuring the zero order reflection of the system. The laser control signal is at 775 nm, while the modulation is observed between 603 nm, where the plamson resonance is located, and 623 nm. The maximum modulation is obtained with a fluence of 60 mJ/cm^2 [84].

Two-photon absorption is the mechanism driving the nonlinear response of a gold film patterned with split ring resonators. This metamaterial has been reported to achieve a modulation of up to 40% with a fluence of the optical control pulse of 270 μJ/cm^2 and a recovery time estimated as 40 fs for the signal light around the plasmonic resonance of the system, located at 890 nm, at a control wavelength also of 890 nm [85].

Nanorod-based metamaterials have also shown promising performances for free-space optical functionalities. As a waveplate, they are potentially able to control the polarization of plane waves over sub-picosecond time scales in different dispersion regimes (hyperbolic, elliptic and epsilon-near-zero) by means of the nonlinear response of the metal [86].

Previous work has experimentally shown strong, ultrafast response of a metamaterial made of gold nanorods embedded in an Al_2O_5 matrix under femtosecond excitation. A maximum change in transmission of 80% with sub-picosecond recovery time and a corresponding pump fluency of 7 mJ/cm^2 has been addressed to enhanced nonlinearity due to plasmonic nonlocal effects [87].

In this chapter, I will use the numerical model developed in Chapter 3 to simulate the ultrafast nonlinear response of a plasmonic nanorod metamaterial. The Kerr optical nonlinearity will be used to determine an intensity-dependent variation of the refractive index of gold, and so a variation of the effective permittivity of the metamaterial. This time-dependent geometry of the metamaterial and its associated optical response will in this way be effectively modified on an ultrafast timescale.

First, I will analyze the linear optical properties of the plasmonic metamaterial, accounting for the nonlocal effects exhibited by the structure.

Secondly, I will analyze the nonlinear optical properties of the metamaterial. Its rich modal response will be explored in order to estimate performances. This will be done through a consistent and methodical approach accounting for the effects from a pump beam, whose role is to modify the optical properties of the metamaterial through a nonlinear interaction, on a probe beam, whose role is to characterize the associated time-dependent changes in the optical properties. The particular effects originating from the dynamics of the electrons temperature on the measured optical properties will be considered as a function of several key parameters governing the energy relaxation dynamics at the nanoscale. For example, the role of inhomogeneities in the spatial electrons temperature distribution inside the nanorods after being illuminated by the pump will be inspected. The TTM model will also be used to reproduce experimental results obtained previously [87] and to generally reconduct the behavior of the nonlinear response to the effective medium treatment of the metamaterial.

The ultimate goal is that of integrating the metamaterial in an optical device. Practical solutions to the realization of nonlinear optical devices with this gold nanorod metamaterial have been already studied. For example, integrating this metamaterial with an on-chip silicon waveguide geometry was shown to provide efficient and ultrafast modal modulation and switching capabilities. Here, the metamaterial's hyperbolic modes are hybridized with the modes supported by the silicon waveguide, and controlled optically at the picosecond timescale to achieve modulation depths of 35%, at an operational wavelength of 1.5 μm. The process is driven by an optical pump at 532 nm, overlapping the metamaterial's transverse plasmonic resonance. The switching mechanism is due to the nonlinear variation of the refractive index of gold in the hybridized metamaterial-waveguide system, which determines a change in the characteristics of the hybrid eigenmodes [88]. This structure is in the process of being patented [89]. Another highly integrated all optical modulator has been studied, exploiting the high reflectivity and the strong nonlinear properties belonging to the ENZ regime of the gold nanorod

metamaterial. The high reflectivity of an ENZ metamaterial layer is used to construct a resonant optical cavity, which can be optically controlled. The nanorod dimensions can be varied to selectively allow the transmission of modes in a silicon waveguide. In particular, the nonlinear metamaterial can modulate the transmission of the TM mode of the waveguide at 1.55 μm. This device is also in the process of being patented [90]. Throughout this chapter, the optical extinction of the metamaterial will be defined as -$\log_e$T, where T is the optical transmission through the metamaterial (transmitted flux of the electromagnetic field divided by the incident flux), while the reflection will be defined as the ratio between the reflected flux and the incident flux.

6.1 Linear response of the nanorod metamaterial

We have calculated numerically the optical extinction and reflection spectra of the metamaterial in the linear regime, for wavelengths between 450 nm and 1500 nm and angles of incidence bewteen 0^o and 90^o. The nanorod metamaterial is illuminated with a low-intensity TM polarized plane wave, inciding from the glass substrate. Figure 6.1 is the schematic of the system and of the illuminating wavevector and electric field.

Figure 6.2 (a) shows the extinction linear dispersion, while (b) shows the linear reflection dispersion. The extinction dispersion shows three peaks. The dispersionless mode visible at 2.4 eV (wavelength 520 nm), is the T-mode, which has the character of a localized mode. The other two peaks between between 1.5 and 1.65 eV (wavelength 830 nm and 750 nm, respectively) are both due to the highly dispersive L-mode of the nanorod assembly. Not only the spectral position, but also the amplitude and shape of the L-mode have a strong dependence on the incident light wavevector. The origin of the T and L-modes has been explained in Chapter 2.

In the reflection dispersion, there is a series of minima between the light line in air and the light line in glass. These modes have a negative group velocity,

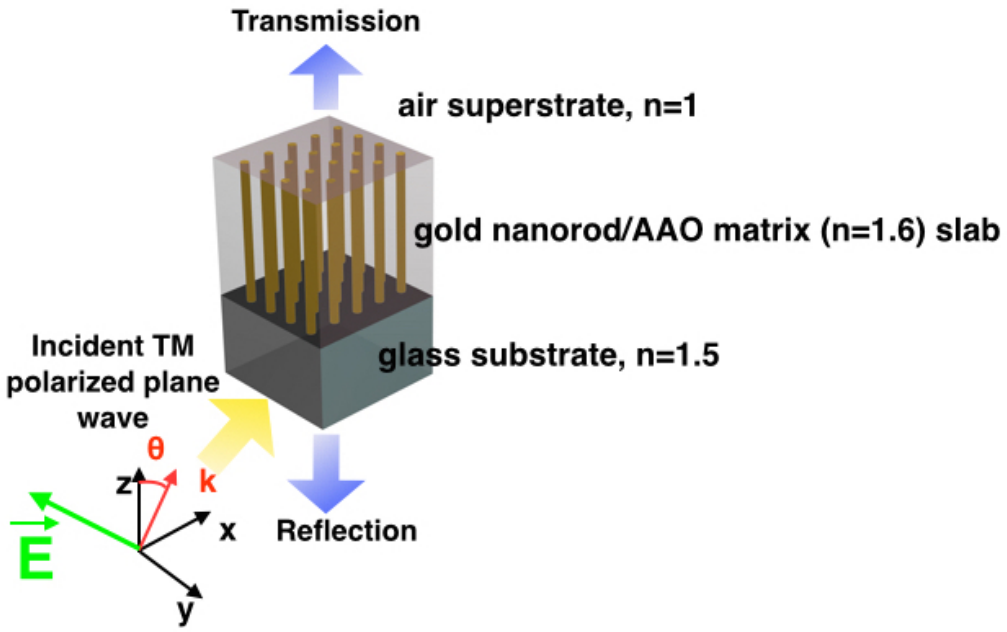

FIGURE 6.1: Schematic of the nanorod metamaterial examined and of the illumination conditions. The incident plane wave is TM polarized with respect to the glass substrate/metamaterial slab interface as explained in 2.2.2.

and thus are associated with the hyperbolic waveguide modes described in section 2.2.3. The fact that waveguide modes with negative group velocity can exsist in the hyperbolic regime, i. e. for negative $\epsilon_{||}$ and so for frequencies below ENZ, has been explained in the context of the Effective Medium Treatment (EMT) with Equations 2.24 and 2.25. It is important to note that the modes are truly guided only below the light line in glass, and are always accessible experimentally via the glass substrate, thus leaky in it. The hyperbolic dispersion obtained with the numerical calculations clearly cannot be recovered by a standard or local EMT, like the one considered up to now. In fact, both the high dispersivity of the L-mode and the structure of the hyperbolic dispersion are a signature of nonlocality. The choice of a nonlocal geometry is motivated by previously observed experimental results on nonlocal nanorod metamaterials [87].

The rich linear modal response of the nanorod/AAO metamaterial, including the anomalous hyperbolic dispersion, is not substantially changed when considering the presence of the thin gold layer deposited above the glass substrate and used for the growth of the nanorods. This layer acts as a highly reflective boundary

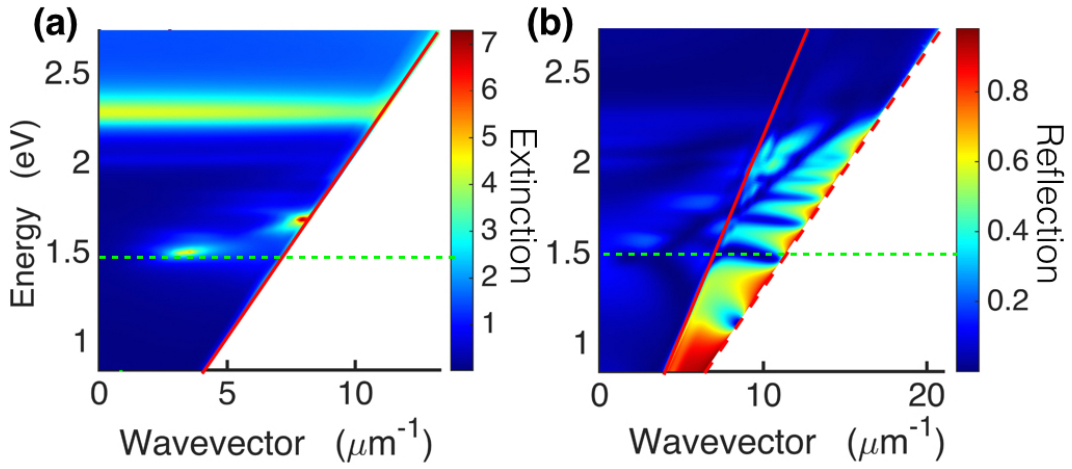

FIGURE 6.2: Linear dispersion of the nanorod metamaterial calculated numerically. (a) is the dispersion of the metamaterial's extinction, (b) is the dispersion of the metamaterial observed through its optical reflection, illuminated by a TM polarized plane wave. The red solid line is the light line in air, while the dashed red line is the light line in glass. The geometrical parameters used are 350 nm for the length, 30 nm for the diameter and 90 nm for the center-to-center distance between the nanorods. The dashed green line corresponds to the ENZ frequency at 1.5 eV, calculated with the local EMT outlined in section 2.2.2.

though, and as a consequence some of the features observed in the optical reflection are enhanced, especially cavity modes, including waveguide modes, forming in the metamaterial as a result of multiple reflections at the metamaterial's interfaces [35]. Figure 6.3 shows the reflection dispersion of the metamaterial, considering an additional 10 nm thick gold layer between the glass substrate and the nanorod/AAO slab. (a) is the numerical calculation, while (b) is the analytical one, using the local EMT. Hyperbolic and elliptic modes are visible, respectively below and above the local ENZ frequency in both calculations.

Figure 6.4 shows the dispersion of the propagation constant of the waveguide modes computed with Equation 2.24, superimposed to the EMT reflection dispersion. The modes with index q=2, 3 and 4 can be identified, while higher order modes are too lossy to be present in the dispersion. The TM mode with q=2 can be identified in both dispersions at a high frequency cutoff of 1.4 eV, but the numerical calculation of Figure 6.3 (a) accounts also for the additional hyperbolic modes above the local ENZ frequency, which originate from nonlocal effects.

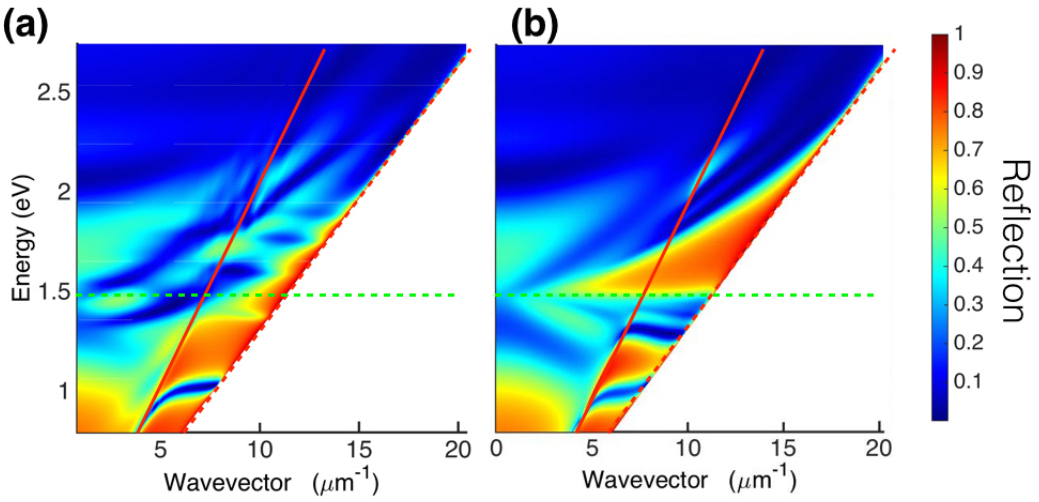

FIGURE 6.3: (a) shows the numerical calculation of the reflection dispersion of the metamaterial considering a thin gold layer above the glass substrate and (b) shows the corresponding analytical calculation obtained using the local EMT. The solid red line is the light line in air, while the dashed red line is the light line in glass. The geometrical parameters used are 350 nm for the length, 30 nm for the diameter and 90 nm for the center-to-center distance between the nanorods. The gold layer has a thickness of 10 nm. The dashed green line indicates the ENZ frequency, which has a value of 1.5 eV, calculated with the EMT outlined section 2.2.2.

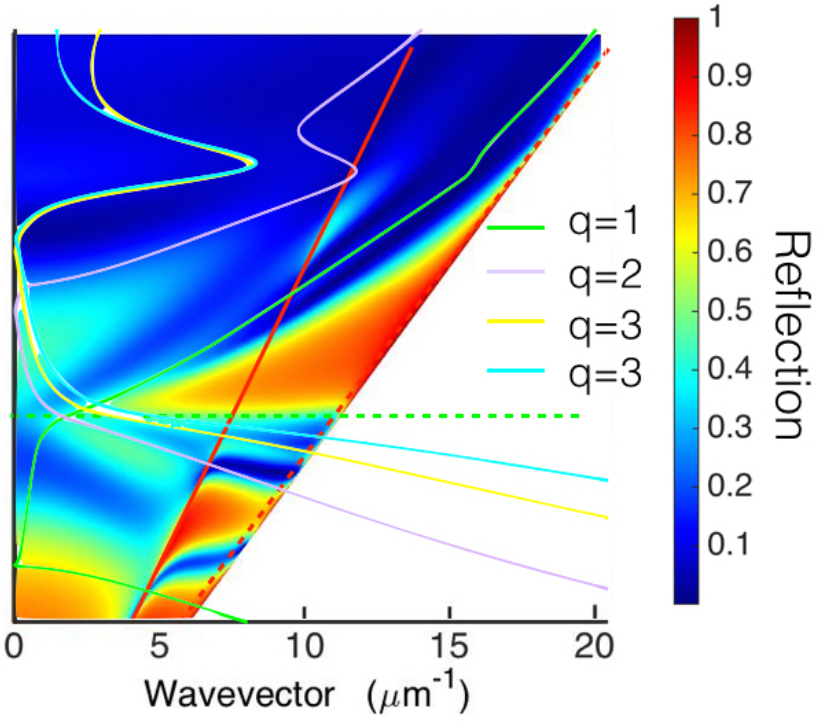

FIGURE 6.4: Reflection dispersion of the nanorod metamaterial computed with the local EMT, considering the presence of a 10 nm gold underlayer. Superimposed are the dispersion relations of the propagation constants of the first four waveguide modes calculated with Equation 2.24.

The homogeneization technique described in section 2.2.2 is based on the assumption that local dispersive constitutive relations, i. e. momentum-independent permittivity and permeability tensors, well describe the response of the composite material to an applied electromagnetic field.

Figure 6.5 shows the effective parameters obtained with the homogeneization technique explained in section 2.2.2. The real part of the effective permittvity component $\epsilon_{||}$ has value zero at a wavelength of 832 nm, corresponding to a frequency of 1.5 eV. Thus the hyperbolic, negative group velocity waveguide modes should be found only for frequencies below 1.5 eV, which is not the case in the dispersion of Figure 6.2 (b).

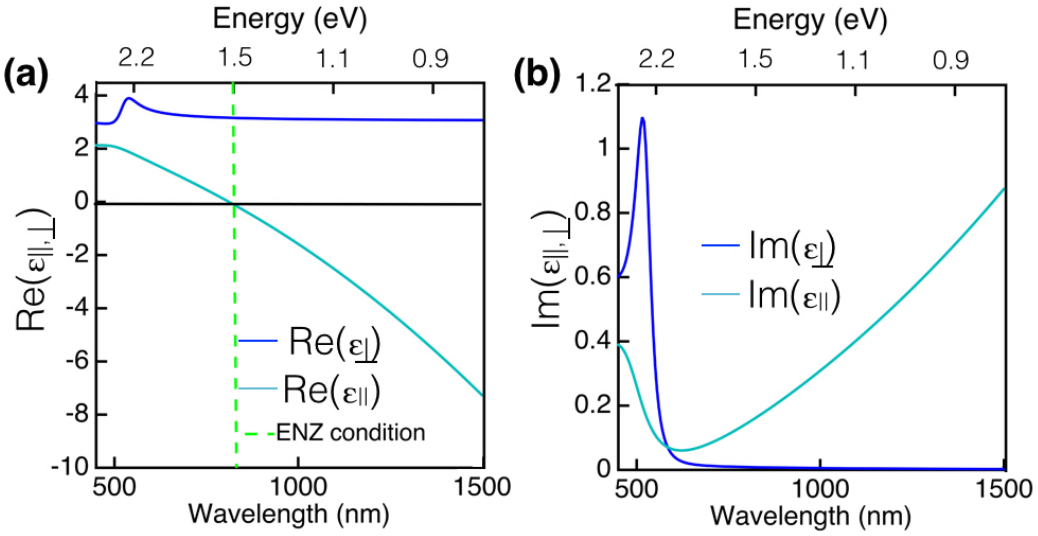

FIGURE 6.5: Real (c) and imaginary (b) part of the diagonal components of the effective dielectric permittivity tensor of the gold nanorod metamaterial. $\epsilon_{\perp}$ is the component of the dielectric permittivity tensor along the directions perpendicular to the nanorod axis, while $\epsilon_{||}$ is the component along the direction parallel to the nanorod axis. The geometrical parameters used are 350 nm for the length, 30 nm for the diameter and 90 nm for the center-to-center distance between the nanorods. The ENZ condition is reached at a wavelength of 832 nm, calculated with the local EMT outlined in section 2.2.2.

The effective parameters of Figure 6.5 provide an adequate description of the metamaterial as long as the variations of the electromagnetic field happen on a scale which is significantly larger that the characteristic size of the individual features. When strong variations of the field happen on the scale of the metamaterial structural components, its spatial derivatives have to be considered as well. In the

case of a plane wave, this means that the constitutive relations will depend also on the components of the wavevector $\vec{k}$ such as $\epsilon(\omega, \vec{k}) = \epsilon(\omega) + \delta(\vec{k})$. Even when the spatial dispersion is a small correction compared to the frequency-dependent term, it becomes predominant when the frequency dependent component of the effective permittivity vanishes.

As can be seen in Figure 6.5, the real part of the dielectric permittivity $\epsilon_{||}$ is close to zero in the region between 750 nm and 840 nm, thus the nonlocal term is expected to become significant in this spectral range, under the condition that the imaginary part of the effective permittivity component $\epsilon_{||}$ also becomes vanishingly small [55, 57, 58]. Figure 6.6 shows the linear extinction spectrum of the metamaterial for various angles of incidence of the incident TM wave. The L-mode undergoes a splitting for an angle of incidence of 30^o. The origin of this splitting can be explained as arising from the strong coupling between the main TM wave sustained by the metamaterial and a second TM polarized wave supported in the nonlocal regime [55].

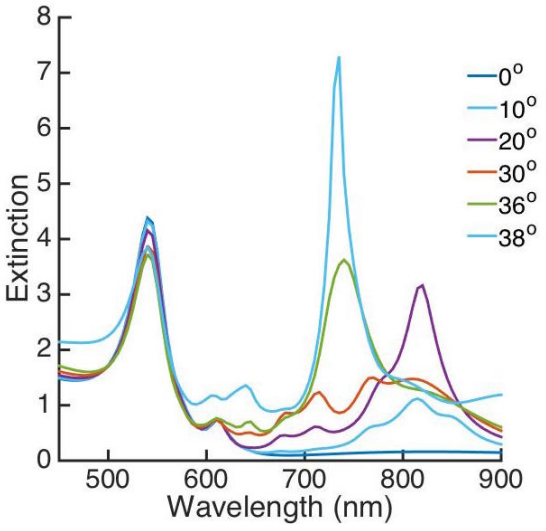

FIGURE 6.6: Extinction spectra of the nanorod metamaterial for different angles of incidence of a TM polarized plane wave. It is possible to observe the nonlocal, high angular dependence of the position of the L-mode around 750-830 nm.

The hyperbolic modes above the local ENZ frequency can be identified with an analytical, effective medium calculation that includes nonlocal effects. Figure 6.7 shows the analytical calculation of the extinction and reflection nonlocal dispersions, which show a remarkable agreement with the numerical results. The

modes identified and that will be investigated with the pump-probe simulation are waveguide TM modes, where the numbers 1, 2, 3, 4 correspond to the number of minima of the electric field profile in the metamaterial slab, visible in Figure 6.10.

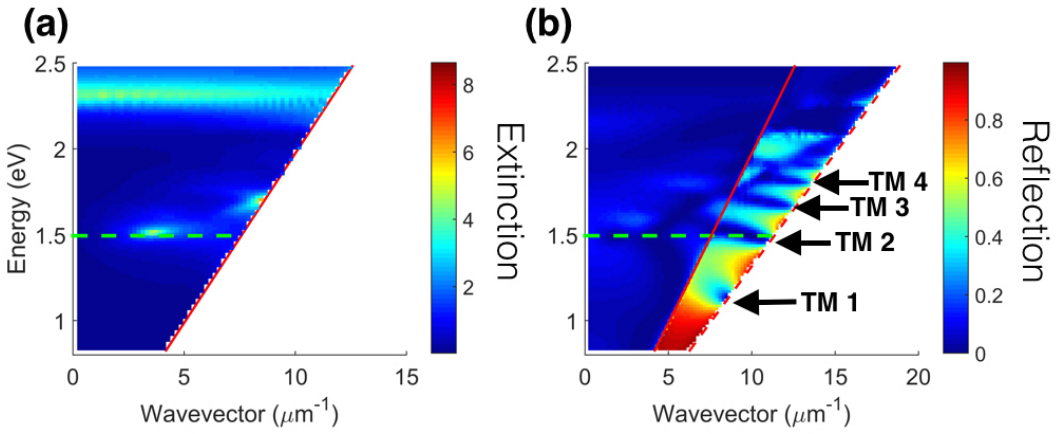

FIGURE 6.7: (a) is the extinction and (b) is the reflection dispersion of the metamaterial calculated analytically including the nonlocal correction to the effective permittivity as in [58]. The red solid line is the light line in air, while the dashed red line is the light line in glass. The geometrical parameters are the same used in the previous calculations. The dashed green line corresponds to the local ENZ frequency at 1.5 eV.

The losses in the metal are the main driving force controlling the nonlocal behavior of the system. In the limit of high losses, corresponding typically to a restriction of the electrons mean free path smaller than 15 nm, and $Im(\epsilon(\omega(Re(\epsilon) = 0)) > 0.1$, the local contribution to the permittivity dominates. Then, the L-mode becomes dispersionless, with only the amplitude and linewidth changing with the incident wavevector. Such a metamaterial can be adequately described by a local EMT.

Losses can be tuned in our system by introducing a restricted mean free path R for the motion of electrons in the gold. In fact, nanorods obtained through electrochemical means have poorer gold quality, with limited electron motion. The typical mean free path of electrons in electrochemically deposited nanorods is generally 3 nm [55], compared to a mean free path in bulk gold R_b of 37.5 nm [55]. The smaller the mean free path, the higher the losses.

In the context of our derivation of gold's dielectric pemittivity with inter and intraband contributions, the mean free path has been kept as a free parameter to fit experimental data for the permittivity of gold, taken from [28]. As a result of this fitting, our linear dielectric permittivity has a restriction on the electrons mean free path of 30 nm. This is the restriction used to compute the optical properties in Figure 6.2. In our model, local effects start to be dominant for typical R values of the order of 15 nm or less. The restricted mean free path is introduced through

$$\epsilon_{correction} = i\omega_p^2 \frac{\frac{R_b - R}{\gamma_{intra}}}{\omega(\frac{\omega}{\gamma_{intra}} + i)(\frac{\omega}{\gamma_{intra}} R + iR_b)}) \tag{6.1}$$

and the complete dielectric permittivity of the gold used is $\epsilon_{gold} = \epsilon_{intra} + \epsilon_{inter} + \epsilon_{correction}$.

Thermally annealing the metamaterial allows to increase the average size of the crystallites composing the nanorods. This results in a decrease in the electron collision rate, and so an increase of the electrons mean free path, to values enabling nonlocal effects to be directly observable in the extinction of the metamaterial as a splitting in the L-resonance, as the one that can be clearly observed in Figure 6.6 for an angle of incidence of 30 ^{o}.

Hence, the mean free path can be used to tune the losses in the metal, enabling to observe the transition of the metamaterial from a nonlocal to a local regime. Spatial dispersion will also be affected by losses in the system, which influence the transition from the local to the nonlocal regime. In the Effective Medium Approach, disorder is not present, since the material is considered to be homogeneous over the wavelength scale sizes. Changing the interrod distance in the Effective Medium theory can, in principle, effectively modify the interaction between the nanorods and can reproduce the introduction of disorder over the larger than wavelength scales. In the numerical simulation, the system is considered to be perfectly periodic, so there is no disorder considered. The electron mean free path can thus be considered as the main cause of losses, and when fitting experimental measurements, the nominal geometrical parameters will also be tuned to recover the existing disorder in the real sample.

Figure 6.8 shows the numerical and analytical calculation ((a) and (b), respectively) of the metamaterial extinction dispersion in the high losses limit. The L-mode doesn't show anymore a complex evolution with the angle of incidence variation, its amplitude is different but not its spectral position. Similarly, the negative group velocity modes that could be observed in the reflection dispersion do not appear above the local ENZ frequency anymore. The local response computed numerically agrees very well with the one computed analytically, as can be seen in Figure 6.8 for the optical extinction of the system and in Figure 6.9 for the optical reflection of the system.

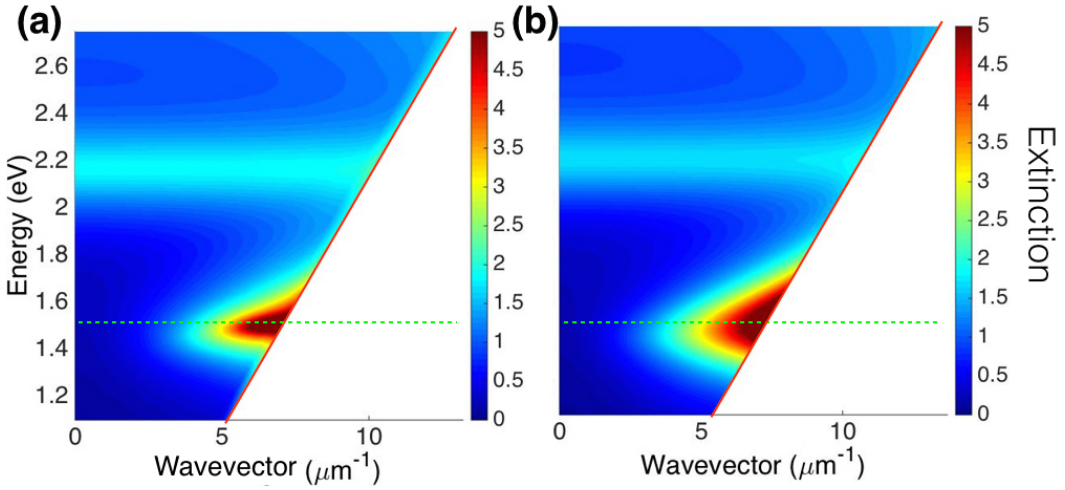

FIGURE 6.8: (a) is the numerical calculation of the disperison observed through the optical extinction of the metamaterial, illuminated with a TM polarized plane wave. (b) is the extinction dispersion of the metamaterial illuminated with a TM polarized plane wave, calculated with EMT. The solid red line is the light line in air. The green dashed line indicates the local ENZ frequency, which has a value of 1.46 eV in this high losses limit. The restricted mean free path of electrons is of 15 nm.

6.2 Nonlinear response of the nanorod metamaterial

The nonlinear response of the system has been investigated by simulating a pump-probe experiment, as explained in section 3.2. In the elliptic regime, we have pumped the system off metamaterial resonance, at 465 nm, which is the

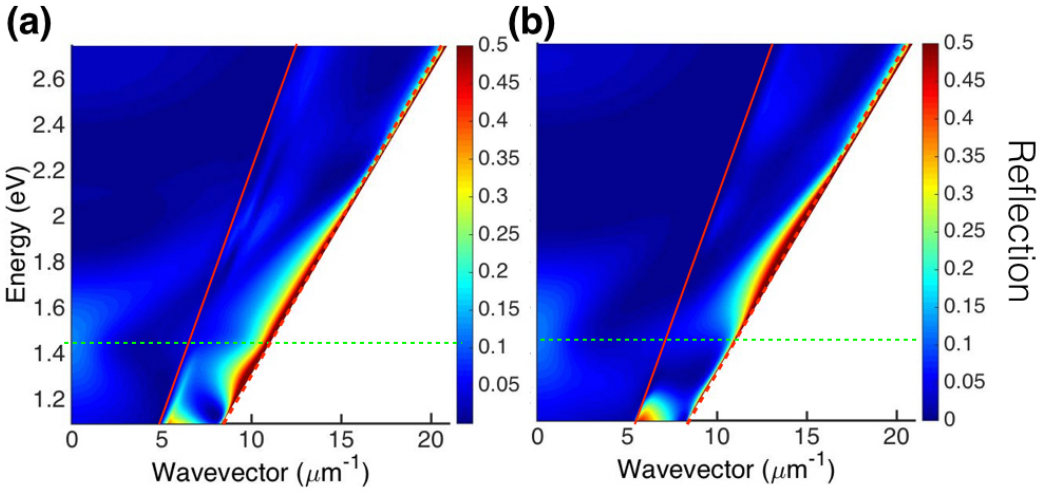

FIGURE 6.9: (a) is the numerical calculation of the disperison observed through the optical reflection of the metamaterial, illuminated with a TM polarized plane wave. (b) is the reflection dispersion of the metamaterial illuminated with a TM polarized plane wave, calculated with EMT. The solid red line is the light line in air, while the dashed red line is the light line in glass. The green dashed line indicates the ENZ frequency, which has a value of 1.46 eV in this high losses limit. The restricted mean free path of electrons is of 15 nm.

region of strong interband absorption. We have used two angles of incidence, 0^o and 20^o, the latter being used for comparison with resonant excitations later on. In the proximity of the local ENZ, we have pumped the system on resonance, at 820 nm and 20^o incidence, corresponding to the L-mode resonance, and again off resonance, at 820 nm and 0^o incidence. We have also pumped the hyperbolic modes above and below the local ENZ frequency, at 670 nm, 730 nm, 830 nm and 1085 nm, in all four cases with an angle of incidence of 60^o. We have used the same fluence of the control gaussian beam for all the configurations, equal to 0.1 mJ/cm^2. This fluence is obtained measuring the integral of the gaussian beam power,

$$P(t) = P_0 e^{\frac{-(t-t_0)^2}{\sigma^2}} \tag{6.2}$$

in one pulse, where P_0 is 0.1 W, t_0 is 100 fs and σ is 50 fs, and divided by the area of the square base of the unit cell.

This fluence is of the order of the smallest fluence used in the ultrafast modulation experiment reported in [87], which is 0.7 mJ/cm^2. The repetition rate of the laser in that case is 1 kHz. As will be shown in the following Sections, the

modulation obtained in the simulations is significantly more efficient than that obtained in the experiment, since the coupling efficiency of the pump with the metamterial's modes is optimized in the simulation. In fact, in the experiment, the energy of the pump is spread among more that one wavevector due to the slight focusing of the beam, which affects strongly the coupling of the energy to a specific mode of the metamaterial. In addition to this, the experimental nanorod samples present noticeable structural inhomogeneities, which again can degrade the coupling efficiency of the pump with the metamaterial modes. The coupling and, as a consequence, the experimental modulation, are averaged over a wide sample area, which will naturally result in a smaller measured transient transmission and reflection with respect to the simulated one. Moreover, nonlocal effects are extremely sensitive to structural imperfections. In this study (apart from section 6.2.4 where the simulations will be directly compared with experimental results) the geometrical parameters are different with respect to the nominal ones used in the experimental studies in [87], and thus cannot be compared directly. Figure 6.10 shows the linear extinction spectra with an angle of incidence of 0^o in (a) and 20^o in (c), and the linear reflection spectra, with an angle of incidence of 60^o in (b) and (d). The reflection of the system, R, is the ratio between the flux of the electromagnetic field reflected by the system, normalized to the incident flux. For the conservation of energy, the absorption of the system is equal to 1- T - R. These fluxes are measured using S-parameters in Comsol [56]. The green lines indicate the wavelengths at which the system has been pumped. For each pump configuration, the electric field norm profile at the central pump wavelength and the electrons temperature distribution inside the nanorods are shown, considering a time delay of 50 fs after the pump excitation.

Figure 6.10 shows a clear mapping between the electric field norm distribution and the electrons temperature distribution in the gold nanorods. The field profile at the wavelength and angle of incidence of the pump is shaping the absorption profile, and as a consequence the temperature profile inside the nanorods. The observable of interest is the modulation of the optical properties of the metamaterial (OP), as a function of time, which will be rationalized against the calculated

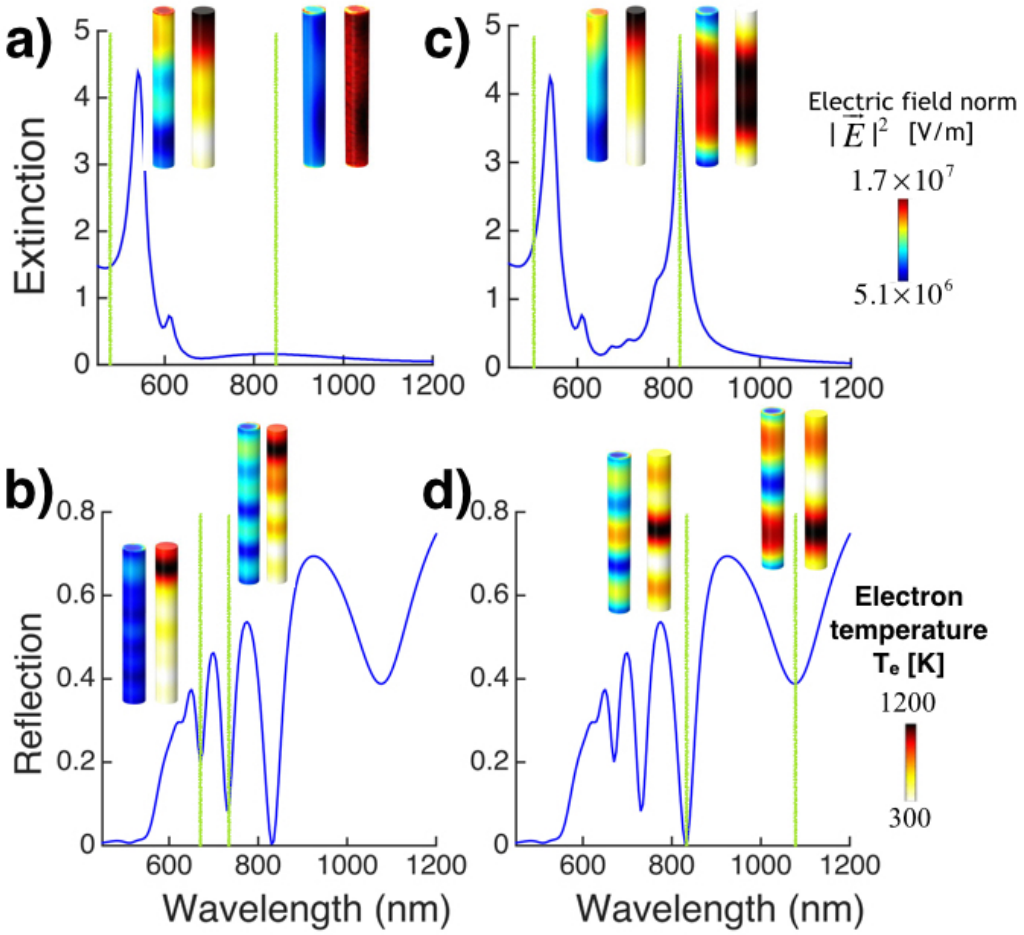

FIGURE 6.10: (a) and (c) show the linear extinction spectra of the metamaterial illuminated by TM polarized light at normal and 20^o incidence, respectively. The green lines indicate the wavelengths at which the system has been pumped, 465 nm and 820 nm, for the specific angle of incidence.(b) and (d) show the linear reflection spectra of the metamaterial illuminated by TM polarized light at 60^o incidence. The green lines indicate the wavelengths at which the system has been pumped, 670 nm, 730 nm, 830 nm, 1085 nm, for the specific angle of incidence. The insets are the electric field norm profile and the electrons temperature profile at a time delay of 50 fs after the pump excitation, for each pump configuration.

electron temperature, as well as the divergence of the gradient of the temperature, which to a large extent can be designed to shape the ultrafast nonlinear porperties of nanostructured systems. Different pump and probe beam configurations will determine a modulation with a characteristic amplitude and recovery time. By exploring the rich modal structure of the system to mediate and probe the nonlinear optical response, the aim is to gain an understanding of the different parameters relevant in optimizing the efficiency of the modulation.

The dynamic of the modulation of the OP of the system, extinction or reflection as of interest here, can be expressed as

$$\frac{d\Delta OP}{dt} = \frac{\partial \Delta OP}{\partial \epsilon} \frac{\partial \epsilon}{\partial T_e} \frac{\partial T_e}{\partial t} \tag{6.3}$$

where ϵ is the dielectric permittivity of gold and T_e is the gold electrons temperature, having assumed that the source of the nonlinearity is the metallic component of the metamaterial, as explained in section 3.2. We will initially focus on the dynamic behavior of the term $\frac{\partial T_e}{\partial t}$, which can be extracted from the TTM.

6.2.1 Electrons temperature dynamics

The dynamics of the electrons temperature averaged over the nanorod volume for the various pump configurations described in the previous section, extracted from the numerical calculations, are shown in Figure 6.11.

As explained in Chapter 3, the electrons temperature dynamic is monitored through the TTM. The power dissipation density of the electromagnetic field of the pump is measured, and it is used as the heat source in the first of the TTM equations 2.55. This equation is then used to find the value of the temperature as a function of spatial coordinates in the nanorods after a 50 fs timestep. The temperature distribution is mapped into the dielectric permittivity distribution via equations 2.50 and 2.53. The power dissipation density is then measured with the updated dielectric permittivity.

Since the fluence used is the same for all the pump central wavelengths and angles of incidence considered, the difference between the maximum temperatures

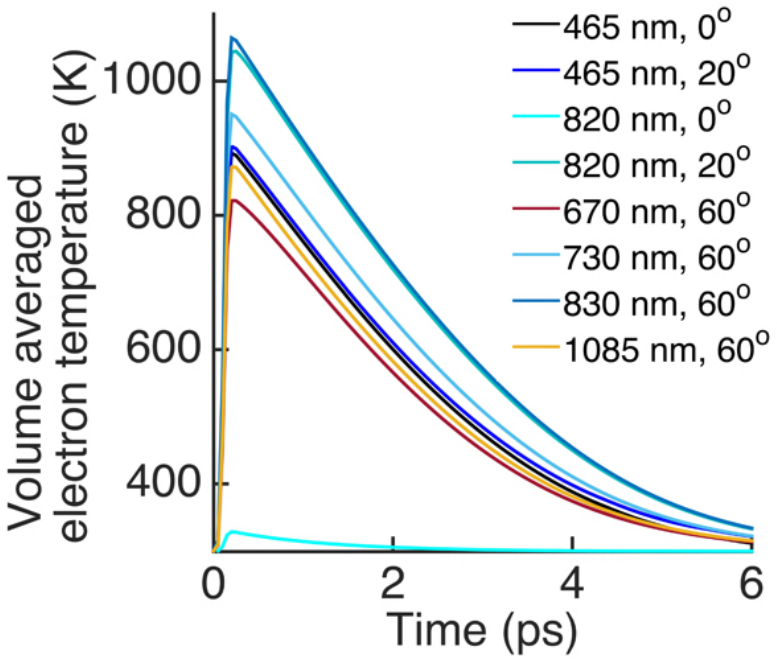

FIGURE 6.11: Time dependence of the electrons temperature averaged over the nanorod volume for the different pump configurations investigated.

reached by the system depends on the different power absorbed by the metamaterial in each pump configuration. The biggest maximum averaged temperature, 1064 K, is reached for a pump pulse centered at 830 nm and at 60^o incidence. These dynamics are fully reproduced, both in terms of the maximum value obtained and in terms of the relaxation dynamics, by solving numerically Equation 2.55, in the absence of the divergence term, and considering as the source term the volume averaged dissipation density, extracted from the numerical pump-probe model.

Figure 6.12 shows the comparison between the numerical calculation of the volume averaged electrons temperature for a representative pump centered at 820 nm and at 20^o incidence, performed on the complete nanostructure domain and in the presence of the divergence term (solid line), and the numerical solution of Equation 2.55, without the presence of the divergence term (dashed line). The two dynamics are very well superimposed, and the same agreement is found for the other pump configurations.

Once established that the volume averaged temperature dynamic is not affected by the presence of the divergence term in Equation 2.55, we can estimate

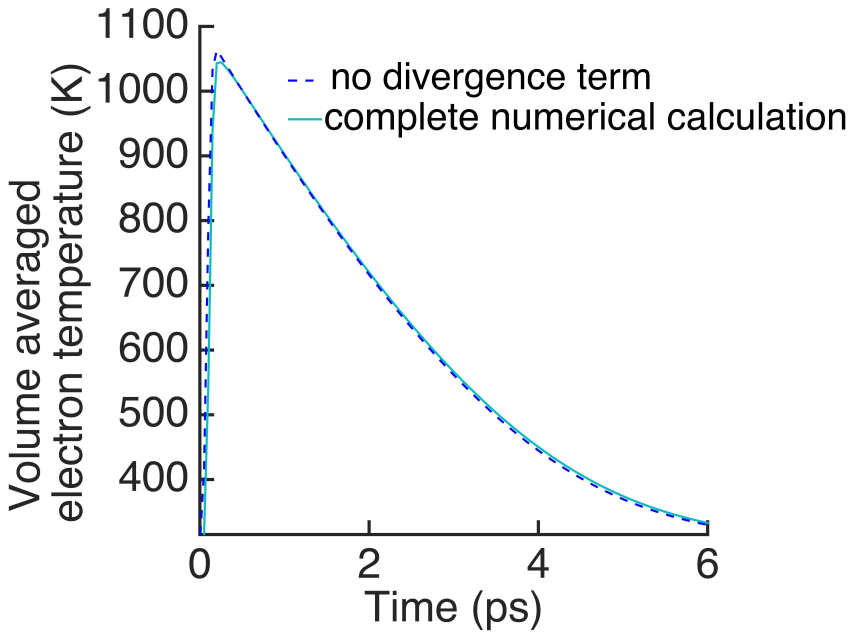

FIGURE 6.12: The dashed line is the electron temperature dynamic computed from Equation 2.55, without considering the divergence term and with the source term extracted from the full numerical calculation as the volume average of the power dissipation density. The solid line is the volume averaged electrons temperature dynamic computed with the full pump-probe model, that icludes the divergence term. The pump used has a central wavelength of 820 nm and an angle of incidence of 20^o.

the value of $\frac{\partial T_e}{\partial t}$, which in this case, since there is no spatial dependence of T, is equal to the total derivative dT_E/dt. We assume that also the optical pump is not active.

When the space and time-dependent divergence term vanishes, the rate equation can be easily solved analytically. Considering the heat capacity of electrons to be independent of their temperature, the temperature dynamic follows an exponential decay for $T_e(t)$, with characteristic time constant C_e/G on the order of 1 ps. This is shown in Figure 6.13 (a). A more realistic situation for gold accounts for a temperature-dependent electron heat capacity of the form $C_e=\gamma T_e$. In this scenario, the absolute value of the rate of change of the temperature is smaller, decreasing with increasing values of γ as shown in Figure 6.13. The respective solutions for these differential equations clearly show the temperature dependence of the relaxation rate, leading to a slowing down of the relaxation time in the situation described by Equation 6.4.

When the heat capacity of electrons depends on the temperature as $C_e = \gamma T_e$,

the absolute value of the rate of change of the temperature is bigger for a higher temperature

$$\frac{dT_e}{dt} = -\frac{G(T_e - T_L)}{\gamma T_e} \tag{6.4}$$

It is important to note that the fact that a faster dynamic is found with a higher temperature in this case doesn't mean that the temperature dependent heat capacity will determine a rate of change of the temperature bigger than that of a constant heat capacity. The relaxation time depends as well on the temperature.

$$t = -ln((T_e - T_L)e^{\frac{T_e}{T_L}}e^{-\frac{A}{T_L}})\frac{\gamma T_e}{G} \tag{6.5}$$

where A is

$$A = T_L(ln(T_e(t=0) - T_L) + \frac{T_e(t=0)}{T_L}) \tag{6.6}$$

The two scenarios are compared in Figure 6.13, for an initial temperature of 1043 K, corresponding to the maximum volume average temperature with a pump centered at 820 nm and at 20^o incidence. The temperature dynamic with a temperature dependent heat capacity follows a multiexponential decay.

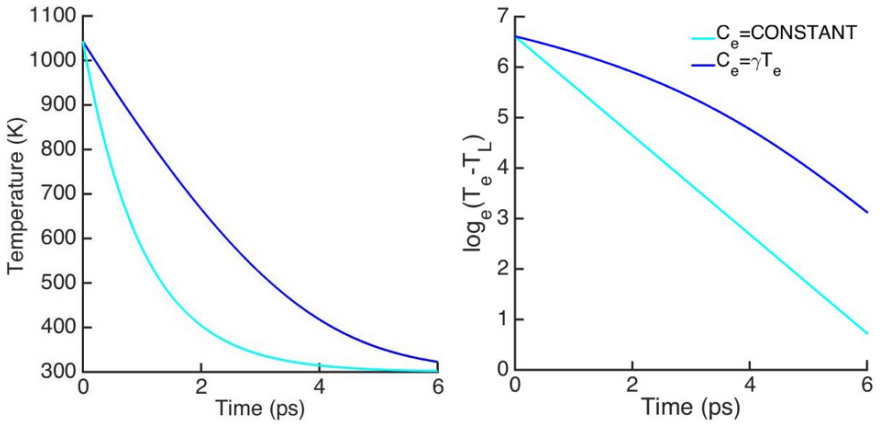

FIGURE 6.13: Comparison between the electron temperature dynamic computed from Equation 2.55, without considering the divergence term and the source term, for two different values of the heat capacity. The light blue line considers a temperature independent heat capacity with a value of 67.69[Kg/m^{3}K^2]*300K, while the dark blue line is obtained considering a temperature dependent heat capacity, with a value of γT_e where γ=67.69[Kg/m^{3}K^2]

Since for gold the heat capacity of electrons depends on the temperature, the presence of inhomogeneities in the temperature distribution inside the nanorods,

clearly visible in Figure 6.10, will determine different rates of change and different temperature dynamics, depending on the spatial coordinates considered.

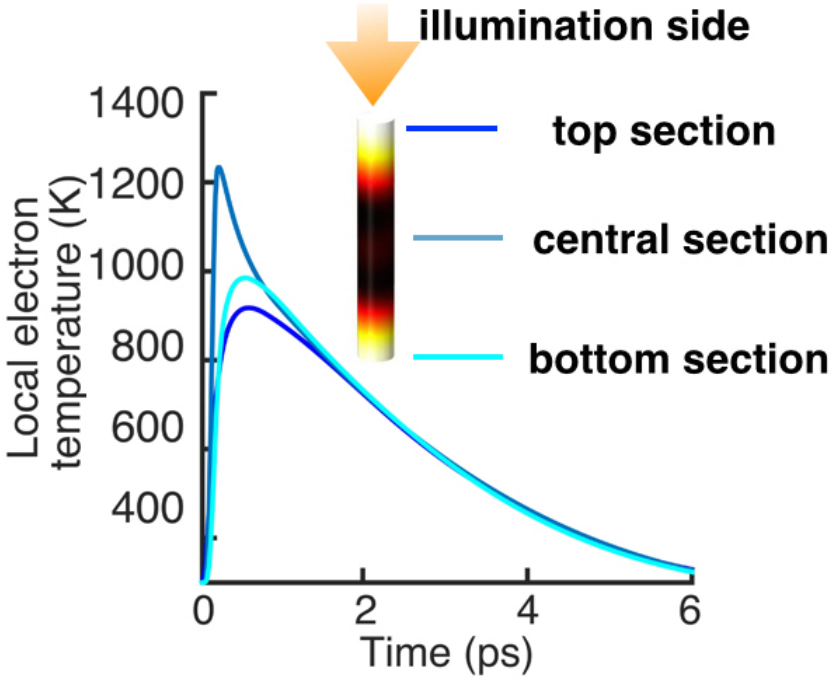

FIGURE 6.14: Electrons temperature dynamics analyzed at different points in the nanorod, for a pump wavelength of 820 nm and angle of incidence of 20^o.

To summarize, the brief analysis of the rate equations governing the energy relaxation of electrons in gold, within the bounds of our accepted model, has lead to two main conclusions.

The first is that the total relaxation time for electrons to dissipate the excess energy deposited by the optical pump in order to return to equilibrium with the lattice energy only depends on the amount of optical power absorbed by the metamaterial from the pump. This is a trivial conclusion following directly from the assumptions made to model relaxation rates in our numerical experiments, but needs to be accepted as we move forward in this Chapter. For plasmonic systems, showing relatively complex position-dependent electron temperature distributions, this time then corresponds to the dynamics of the electron temperature as spatially averaged over the metallic component of the metamaterial (Figure 6.11), a quantity recovered with the TTM, accounting only for a homogeneous electron energy across the metal.

The second is that with the introduction of a temperature dependent electronic heat capacity in the TTM, the relaxation rate, and therefore the associated relaxation time, grows with electronic temperature. These apparently contradictory statements are unified by the introduction of the divergence term in the TTM, adjusting the relaxation rates locally so as to ensure a globally (spatially) unchanged average electronic temperature dynamic. Figure 6.14 shows the time evolution of the electrons temperature at different locations inside the nanorod for a pump central wavelength of 820 nm and angle of incidence of 20^o. In this case it is possible to see that, especially at early times, the dynamic of the electrons temperature shows different beahviors. The warmer locations of the rod relax faster, an effect solely due to the presence of a divergence in the gradient of the temperature. Neglecting this term in the TTM would lead to a longer relaxation time for higher temperatures as shown above.

The opportunities for nanostructured plasmonic systems, as a result of these observations, become evident immediately. Since for gold the heat capacity of electrons depends on the temperature, and the spatial distribution of energy deposited by the pump beam (Figure 6.14) in the metamaterial is a mapping of the modal distribution of the metamaterial at the pumping conditions, including polarization and frequency, we can expect nanostructured systems to show highly spatially-dependent electron energy dynamics. Because the average electron energy relaxation rate is unchanged, some region of space will suffer attenuated or even reversed rates while other spatial regions will experience enhanced rates, driven back to equilibrium much more rapidly, in fact exceeding average rates by several orders of magnitude for the model geometry studied in the work. While the full potential of designing ultrafast dynamics at the nanoscale provides far-reaching opportunities that go beyond the scope of this work, including the ability to regulate energy transfers at the nanoscale between interacting nanostructures for example, here we will make an attempt to rationalize these effects when observed in averaged far-field measurements and further discuss their implications in the use of metamaterials for ultrafast applications.

At the heart of this diagnostic strategy is the resonant behavior of the metamaterial, a direct spatially-sensitive probe of the optical properties in itself, able to sample the spatial inhomogeneities in the electron temperature distribution according to its modal distribution. In a zero-order approximation, this statement can be expressed mathematically as an overlap integral of the form

$$\Delta OP \propto \sum_n \int \Psi_m^*(\vec{r},t) V(\vec{r},t) \Psi_n(\vec{r},t) d\tau \tag{6.7}$$

where the integration runs over all space, $\Psi_i(\vec{r},t)$ represents the metamaterial's eigenmode i, $V(\vec{r},t)\Psi_n(\vec{r},t)$ represents the pump-driven Kerr-induced modification of eigenmode $\Psi_n(\vec{r},t)$, $\Psi_m(\vec{r},t)$ is the eigenmode sampling the nonlinear changes in $\Psi_n(\vec{r},t)$, i.e. the probing mode addressed by the incident field, and the discrete summation runs through all of the metamaterial's eigenmodes, including the probing eigenmode $n = m$. A transient nonlinear dispersion is then obtained by further probing all optically active eigenmodes at different frequencies and in-plane momenta.

6.2.2 Dynamics of the optical modulation

We have considered the different TM polarized probe beam in order to understand which modes had the biggest sensitivity to the nonlinear modulation. We will examine the modulation of the optical extinction(ΔOD) and of the optical reflection (ΔR) such as:

$$\begin{aligned} \Delta OD &= Extinction_{Nonlinear} - Extinction_{Linear} \\ \Delta R &= Reflection_{Nonlinear} - Reflection_{Linear} \end{aligned} \tag{6.8}$$

where the subscript Nonlinear indicates the optical properties of the system probed at a certain time delay after the excitation and the subscript Linear indicates the optical properties of the system in the ground state, at infinite time delay after the ultrafast excitation. Figure 6.15 (a) shows the dispersion of ΔOD at the time delay after the pump excitation where the maximum modulation occurs, τ=200 fs, while (b) shows the dispersion of ΔR in the same condition. The

dispersions allow to locate suitable angles of the probing beam to observe the greatest nonlinear modulation. These dispersions refer to the pump configuration centered at a wavelength of 820 nm, and at an angle of incidence of 20^o, but the same qualitative features are present for all the other pump configurations. I have chosen to examine the dynamic evolution of ΔOD for an angle of incidence of the probe of 20^o, and the dynamic evolution of ΔR for an angle of incidence of the probe of 60^o, indicated by the black solid lines in (a) and (b), respectively.

As expected in the small perturbation approximation, in the condition in which $V(\vec{r},t)\Psi_n(\vec{r},t)$ is approximately equal to $\Psi_n(\vec{r},t)$, the absolute modulation is stronger, so the probing L-mode provides a better overlap integral with the pump-induced modal changes across the spectrum.

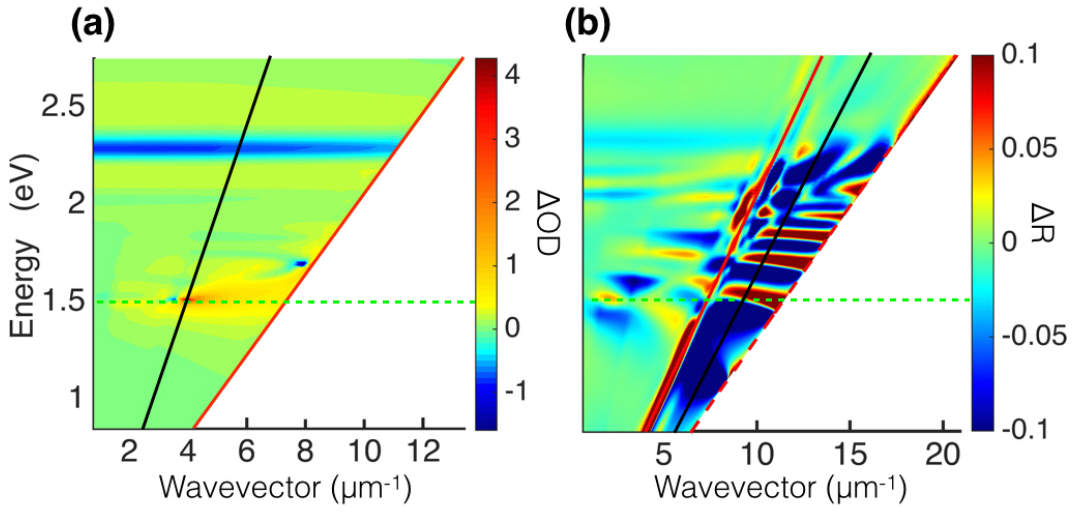

FIGURE 6.15: (a) shows the differential extinction dispersion at the time corresponding to the maximum modulation, τ=200 fs. (b) shows the differential reflection dispersion in the same condition. The solid red line is the light line in air, while the dashed red line is the light line in glass. The dashed green line indicates the local ENZ frequency. The solid black line in (a) shows the 20^o incidence differential extinction. The solid black line in (b) shows the 60^o incidence differential reflection.

Figure 6.16 shows the cross sections of the extinction ((a)) and reflection ((b)) modulation dispersions as a function of wavelength, for various angles of incidence of the probing light. In (a), 20^o shows the maximum modulation, while in (b), 60^o shows the maximum modulation.

Again, we are focusing on the modal response of the metamaterial, neglecting average optical effects occurring at the critical angle for example, which can also

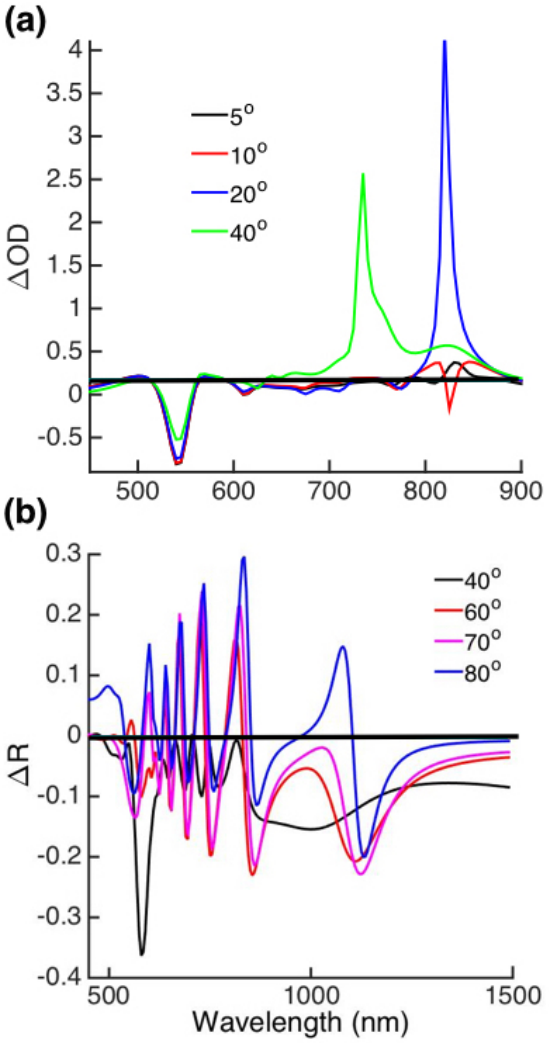

FIGURE 6.16: (a) shows the differential extinction at the time corresponding to the maximum modulation, τ=200 fs, for various angles of incidence of the probing beam. (b) shows the differential reflection dispersion in the same condition. The modulation refers to a pump centered at 820 nm, with an angle of incidence of 20^o.

show substantial changes in reflectance under nonlinear excitation. The dynamics of the OP have been fitted with a linear combination of exponential functions

$$\Delta OP = \sum_{i}^{n} A_i e^{-\frac{t}{\tau_i}} \tag{6.9}$$

The relaxation constants τ_i determined in this way are effective relaxation constants, that allow to make a comparison between the performance of the different pump-probe configurations used, but are not intended to determine physically related dynamic constants.

First of all, I will examine the nonlinear response for a pump pulse in the elliptic regime, centered at 465 nm, in the spectral region of strong interband absorption, but off-resonance with regards to the modes supported by the metamaterial, for two different angles of incidence, of 0^o and 20^o, and probed through the optical extinction at 20^o and through the optical reflection at 60^o.

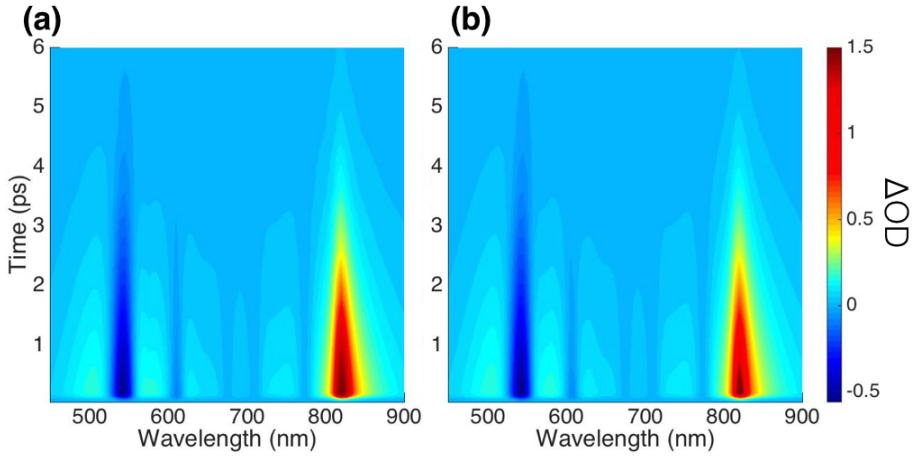

FIGURE 6.17: (a) transient extinction map of the metamaterial pumped at 465 nm, 0^o incidence and (b) at 20^o incidence. In both cases the probing light is TM polarized, at 20^o incidence.

Figure 6.18 shows the cross sections of the dynamic maps corresponding to increasing time delays from the start of the pump excitation. The T and L-mode undergo the main modulation. The transient response of the T-mode can be understood on the microscopic level by a redshifted and broadened excited state, mainly as a result of the increased interband electron scattering. The transient response of the L-mode at this angle of incidence reveals increased extinction, but does not shift spectrally significantly. As a result, the L-mode shows the maximum positive modulation amplitude at 820 nm, 20^o of 1.71. The relative percentage extinction modulation is thus 54%. For the two different angles of incidence for the pump in the elliptic regime, the temperature dynamics, as is shown in Figure 6.11, is indistinguishable. The modulations obtained are also extremely similar, as can be seen in Figure 6.18, reflecting the off-resonance response of the metamaterial, and therefore very similar and featureless field distribution and associated electron temperature distributions for both pumping conditions. This is due to the fact

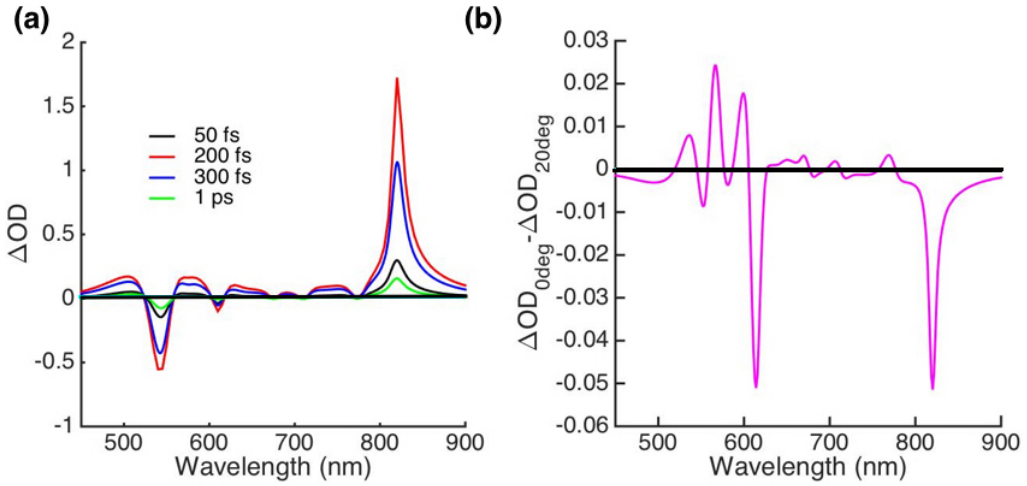

FIGURE 6.18: (a) ΔOD of the metamaterial pumped at 465 nm, 20^o incidence at different time delays from the pump excitation and (b) difference betwee the maximum ΔOD for the pump at 465 nm, 0^o and the maximum ΔOD for the pump ay 465 nm, 20^o incidence. In both cases the probing light is TM polarized, at 20^o incidence.

that the excitation is off resonance, so a different angle of incidence of the pump doesn't change the absorption and temperature spatial profile inside the nanorods.

ΔR, observed at an angle of 60^o, is greatest at a probing wavelength of 860 nm and equal to -0.09. The corresponding relative percentage variation of reflection is 30%. Figure 6.20 shows selected cross sections of the dynamic map for the two angles of incidence of the pump configuration in the elliptic regime, and the probe at 60^o. As for the transient extinction, the transient reflection maps for the two angles of incidence of the pump are also substantially indistinguishable. As previously explained, this is forseeable since the absorption profile is not different for different angles if incidence, being the pumps off resonance.

Figure 6.20 shows the cross section of the dynamic map for the two angles of incidence of the pump configuration in the elliptic regime, and the probe at 60^o. When pumping the system at 820 nm with an incidence angle of 20^o, i.e. in resonance with the L-mode, a noticeable difference from the 0^o incidence configuration is observed. With the pump at normal incidence, in the absence of the L-mode plasmonic resonance, the nonlinear modulation is two orders of magnitude smaller. The optical modulation performances of our system can be considered optimized when combining the pump and probe beams at 820 nm and at 20^o incidence. The

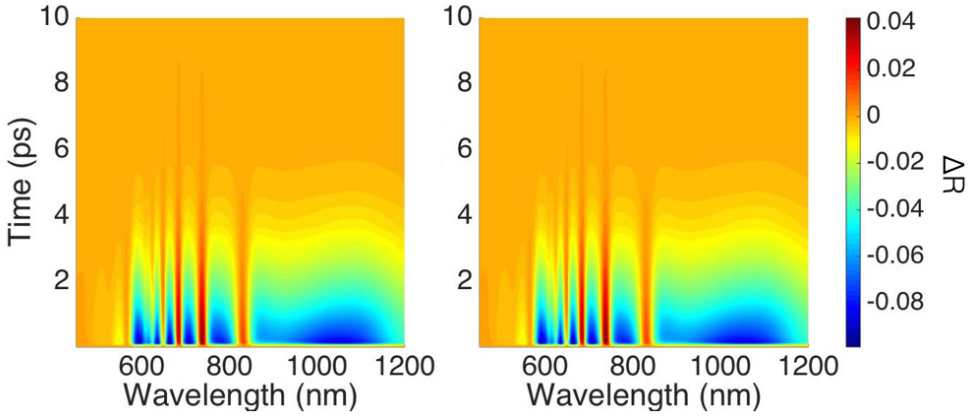

FIGURE 6.19: a) transient reflection map of the metamaterial pumped at 465 nm, 0^o incidence and b) at 20^o incidence. In both cases the probing light is TM polarized, at 60^o incidence.

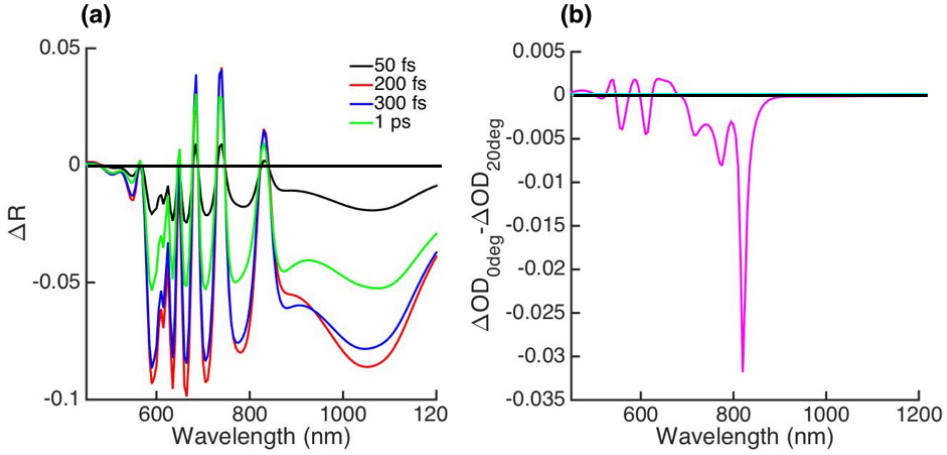

FIGURE 6.20: a) transient reflection map of the metamaterial pumped at 465 nm, 0^o incidence and b) at 20^o incidence. In both cases the probing light is TM polarized, at 60^o incidence.

maximum relative percentage change in extinction exceeds 130%. This is due to the fact that the superposition between the pump-shaped absorption profile and the probe electric field profile are maximized. Figure 6.21 (a) shows the transient extinction map of the metamaterial pumped at 820 nm and normal incidence, while (b) shows the transient extinction of the system pumped at 820 nm and 20^o incidence. Due to the presence of the plasmonic resonance, the absorption in the case of the pump at non normal incidence is enhanced of two orders of magnitude. The maximum value of the power absorbed by a single nanorod at non-normal incidence is 0.0551 W, while for the pump at normal incidence is approximately

0.0005 W. This leads to increased transient optical properties, especially at the L-mode resonance frequency. The remarkable feature is in the relative extinction at the two resonant frequencies of the metamaterial probed in these conditions. While both T and L-modes are sensitive to the off-resonant pumping, the L-mode proves three times more sensitive to the resonant excitation at the L-mode frequency, in accordance with the overlap integral. Again, it needs to be emphasized that the increased absorption of the resonant pump leads to an increased electron temperature compared to the non-resonant excitation. While this enhances the amplitude of the transient optical properties, it also leads to longer relaxation times within our model calculations.

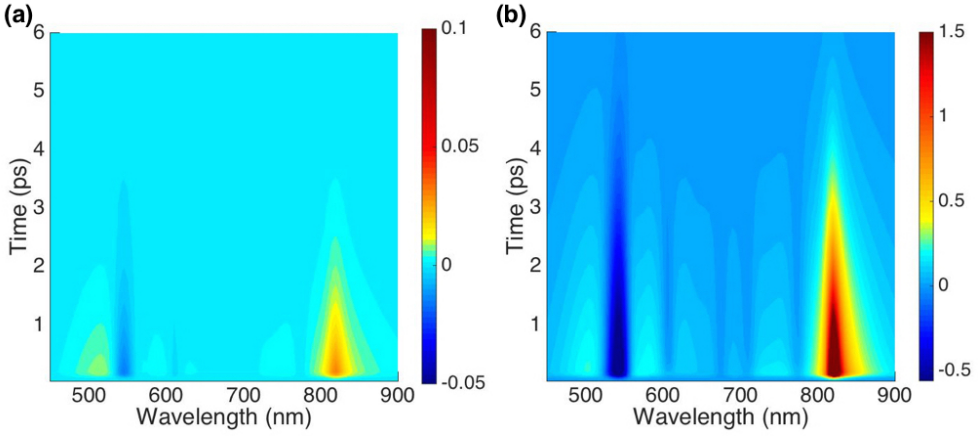

FIGURE 6.21: a) transient extinction map of the metamaterial pumped at 820 nm, 0^o incidence and b) at 20^o incidence. In both cases the probing light is TM polarized, at 20^o incidence.

6.2.3 Role of temperature inhomogeneities in the dynamic of the optical response

In order to understand the role of the divergence term of Equation 2.55 in the strength of the nonlinear modulation, we have compared the amplitude of the nonlinear modulation when the inhomogeneities in the temperature distribution inside the nanorods are considered, with the amplitude of the modulation considering a homogeneous temperature distributon, equal to the correspondent volume average electrons temperature. This has been done for a representative pump pulse centered at 820 nm, with an angle of incidence of 20^o. As can be seen in

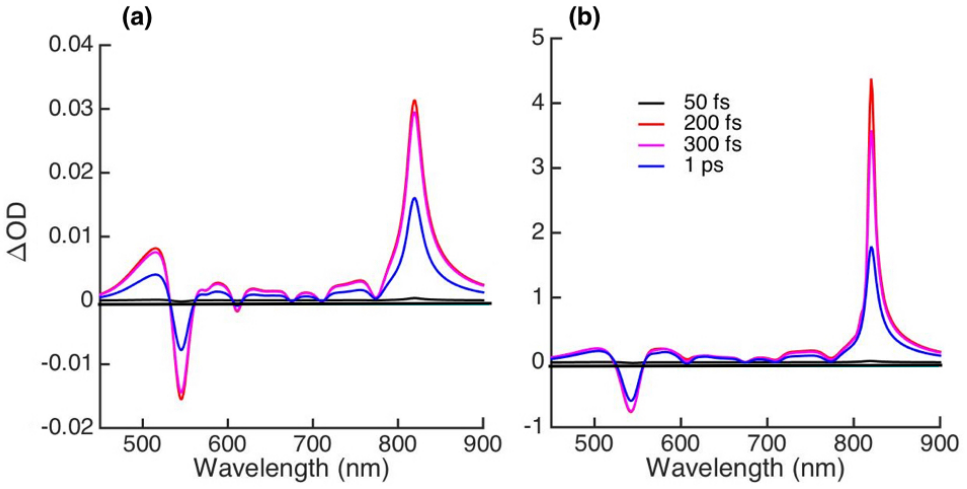

FIGURE 6.22: a) cross section of the transient extinction map of the metamaterial pumped at 820 nm, 0^o incidence and b) at 20^o incidence, for different time delays. In both cases the probing light is TM polarized, at 20^o incidence.

Figure 6.23, the amplitude of the modulation probed at 820 nm, 20^o incidence, is enhanced of 20% when the inhomogeneities in the temperature distribution are considered. The increase of the nonlinear modulation is consistently observed using all the pump configurations considered, mantaining the same probing beam settings. The percentage increase of the modulation varies in the range of 5-10%.

Subsequently, we have compared the dynamics of the optical extinction and reflection of our system when using the inhomogeneous and the homogeneous temperature distribution. Figure 6.24 shows the normalized dynamic of the differential optical extinction of the metamaterial using the inhomogeneous temperature distribution and the correspondent homogeneous values of its volume average. Although this is a qualitative comparison, it is possible to notice how the optical relaxation of the system is faster in the case in which inhomogeneities are considered. The representative pump configuration used in Figure 6.24 has a central wavelength of 830 nm and an angle of incidence of 60^o. The probing wavelength considered is always that of the L-mode, at an angle of incidence of 20^o.

Also this faster optical relaxation is observed consistently across the different pump configurations, keeping the probe beam at 820 nm, 20^o incidence.

The presence of inhomogeneities in the electrons temperature distribution provides thus not only a boost for the nonlinear modulation, but also for the

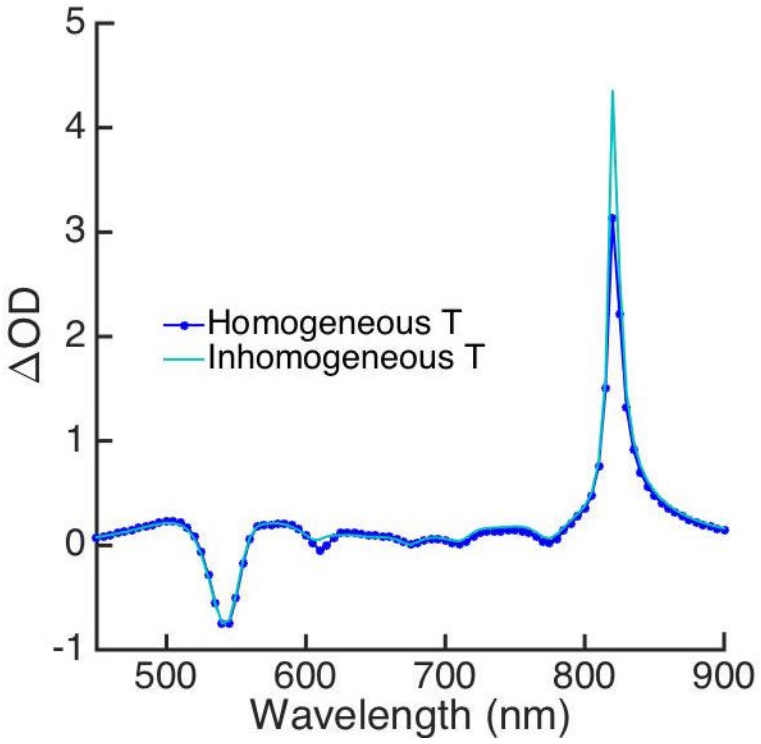

FIGURE 6.23: The dark blue line is the differential optical extinction of the nanorod metamaterial computed considering a homogeneous electron temperature inside the nanorods, equal to the volume average of the electron temperature distribution. The light blue line is the differential optical extinction of the nanorod metamaterial computed considering the inhomogeneous electron temperature distribution in the nanorods. The pump pulse considered is centered at 820 nm and has an alngle of incidence of 20^o, and the probe beam has an angleof incidence of 20^o. The space dependent, inhomogeneous temperature distribution considered corresponds to a time delay of 200 fs after the pump excitation, and the correspondent volume average has a value of 1043 K.

relaxation dynamics.

It is insightful to compare the dynamics of off- and on resonance pumping when identical powers have been deposited by the pump beam in the metamaterial. In particular, I have compared two pumping configurations for an input power such that the integrated power absorbed in both cases is the same. This allows to understand how the different overlap between the pump-induced temperature distribution and the probing beam electric field profile in the two configurations can lead to a different dynamic of ΔOD.

Figure 6.25 shows the maximum power dissipation density absorbed by the system in the presence of the two different pumps, as a function of the maximum input optical power. We have thus chosen the appropriate maximum input power

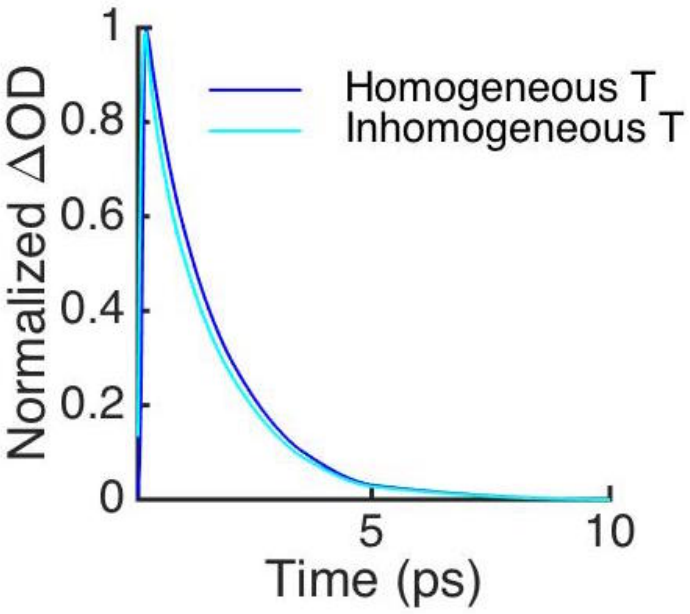

FIGURE 6.24: The dark blue line is the differential optical extinction dynamic of the nanorod metamaterial computed considering a homogeneous electron temperature inside the nanorods, equal to the volume average of the electron temperature distribution. The light blue line is the differential optical extinction of the nanorod metamaterial computed considering the inhomogeneous electron temperature distribution in the nanorods. The pump pulse considered is centered at 830 nm and has an alngle of incidence of 60^o, and the probe beam has a wavelength of 820 nm an angle of incidence of 20^o.

for the two pump configurations in order to obtain a time-integrated power dissipation density of 1.414 J/m^3 in both systems. The resulting maximum input powers are of the order of 10^{-3} W for the pump at normal incidence and of 10^{-4} W for the resonant pump. Figure 6.26 shows the dynamic of the volume averaged electrons temperature for the two pumping conditions, and Figure 6.27 shows the optical extinction probed at the L-mode resonance for both on- and off-resonant pumping situations. The transient change in extinction demonstrates both a stronger amplitude and a bigger relaxation rate when pumping and probing both occur at the L-mode resonance. This is consistent with the overlap interpretation given earlier and with the unchanged average dynamics expected for this system, keeping in mind that the dynamics of the optical properties carries more information than the dynamics of the electron temperature.

The volume average electrons temperature shows the same variation and dynamics in the two systems, which is what is expected having the same energy

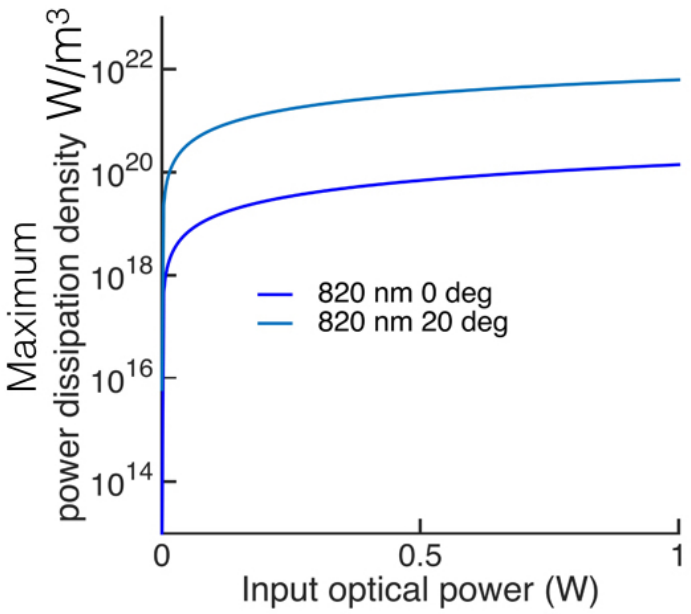

FIGURE 6.25: Maximum power dissipation density inside the nanorods for two different pumps, both centered at 820 nm, one at normal incidence and one at 20^o incidence.

input. On the contrary, the optical differential extinction probed at 820 nm and 20^o incidence, is different between the two configurations. The time decay constants that can be extracted are 1.2 ps for the normal incidence pump and and 0.8 ps for the non-normal incidence pump.

While transient changes in the amplitude of the optical properties and transient dynamics are ultimately intimately related, let us make an attempt to gain further understanding of our observations by an analysis of the pump-induced transient temperature profiles. The optical modulation probed at 820 nm depends on the spatial dendent temperature profile induced by the optical pump. The power dissipation density term (the driving term) in the TTM Equation 2.55 for the two pump configurations is of the order of 10^{-4} after 500 fs. Thus it is negligible compared to the coupling term $G(T_e - T_L)$, which is of the order of 10^{16}, and to the divergence term. Figure 6.28 shows the map of the divergence term in the two pump configurations at 500 fs time delay, extracted from the numerical calculations, in a vertical cross section containing both the plane of incidence and the symmetry axis of the nanorod (the nanorod has its centre in the origin of the

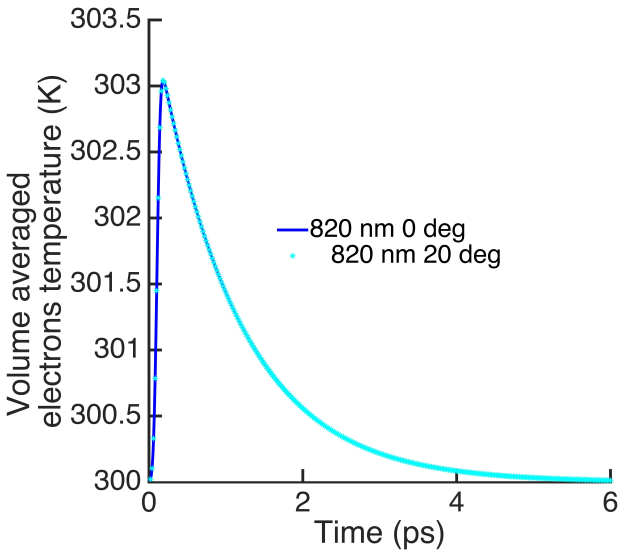

FIGURE 6.26: Volume averaged electron temperature for two different pumps, both centered at 820 nm, one at normal incidence and one at 20^o incidence, considering the same time integrated power dissipation density.

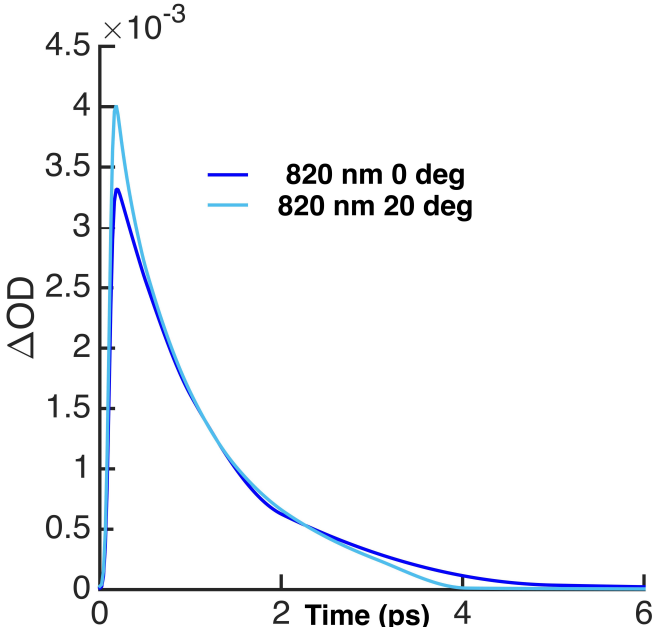

FIGURE 6.27: Dynamic of the differential extinction of the system for two different pump configurations, both centered at 820 nm, one at normal incidence and one at 20^o incidence, considering the same time integrated power dissipation density, probed at 820 nm and 20^o.

reference system).

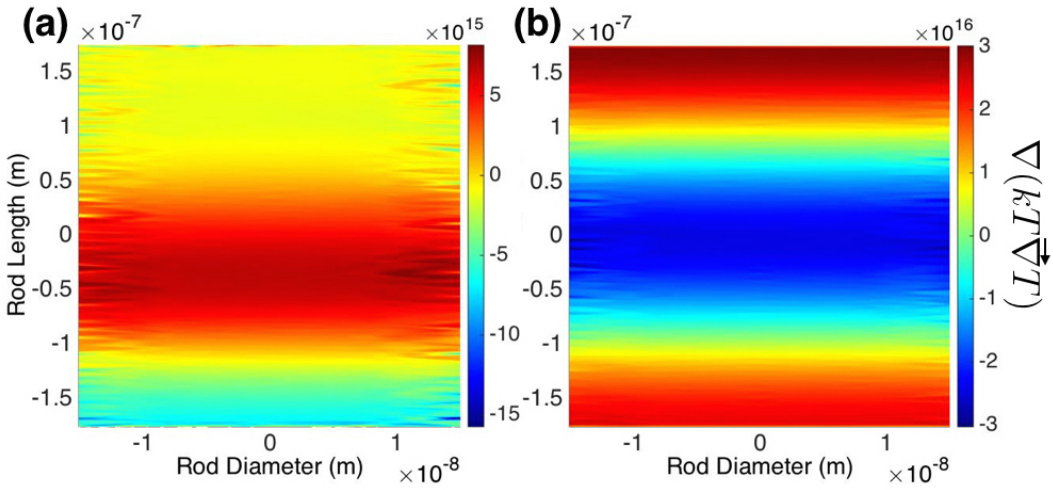

FIGURE 6.28: Divergence term in the TTM plotted as a function of spatial coordinates for 820 nm, 0^o off-resonant (a) and 820 nm, 20^o resonant (b) pump configurations. The same time integrated power dissipation density is considered in both cases.

Following the TTM description it is found that regions of higher negative temperature divergence also demonstrate stronger negative relaxation rates and therefore faster relaxation times. Metamaterial eigenmodes that map these spatial regions will also experience faster pump-induced optical changes, as can be evidenced when probing these modes. It is interesting to note that the topography of the temperature spatial distribution may not overlap the topography of the divergence term in the TTM, although such an overlap is observed in Figure 6.28.

The reflection modulation amplitude also differs of an order of magnitude when considering two angles of incidence for the pump at 820 nm, as can be seen in 6.29.

Finally, we have used a pump beam resonant with selected hyperbolic modes, visible in the reflection dispersion map above and below the local ENZ fequency. Figure 6.30 and Figure 6.31 respectively show the dynamic transient extinction measured at an angle of 20^o and the transient reflection measured at an angle of 60^o for the system pumped at the four hyperbolic resonances, all addressed at an angle of incidence of 60^o. The chosen pumping conditions are at constant incident fluence for all cases. As a result, the absorbed energy varies and the differences in the transient maps do reflect both the differences in the amount of

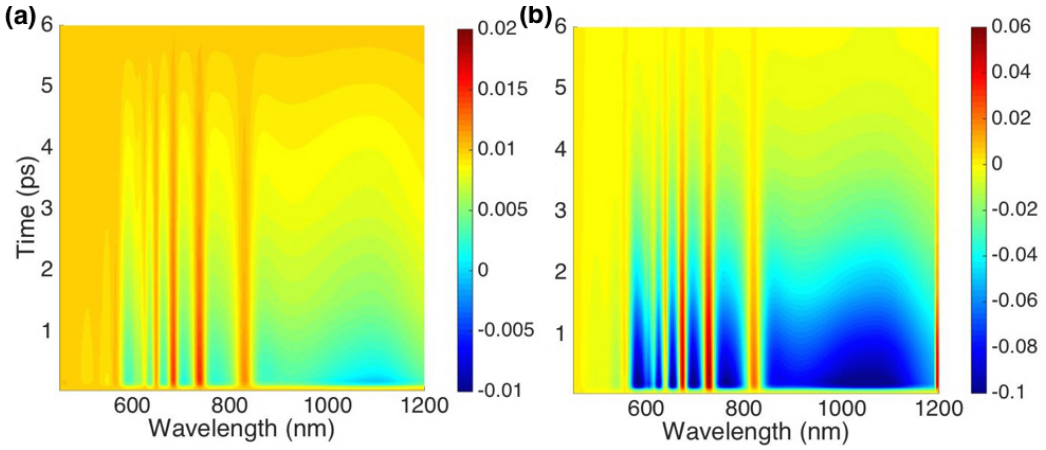

FIGURE 6.29: Dynamic of the differential reflection of the system for two different pump configurations, both centered at 820 nm, one at normal incidence and one at 20^o incidence, probed at an angle of 60^o

power deposited by the pump in the metamaterial, but also the capacity of the metamaterial's modes at mapping the spatial distribution of the deposited power, including the divergence term, as encrypted in the electronic temperature changes.

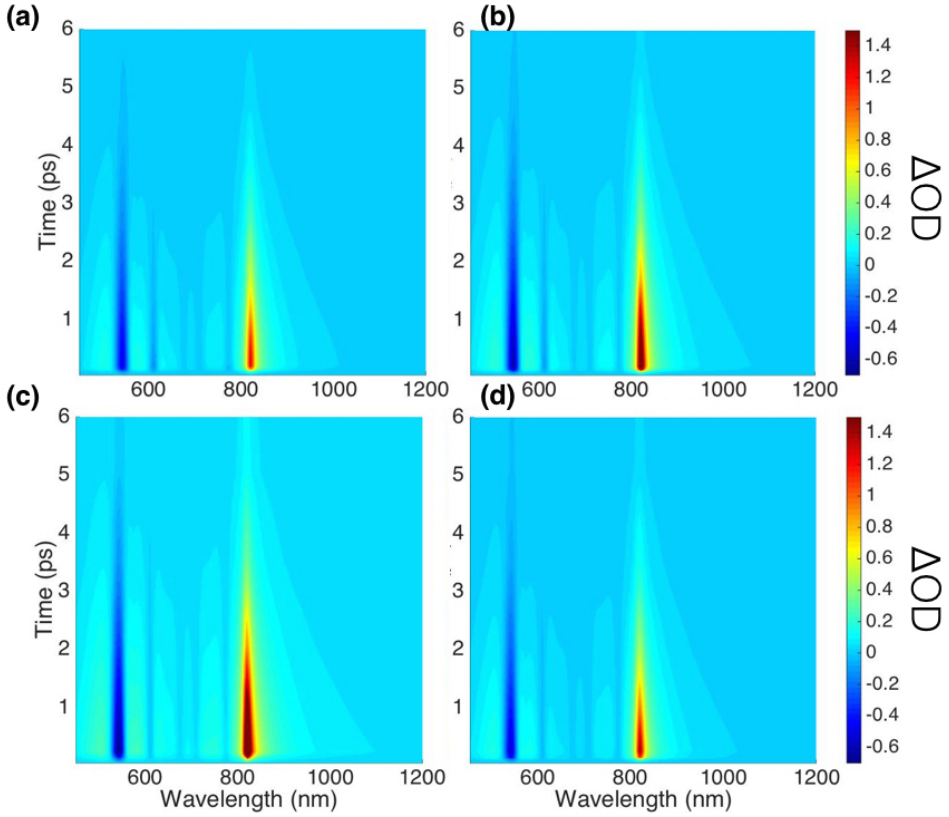

FIGURE 6.30: a) Transient extinction map of the metamaterial pumped at (a) 670 nm, (b) 730 nm, (c) 830 nm, (d) 1085 nm always at an angle of incidence of 60^o, and probed with a TM polarized wave at 20^o incidence.

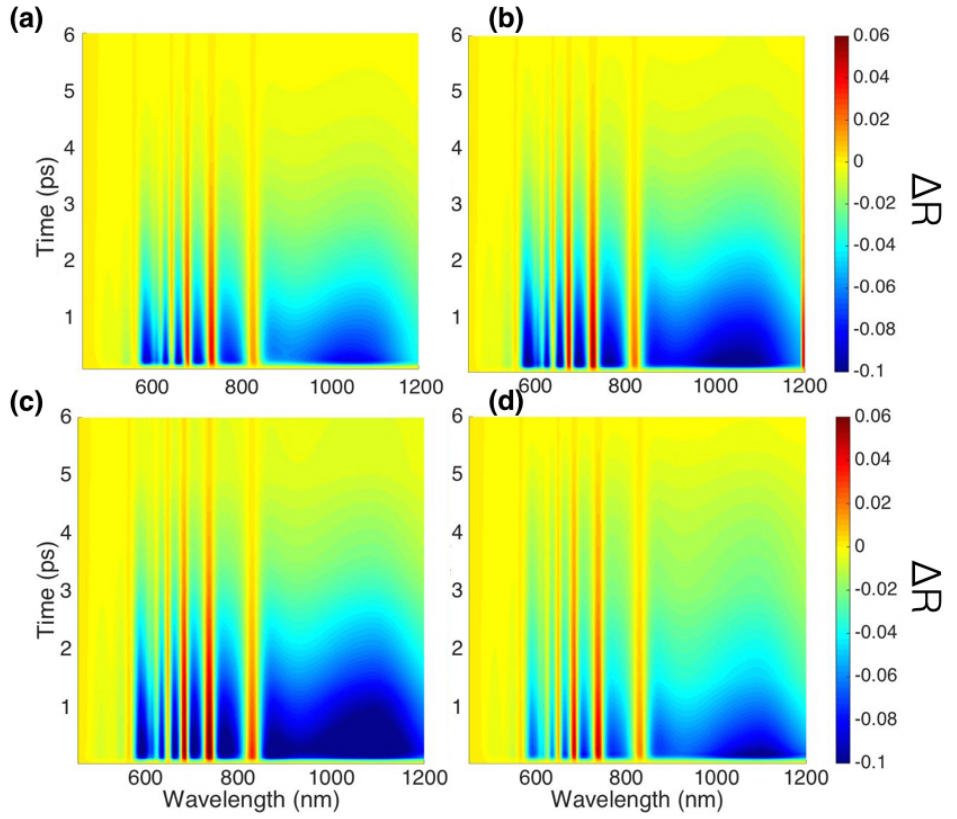

FIGURE 6.31: a) Transient reflection map of the metamaterial pumped at (a) 670 nm, (b) 730 nm, (c) 830 nm, (d) 1085 nm always with an angle of incidence of 60^o, and probed with a TM polarized wave at 60^o incidence.

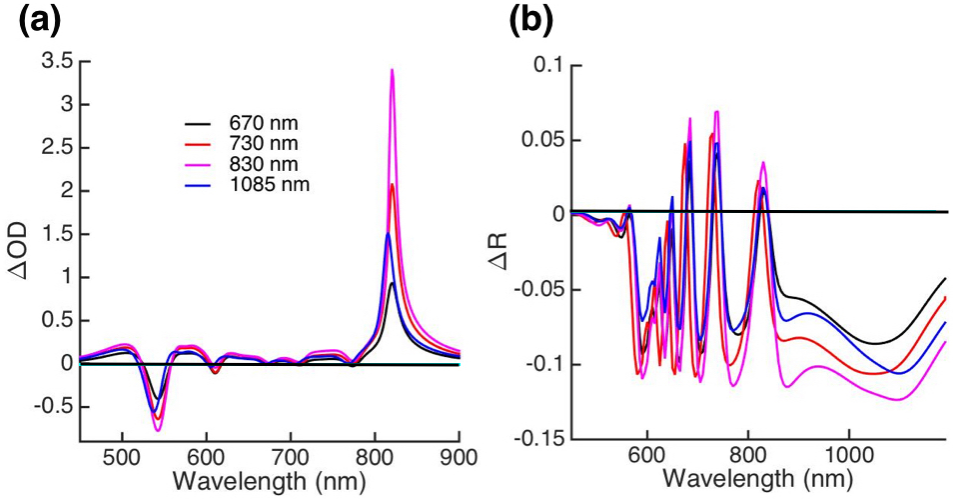

FIGURE 6.32: a) Transient extinction of the metamaterial pumped at the waveguided modes and probed with a TM polarized wave at 20^o incidence and (b) transient reflection of the metamaterial pumped at the waveguided modes and probed with a TM polarized wave at 60^o incidence.

The cross sections plotted in Figure 6.32 give a snapshot of the differential extinction spectra as obtained for maximum modulation. Qualitatively, transient extinction maps give an indication of the amount of power absorbed from the pump at the various pumping wavelengths, with most power transferred to the metamaterial at a pumping wavelength of 830 nm, followed in decreasing order by the pumps at 730nm, 1085nm, and 670 nm. Another information retrieved from the transient extinction measurements is in the relative change in the amplitude of the modulation at both T- and L-mode frequencies, reaching an extinction change of 0.3 and 2.5 at those respective frequencies. This is indicative of the stronger value in the overlap integral at the L-mode frequency.

We have fitted the dynamics of the differential optical extinctions for all the pump configurations considered with a linear combination of exponential functions, considering two probing wavelengths at 20^o incidence, one in the elliptic and one in the ENZ, specifically 550 nm, in the proximity of the T-mode, and 820 nm, at the L-mode.

While the probing T-mode determines a single time decay constant, consistently around 2 ps for all the different pump configurations, the L-mode shows a much more diversified reading capability. For the pump off-resonance at 465 nm, a single time decay component around 1.3 ps can be determined. For the pump at the L-mode, the dynamic can be well reproduced by a combination of two exponentals, as mentioned above, one of which has a time constant of the order of 100 fs and the other one of the order of 1.4 ps. For the pumping negative group velocity modes situated well above the ENZ frequency (670 and 730 nm), the time decay constant is around 1.6 ps, while for the pump centered at the wavelength corresponding to negative group velocity modes close to or below ENZ (830 nm and 1085 nm), the decay constant is slightly reduced, around 1.3 ps.

We have similarly analyzed the dynamic behavior of the differential optical reflection, considering the probe at 60^o incidence, at the wavelengths where the most significant negative modulation occurs. The significant probing wavelengths are at 655 nm, 695 nm, 770 nm, 1050 nm for the pump in the elliptic regime (corresponding to the shift of the waveguide modes), at the L-mode and at the

waveguide mode located below the local ENZ. For the pump in the elliptic regime, at both angles of incidence of 20^o and 0^o, the most significant modulation happens at 655 nm. The dynamic of the differential reflection can be fitted with a single exponential, with a characteristic time of 2.2 ps. Considering the probing light at the other wavlengths, the fitting with a singl exponential gives consistently a characteristic relaxation time of 2 ps.

For the pump at 820 nm, the most significant modulation occurs with a probing wavelength of 1050 nm. The dynamic of the modulation in the configuration where the pump is at normal incidence can be fitted with a single exponential, and a relaxation time decay of 1.1 ps can be extracted. In the case of the non normal incidence pump exciting the L-mode, the relaxation can be fitted with a linear combination of 2 exponentials, giving time relaxation constants of 0.9 and 1 ps. The dynamics at the other probing wavelengths can be fitted with a single exponential, with decay time constants around 2.

When exciting the waveguide mode at 670 nm, 60^o incidence, the reflection modulation relaxation determines a single characteristic time of 1.7 ps, probing the system at 665 nm, where the biggest modulation occurs. The other negative modulation peaks decay can be as well fitted with a single exponential, with a characteristic time around 2 ps. Exciting the waveguide mode at 730 nm, a single exponential provides a good fit, with time constants around 1.4 ps.

For the pump exciting the waveguide modes located above the local ENZ frequency, the biggest negative reflection modulation happens at 1090 nm. In both configurations (pump at 830 nm and 1085 nm), the relaxaton dynamics at this wavelength can be fitted with a single exponential, with a time constant of around 1.2 ps. The system's dynamic when pumped at 830 nm and probed at 660 and 710 nm, is fitted with a linear combination of two exponentials, with two time relaxation constants, one of 1 ps and one of 1.3 ps. In the case of the pump exciting the waveguide mode at 1085 nm, all the significant dynamics can be fitted with a single exponential, with values around 1.2 ps.

6.2.4 Comparison with experimental measurements

In order to understand the importance of the $\frac{\partial OD}{\partial \epsilon}$ term, we have analyzed the dynamic optical relaxation of the system in the absence of the optical pump, and compared the results obtained in this conditions with eperimental measurements. There is thus no spatial dependence of the absorption and as a consequence of the electrons temperature given by $\nabla(kT\vec{\nabla}T)$. A homogeneous power dissipation density is used to increase the electron temperature up to a value of 1043 K, consequently also homogeneous across the nanorods. This temperature has been chosen as it is the maximum volume averaged temperature reached by the gold electrons usng a pump centered at 820 nm, with an angle of incidence of 20^o. The system then relaxes in the absence of any additional pump-driven power dissipation. The dynamic differential optical extinction and reflection are observed, for a probe beam at 20^o incidence and 60^o incidence, respectively.
The linear modes of the metamaterial will probe the same temperature, but are expected to show absolute modulation amplitude and relaxation dynamics based on material dispersion and modal field distribution.

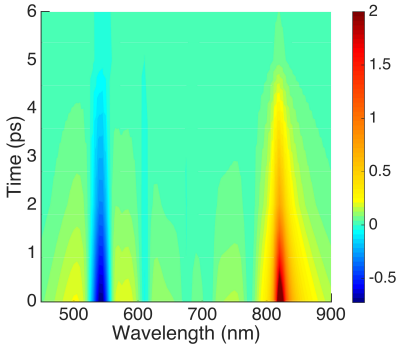

FIGURE 6.33: Time evolution of the differential optical extinction of the nanorod metamaterial, for a homogeneous initial electrons temperature of 1043 K and a probe beam incident at an angle of 20^o.

Figure 6.33 shows the time evolution of the optical extinciton of the metamaterial in the conditions outlined above. The nonlinear modulation is detected mainly by the two dominant modes, in fact the main dynamic features are around 520 nm, corresponding to the T-mode, and between 780 and 900 nm, corresponding to the L-mode. The greatest nonlinear modulation is obtained at 820 nm, with a value of ΔOD of 2.9. The modulation is weaker when considering the T-mode

as the probing resonance, with a maximum absolute value $|\Delta OD|$ of 0.7. The T-mode shows a negative nonlinear modulation between 520 nm and 565 nm. Fitting the relaxation dynamics in this wavelength region with a linear combination of exponentials, it is possible to recover a time relaxation constant between 1.25 ps and 1.7 ps. The number of exponential terms that allow to obtain a good fit varies between 1 at the T-mode wavelength, 520 nm, and 2 for wavelengths around it. For the second strong nonlinear modulation signature close to the ENZ frequency and to the L mode, the relaxation shows a single time decay component at the L-mode wavelength, 820 nm, with a value of 1.4 ps. This confirms that the fast, subpicosecond component of the decay, is due to the presence of the divergence term.

The relaxation is faster for wavelengths below and above 820 nm, with a value around 1.1-1.2 ps. Thus the L-mode, as could be seen also from the complete pump-probe data, is the most sensitive mode to the nonlinear modulation, and the time resolution of the system's modulation in these conditions has an optimal performance at 815 nm, where the time decay constant has a value of 1.1 ps.

It is interesting to identify the main contribution to the observed nonlinear response modulated by nonlocality as originating from an increase in the intraband damping constant in ϵ_{Au}. This leads to the modification of the real part of the metal's permittivity leading to the red-shift of the L-mode. However, the main effect comes from the increase in the imaginary part of the metal's permittivity, as can be seen in Figure 6.34. The variation of the imaginary part of the metal's permittivity is of the order of 30% comparing the dielectric permittivity at 300 K and 1043 K at the L-mode wavelength.

A homogeneous temperature distribution has been used to reproduce previous experimental results [87], in which a nonlocal system has been used. In the experiment, the split output laser of a regenerated 800 nm wavelength, 100 fs laser pumps an OPA cavity to produce a pump beam with a wavelength tunable from 450 nm to 770 nm. The remainder of the regenerated pulse is directed to a delay line and focused into a 1 mm thick sapphire substrate to produce the white light continuum used to probe the dynamics of the sample following optical excitation

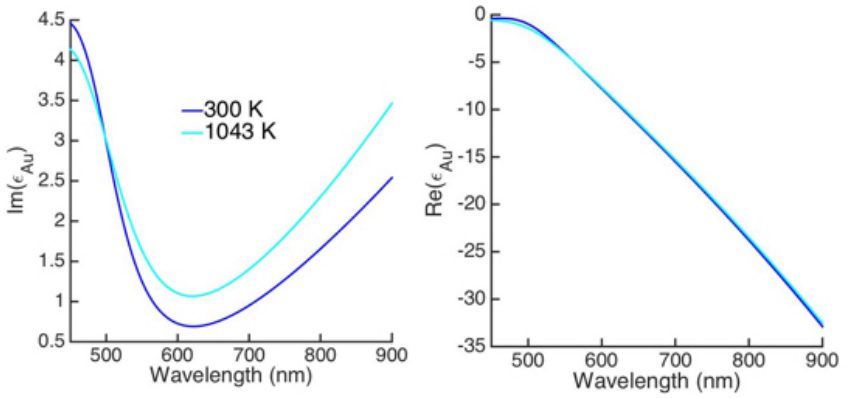

FIGURE 6.34: a) real and b) imaginary part of the dielectric permittivity of gold for two different electrons temperature, 1043 K and 300 K.

by the pump beam. The delay line controls the temporal delay τ between probe and pump beams over a maximum of 3.5 ns with a sub-20 fs time resolution. For this experiment, both beams are TM polarized so as to couple to both plasmonic modes for non-zero angle of incidence, and overlap spatially on the sample where they are weakly focused on a 200 μm diameter spot. The beams are incident on the sample at angles differing by about 3 degrees for spatial discrimination after transmission through the sample. The probe beam, transmitted through the sample, is sent to a spectrometer via a 50 μm core diameter fiber and subsequently processed to determine the transient response of the sample as a function of free-space wavelength of the probe radiation λ_0 for a set time delay τ. Figure 6.35 shows a schematic of the experimental setup.

Further details on the experimental set-up can be also found in [87]. Figure 6.36 plots the experimental results obtained in these conditions, where (a) represent the transient optical density map $\Delta OD = -log_{10}(T_{ON}/T_{OFF})$ for an incident angle of 40^o, where T_{ON} is the transmission of the sample following excitation by the pump beam at finite time τ and T_{OFF} is the transmission of the sample in the ground state, i.e. when $\tau = \infty$. The same definition for the transient extinction is used in the simulations to perform the experimental measurements fitting. (b) presents cross-section spectra of (a) taken at selected time delays, while (c) shows the sensitivity of the transient signal measured for different angles of incidence at a constant time delay.

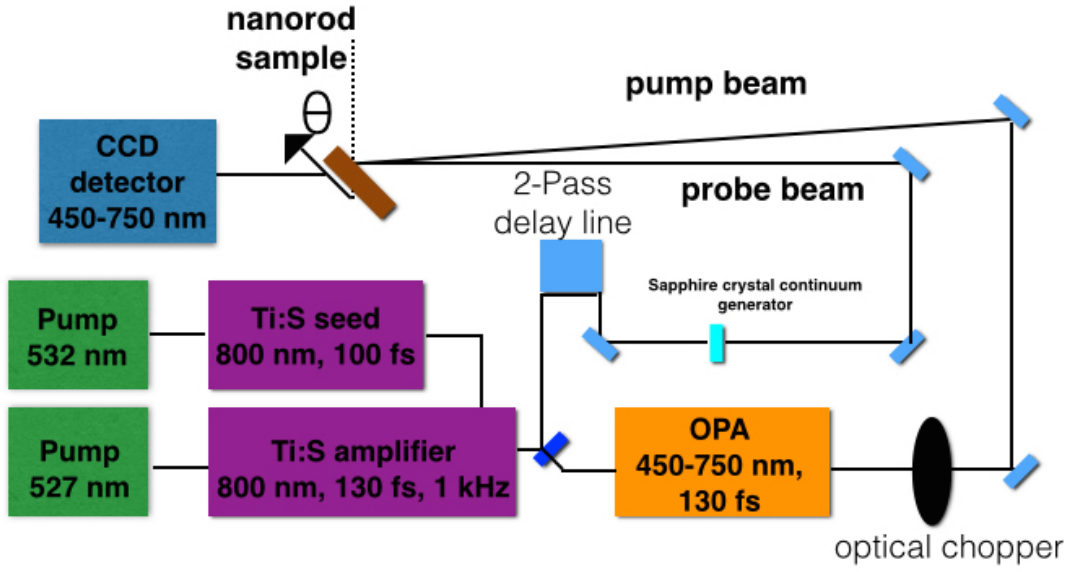

FIGURE 6.35: Schematic of the pump-probe experimental setup

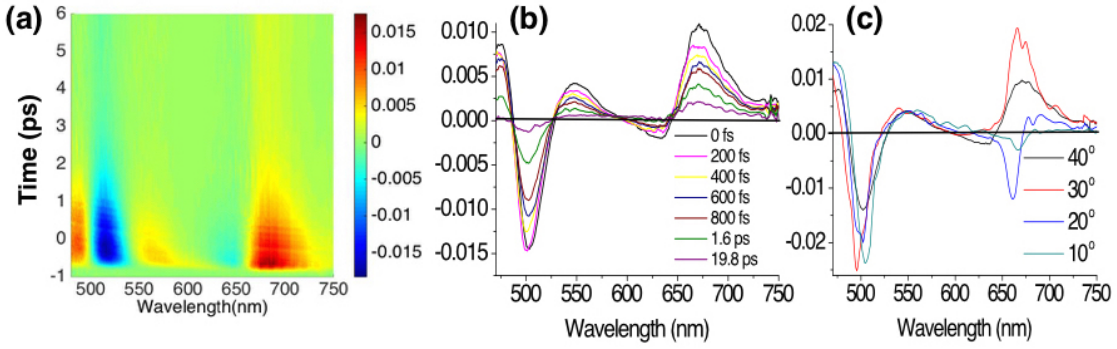

FIGURE 6.36: Transient extinction map, measured for a metamaterial similar to that in Fig. 2b, for TM-polarized probe light at an angle of incidence of 40 degrees. The pump wavelength and fluence are 465 nm and 0.7 mJ/cm2. (b) Cross-sections (a) showing the transient extinction spectra at various time delays between pump and probe beams. Spectrum '0 fs' corresponds to the spectrum of the metamaterial measured directly after optical pumping. The other transient spectra correspond to increasing pump–probe time delays τ. (c) Transient extinction spectra at τ=200 fs measured for different angles of incidence.

In Figure 6.37 though, the numerical calculation has been performed to reproduce the experimental results considering a homogeneous temperature distribution of the electrons temperature inside the gold nanorods. The power dissipation density has been adjusted in order to fit the experimental measurements.

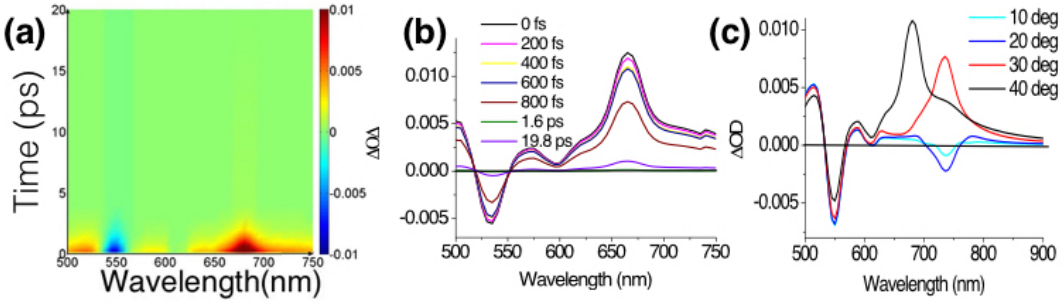

FIGURE 6.37: Numerically modelled transient spectra corresponding to the experimental situation described in Figure 3, (a) extinction map, (b) extinction spectra at selected delay times and (c) transient extinction spectra at tau=200 fs at different angles of incidence. The transient spectra are obtained by considering a spatially homogeneous permittivity for Au extracted from the TTM. For the FEM calculations of the transient response R = 30 nm was used which reproduces both static and dynamic optical response of the metamaterial. For the calculations the rod diameter, length, and spacing are 35 nm, 350 nm, and 90 nm, respectively.

6.3 Summary

In this Chapter, I have shown the results of the theoretical and numerical model I have developed, and that has been described in Chapter 2 and 3, to simulate the dynamic nonlinear optical response of a gold nanorod metamaterial.

In particular, I have simulated a pump-probe experiment, changing the configuration of the control and signal light in terms of wavelength and angle of incidence. In fact, the plasmonic resonant modes of the metamaterial have been exploited as mediators of the nonlinear Kerr effect in gold and as probes. The dynamic behaviour of the difference between the nonlinear and linear extinction and reflection of the metamaterial has been considered.

I have shown that the field profile of the resonant mode used to pump the system is mapped into the electrons temperature distribution of the excited system.

This determines different dynamics of the temperature in different parts of the nanorods, although the volume averaged temperature decay rate is not affected by the inhomogeneities. The presence of temperature inhomogeneities determines an enhancement of the nonlinear modulation extinction amplitude of approximateley 30%, when probing the system with the L-mode. I have shown theoretically and numerically that the divergence term in the first of equations 2.55 determines a faster dynamic for the electrons temperature and, as a consequence, of the transient optical response. By appropriately combining the pump and probe electric field profiles, it is possible to maximize the effect of the divergence, sampling only the regions of the nanorods where its effect is stronger and obtaining an optimized response in terms of the time decay. I have shown that combining pump and probe corresponding to the metamaterial's L-mode, the dynamic of the transient extinction shows a fast decay component around 0.1 ps.

I have also shown that nonlocality enables the presence of hyperbolic, waveguided modes above the local epsilon near zero condition, which determine as well a dynamic response of the system with a decay constant between 1.2 and 1.6 ps.

Chapter 7

Ultrafast dynamics of weak and strong exciton-plasmon coupling in hybrid nanorod metamaterials

In this chapter, I will examine theoretically and numerically the formation of hybrid plasmonic-excitonic states in assemblies of aligned gold (Au) nanorods surrounded by a shell of J-aggregate supporting a molecular excitonic transition dipole moment. The flexible geometry of the metamaterial will be used to control the position of the J-aggregate in the plasmonic structure as well as the mixing of the hybrid system's eigenstates, offering a unique possibility in the design of molecular plasmonic nanodevices with tailored optoelectronic functionalities. The dynamic optical response of the system will be analyzed in order to understand its modulation capabilities.

7.1 Hybrid plasmonic structures

The properties of SPPs and LSPRs can be used to actively manipulate optical signals also in hybrid plasmonic structures. For example, plasmonic modes can induce linear or nonlinear variations in the optical properties of an embedding dielectric material not observed in the optical response of both subsystems when isolated. Two main operational regimes of hybridized plasmonic structures can be

identified as originating from a weak or strong electromagnetic coupling between plasmonic modes and modes supported by a host or guest medium.

Weakly coupled systems can be described by the eigenmodes of the isolated entities, essentially unperturbed by the coupling, with the optical properties of the hybrid found by treating the subsystems as coherent oscillators. In the weak coupling regime, a silver SPP interferometer covered with a layer of CdSe quantum dots was used to demonstrate switching of a control signal on a timescale of a few tens of ns. The transmission of SPPs through a slit is controlled by the nonlinear absorption of the quantum dots [91]. Similarly, ultrafast modulation was achieved using an SPP supported by a gold/ITO interface, in a regime in which ITO has a vanishing real part of the permittivity. In this regime the SPP at the interface between ITO and gold can be coupled using air as a wavevector-matching medium. The hybrid system, pumped with a pulsed control laser, demonstrates a differential reflectivity reaching 20% for a fluence of 10 mJ/cm^2. The nonlinear effect driving the reflectivity modulation in this system is the gold-mediated hot electron injection in ITO, which controls the SPP dispersion [92].

Localized Surface Plasmon Resonances (LSPs) have also been weakly coupled to nonlinear materials to perform active optical functionalities. For example, ultrafast all-optical signal modulation was achieved in a hybrid gold nanoantenna-ITO plasmonic system, based on the hot electron transfer process similar to the one previously described. In this configuration, the LSP of the nanoantenna generates a change of the free carrier density in the neighboring ITO, allowing for a nonlinear change of its refractive index. This modifies the dipolar mode of the nanoantenna and its subsequent reflectivity to a value on the order of 2% at pump energies of 180 pJ [93].

Hybrid plasmonic metamaterials have also shown remarkable modulation capabilities. For example, the variation of the free carrier density in the semiconducting dielectric component of a fishnet metamaterial, driven by localized plasmonic fields, is at the origin of its ultrafast nonlinear optical response. This metamaterial consists of an amorphous silicon (a-Si) layer embedded between silver (Ag) cladding layers. In this system, the change in the refractive index of the a-Si,

mediated by the plasmon resonances of the structure in the near IR, produces a variation in transmission and reflection of about 30% and 40%, respectively, with a pump fluence of 300 μJ/cm^2. The fast component of the system's recovery time was characterized to be on the order of 750 fs [94].

All-optical switching was demonstrated with split ring slit arrays hybridized with semiconducting single-walled carbon nanotubes. This metamaterial has demonstrated a relative transmission change of 10% with a recovery time of 500 fs, achieved at a pump fluence of 10 μJ/cm^2 [95].

A hyperbolic metamaterial, consisting of alternated Kerr-type nonlinear dielectric and lossless Ag layers, has shown numerically to provide a variation of refractivity from positive to negative under a varying incident control intensity at 311 nm and for power densities on the order of GW/cm^2 [96].

These examples show the benefits in operating in the weak coupling regime as essentially resting on the fundamental properties for which plasmonic modes are broadly used, i.e. for the spectral sensitivity and localized field enhancement associated with their resonant response.

In the strong coupling regime, the eigenmodes of the hybrid system can be described as resulting from the mixing of the eigenmodes supported by the constituting entities [97].

Strong coupling was observed in different systems including microcavities where the quasiparticle comprises a cavity photon and a molecular exciton [98, 99], in plasmonic systems involving a SP and a waveguide photon [100] and between a SP and an exciton [101–104].

Strong coupled exciton-plasmon systems have recently attracted considerable attention. Excitonic states, which are electrically neutral electrons/holes pairs, created by the absorption of photons, are used in photosynthetic processes by plants to collect, store, and guide energy to the reaction center for energy conversion and could therefore drive artificial devices on identical principles. Organic semiconductor materials, such as J-aggregates, support excitonic transitions and have a very low manufacturing cost and remarkable electrochemical and mechanical stability. Moreover, they have a very efficient interaction with light, provided

by their large oscillator strength [102], and their optical properties can be drastically modified by their environment. In particular, the strong light-matter coupling regime can be reached, inducing dramatic modifications of the energy transition and dynamic behavior.

J-aggregates, as the name suggests, are aggregates of unit-cell molecules, i.e. monomers assembled in a chain-like structure, resulting from the self-assembly of monomers in high concentration solutions and thin solid films. The aggregate is characterized by an absorption band which is redshifted and narrowed with respect to the monomer's absorption and corresponding to an excitonic eigenstate delocalized over the aggregate. The coherence length of the exciton is the characteristic size of the aggregate over which the excitonic state is delocalized [105–108], determining both the spectral position and linewidth of the excitonic absorption band. This length differs from the physical size of the molecular aggregate, and can be easily determined optically. If a defect is present within the actual size of the molecular aggregate, it will become a scattering point of an exciton, which will not be able to propagate along the entire monomer chain. The closer the coherence length to the actual monomer chain size, the lower the potential energy of the exciton, and the greater its stability. In a stable state, the linewidth of the optical absorption spectrum corresponding to the excitonic transition is narrowed with respect to the monomer absorption. The more delocalized the excitonic state, the more redshifted and narrow will be its absorption band.

The interest of coupling molecular excitons to plasmonic excitations is in the the very strong nonlinear optical behavior these systems demonstrate and which could ultimately be used to produce stimulated nanosources of photons and transistor like action. Additionally, molecular excitons have relatively large polarizability and optical extinction, which makes the coupling through linear or nonlinear processes to an inorganic substrate very strong. It has been underlined in Chapter 2 how metal nanoparticles are able to enhance the optical field in their immediate surroundings, due to their resonant polarizability. They thereby represent ideal candidates to interact strongly with molecular excitons. For example, the important scattering cross section of silver nanoparticles covered with J-aggregate has

been used to induce stimulated emission from the molecular excitons, with very low excitation powers [109].

Ultrafast Rabi oscillations between excitons and plasmons have also been observed in a hybrid nanostructure consisting of a 50-nm-thick film of J-aggregate molecules in a polymer matrix coated onto a gold nanoslit array. The SPPs in the proximity of the slits are strongly coupled to the molecular aggregate. When the system is pumped at 688 nm, a relative reflection variation of 0.02 is modulated on a 10 fs timescale by the exciton population [110] at 751 nm, with a fluence of 30 μJ/cm^2.

The ultrafast reversal of a Fano resonance has been studied theoretically in a strongly coupled system consisting of a two-level quantum dot/plasmonic nanoantenna. The reason for the reversal is interpreted as a transient change in the phase of the dipoles of the plasmon and exciton and happens on a timescale of tens of femtoseconds. The system is pumped and probed at 607 nm, with a fluence between 10^{-10} and 10^{-7} J/cm^2 [111].

7.2 Linear response of the hybrid nanorod/J-aggregate metamaterial

The way in which the metamaterial and J-aggregate eigenmodes hybridization is performed in the present work, is the spatial and spectral overlap between the plasmonic resonant modes and the exciton dipole transition moment.

The spatial overlap between the two systems, the metamaterial and the organic polymer, is obtained by creating a void shell around the gold nanorods, in which the J-aggregate is placed.

Experimentally, the void shell is obtained through a simple chemical etching reaction, that guarantees the creation of a shell of uniform and tuneable thickness. Such coreshell geometry, illustrated in Figure 7.1, opens up unique opportunities to, controllably, couple plasmonic structures with their environment.The monomer dye is introduced in the shell and subsequently, the monomer adsorbs on the gold nanorod surface in the form of a J-aggregate. The thickness of the shell

represents an additional geometrical parameter with respect to the gold nanorod array investigated in Chapter 6, allowing one to tune the optical properties of the plasmonic structure without changing the original nanorod geometry. The precise tunabilty of the shell thickness also guarantees spatial selectivity to couple the plasmonic resonances with active molecules.

The spectral overlap between the plasmonic resonances and the excitonic transition is obtained considering the L-mode as the metamaterial eigenmode. The geometrical parameters of the metamaterial have been tuned in order for the L-mode to be spectrally superimposed to the J-aggregate excitonic resonance.

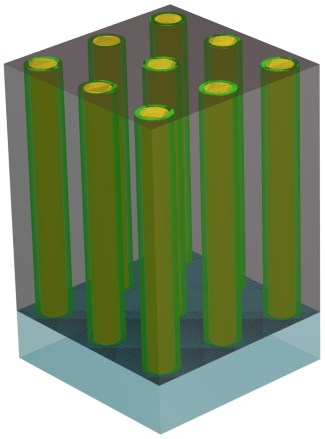

FIGURE 7.1: Schematic of the coreshell nanorod metamaterial

The excitonic transition of the J-aggregate is situated at 622 nm. The exciton resonance has been modelled assuming a Lorentzian absorption lineshape, i.e. a homogeneously broadened absorption [85], in a dielectric background with $\epsilon_\infty = 1.44$ and transition frequency $\omega_0 = 3.03^{15}$ rad/s, reduced oscillator strength $f = 0.2^{15}$ rad/s, and linewidth $\gamma_{agg} = 0.05/\hbar$ rad/s [86]. The dielectric response of the aggregate can then be expressed as

$$\epsilon_{Jagg} = \epsilon_\infty + \frac{f\omega_0^2}{\omega_0^2 - \omega^2 - i\omega f} \tag{7.1}$$

In order to obtain the overlap, we have taylored the geometry of the nanorod array considering a 'reference' coreshell structure. This structure consists of the usual square array of gold nanorods, surrounded by a shell with a refractive index of

$n = 1.2$, which is the saturating value of the J-aggregate refractive index for high frequencies. Observing through the optical extinction of such metamaterial the spectral shift of the L-mode when changing the shell thickness, it is possible to taylor the optical response in order to locate the resonance around the excitonic transition wavelength. We have determined a shell of thickness 20 nm around them in order to have the L-mode at around 621 nm, or in spectral resonance with the exciton absorption when present in the shell. The dielectric permittivity of the J-aggregate is shown in Figure 7.2. The geometrical parameters of the metamaterial have been set as 35 nm for the diameter, 250 nm for the length and 80 nm for the center-to-center distance.

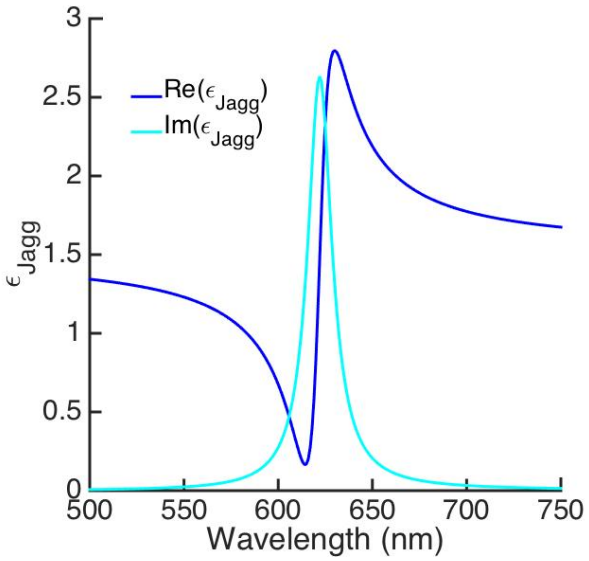

FIGURE 7.2: Real and imaginary part of the dielectric permittivity of the J-aggregate modelled as a Lorentzian function with the parameters specified for Equation 7.1.

Figure 7.3 (a) and (b) show the optical extinction spectrum of the geometry just considered and the optical extinction of this same core/shell structure, once the resonant nature of the aggregate is accounted for, respectively.

Having a spectral overlap between the resonant absorption of the two systems, strong coupling is achieved. It is possible to see how the L-mode and the excitonic transitions couple and become two new modes, one blueshifted and the other redshifted with respect to the initial position of the L-mode and excitonic resonances in the uncoupled isolated systems. By varying the thickness of the shell around

the nanorods in the plasmonic metamaterial, it is possible to tune the frequency of the L-mode with regards to the exciton and therefore to transition from a strong coupling regime to a weak coupling regime. Figure 7.3 (a) and (b) show the extinction spectra of the hybrid metamaterial as the shell thickness is tuned from 5 nm to 20 nm. For the smallest shell thickness, the spectral overlap between L-mode and exciton resonance is relatively small leading to weak coupling between the two eigenmodes. For this geometry, the L-mode is simply redshifted with respect to the original position and the resonant absorption of the J-aggregate remains at around 622 nm. The figure demonstrates the occurrence of strong coupling as a bi-modal splitting (anti-crossing) in the spectrum, opening a gap between 1.9 eV and 2.01 eV, visible in Figure 7.3 (c). Previous experiments have used a similar strategy to control the exciton-plasmon coupling strength [97]. The calculations can also be performed in the effective medium approximation, assuming the absence of nonlocal effects. In this case we have considered an anisotropic dielectric permittivity of the shell, with the only component of the dielectric permittivity tensor of the exciton assumed to be resonant along the nanorod symmetry axis.

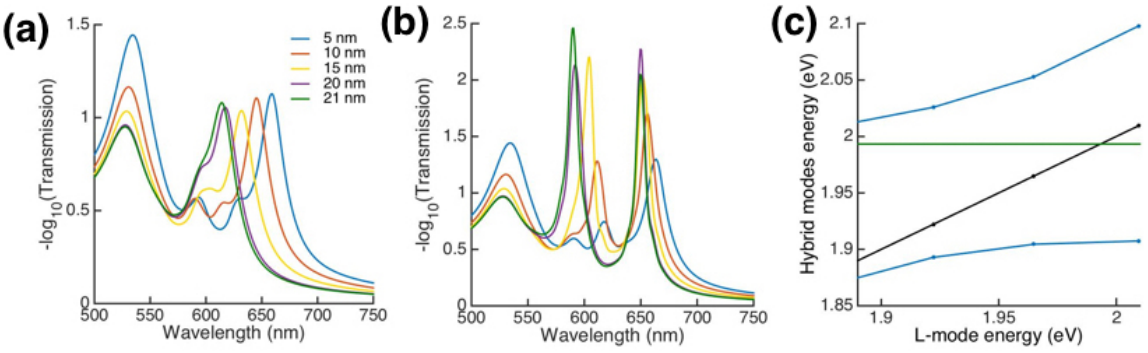

FIGURE 7.3: Numerical calculation of the extinction spectra of the core-shell J-aggregate hybridized metamaterial for varying shell thicknesses. (a) shows the system with a non-resonant aggregate shell, (b) shows the system with a resonant J-aggregate shell along the nanorod symmetry axis. (c) shows the resulting anticrossing diagram, with the hybrid modes in blue, the plasmon energy in black and the Jaggregate excitonic transition energy in green.

Figure 7.3 (a) shows the extinction spectra of the reference core-shell metamaterial, when no exciton is present in the shell and its thickness is varied between

5 and 21 nm. The metamaterial's L-mode then spans the wavelength region between 600 nm and 660 nm, across the strong coupling spectral region. Figure 7.3 (b) shows the correspondent spectra when the J-aggregate is present in the shell. It is possible to see how the two modes characterizing the strong coupling regime gradually disappear leaving only the remaining J-aggregate enhanced absorption around 622 nm and the redshifted L-mode around 670 nm.

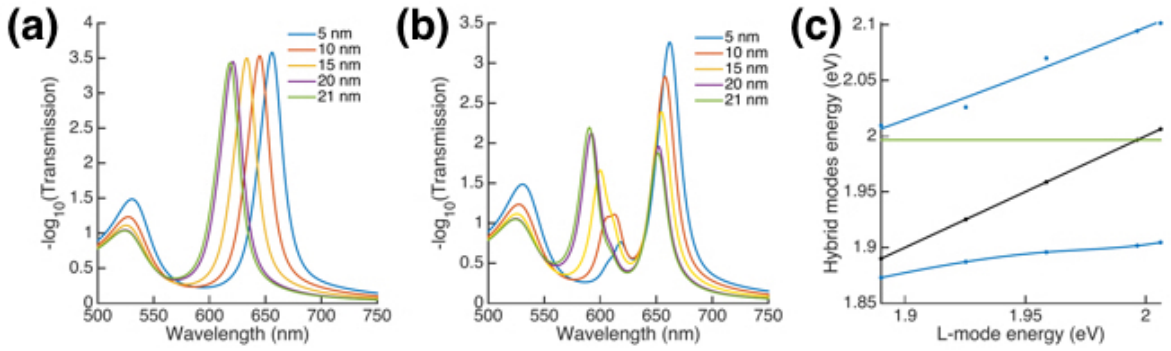

FIGURE 7.4: EMT calculation of the extinction spectra of the J-aggregate hybridized metamaterial for varying shell thicknesses of the J-aggregate. (a) shows the system with a non resonant J-aggregate shell, (b) shows the system with a resonant J-aggregate shell along the nanorod symmetry axis. (c) shows the resulting anticrossing diagram, with the hybrid modes in blue, the plasmon energy in black and the J-aggregate excitonic transition energy in green.

Figure 7.4 shows the same calculation as 7.3, performed with EMT. The anticrossing is reproduced even in the Effective Medium approximation, which again shows to be a valuable tool to model the core-shell system reliably.

Figure 7.5 shows the linear dispersions observed through the (a) extinction and (b) reflection in the strong coupling regime. The L-mode of the plasmonic metamaterial and the excitonic transition, which was previously situated around 2 eV in the extinction dispersion, do not appear anymore. They have been replaced by two dispersive hybrid modes starting at 1.9 and 2.1 eV. These hybrid modes show the nonlocal behaviour inherited from the plasmonic resonance.

Figure 7.6 shows the linear dispersions of the hybrid metamaterial observed through the extinction and reflection in the weak coupling regime. Here, the dispersion is dominated by the nonlocal L-mode, unaffected by the exciton transition

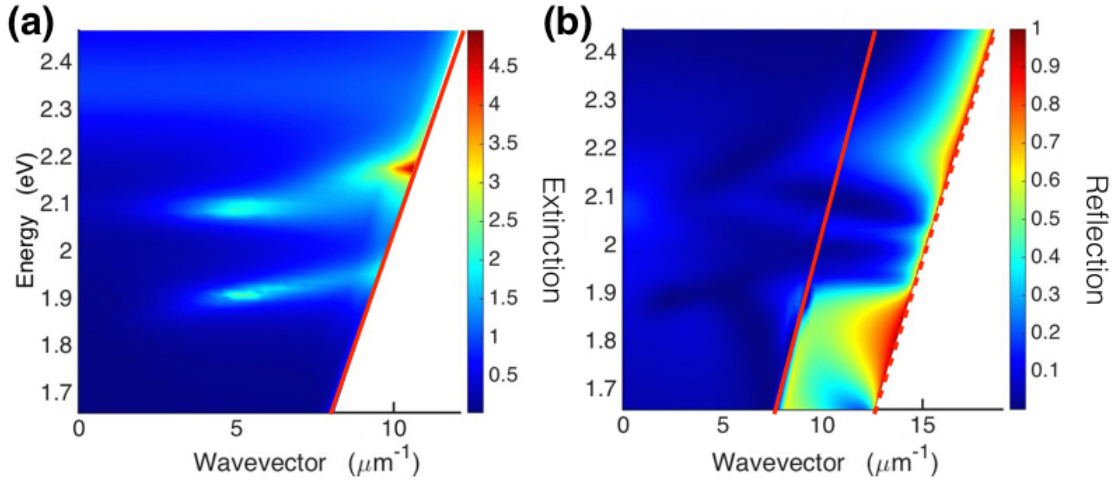

FIGURE 7.5: (a) shows the extinction dispersion of the strong coupled system, illuminated by a TM polarized plane wave. (b) shows the reflection dispersion. Both are calculated numerically.

dipole, which on the contrary has no angular dependence and can be seen at 2 eV for all wavevectors of the incident light.

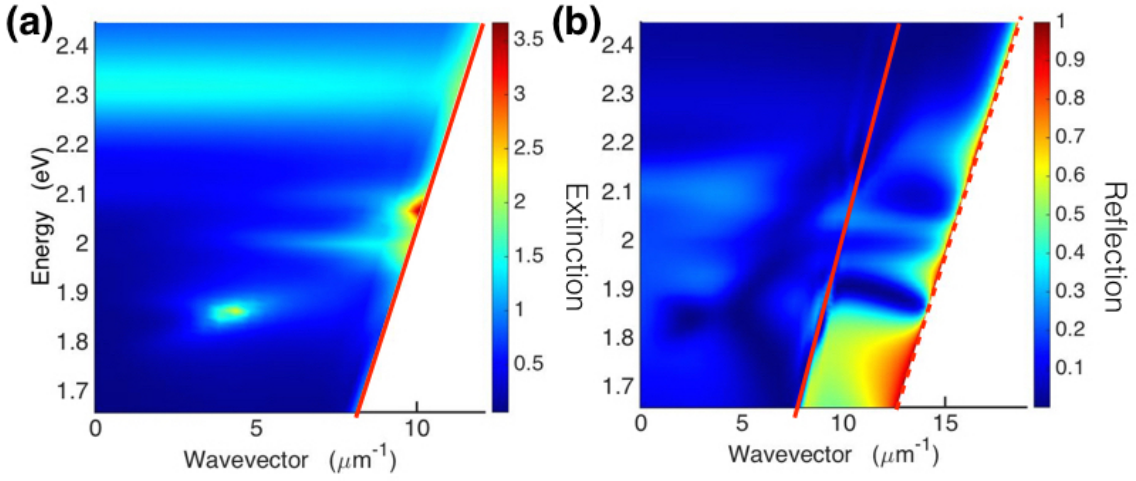

FIGURE 7.6: (a) shows the extinction dispersion of the weak coupled system, illuminated by a TM polarized plane wave. (b) shows the reflection dispersion. Both are calculated numerically.

7.2.1 Nonlinear response of the coreshell naorod metamaterial: strong coupling regime

Similarly to the case of the gold nanorod metamaterial, we have performed pump-probe simulations on the nanorod/J-aggregate hybrid system.

In a first set of numerical calculations, the transient behavior of the hybrid system was assumed to originate solely from the Au nanorods, leaving the molecular aggregate unaffected by the optical pump. We know this to be a gross approximation, but it was done at first to quantify/qualify the contribution of Au, and of the underlying plasmonic response of the metamaterial, in the transient response of the hybrid structure. Additionally, the transient response of the molecular aggregate to an optical stimulus, when adsorbed on a nanostructured metallic surface, is far from trivial, necessitating more evolved quantum mechanical models. A more straightforward model, assuming a stationary excited state of the molecular aggregate, can be used to reproduce the experimental observations, but with no factual information on the dynamics of the system. The hybrid metamaterial has been pumped in two configurations. The first has an exciting pulse centered at 465 nm, in the interband absorption region, at 20^o incidence, and the second has an exciting pulse centered at 590 nm, corresponding to the wavelength of the high energy hybrid mode, and an angle of incidence of 20^o. Both configurations correspond to experimental situations.

The qualitative features of the calculated nonlinear response of the system for the two configurations are very similar and are shown in Figure 7.7. The maximum modulation of the extinction appears in the transient signal at wavelengths in the proximity of the two hybrid modes. The remarkable feature is a change in sign that occurs around an angle of incidence of the probe of 20^o. Figure 7.7 (b) shows the difference between the differential extinction dispersion obtained for the pumping wavelength at 465 nm and that obtained for pumping wavelength of 590 nm. The maximum differential modulation obtained for the pump centered at 590 nm has a greater modulation in absolute value, as expected when pumping the resonance of the hybrid metamaterial. However, the response of the system is qualitatively identical to that observed at a wavelength of 465 nm, ill-reproducing the experimental results. We have thus examined the dynamic of the nonlinear response of the system for three representative angles of incidence of the probe light, 10^o, 18^o and 20^o.

Figure 7.8 shows the time evolution of the differential optical extinction of

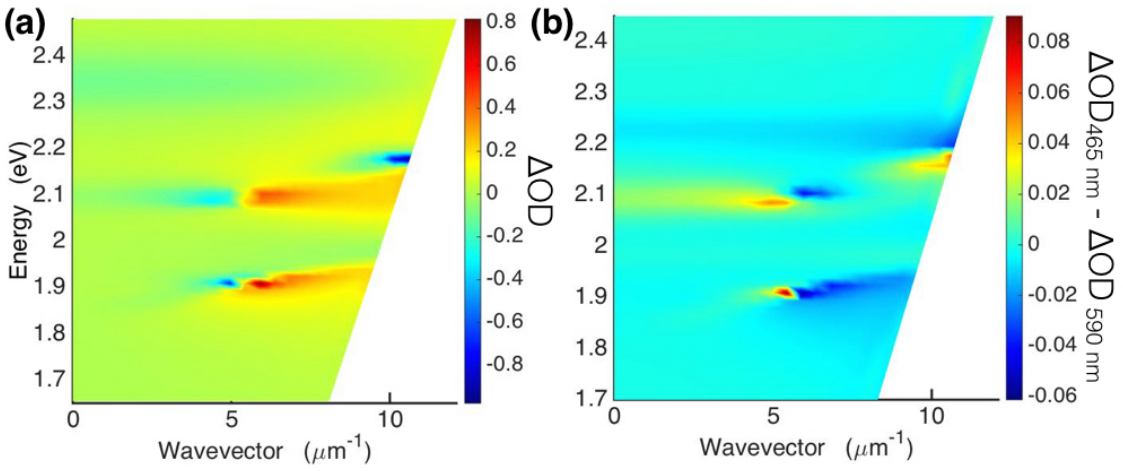

FIGURE 7.7: Strong coupled system transient extinction results. (a) Dispersion of the difference between the optical extinction of the gold nanorod core, J-aggregate shell metamaterial in the linear regime, assuming a homogeneous temperature of 300 K, and that in the nonlinear regime, when pumping the system at 465 nm, 20^o incidence, and probing it at a time delay of 200 fs. (b) difference between the differential extinction pumping at 465 nm and pumping at 590 nm at 20^o incidence.

the system probed at 10^o incidence. The amplitude of the transient signal is dominated by the T-mode resonance and the high-energy hybrid mode at 590 nm, in particular at early times. The time evolution, from time zero where the system is farthest to the ground state, has been fitted with a linear combination of exponential functions. First of all we have followed the modulation of the T-mode, which is unaffected by the presence of the J-aggregate in the shell. The maximum absolute negative extinction modulation is -0.09, which corresponds to a relative extinction modulation of 10%. The dynamic at 530 nm can be fitted with a single exponential, with a time decay constant of 2.2 ps. At 590 nm, corresponding to the high energy hybrid mode, the maximum absolute modulation can be found and has a value of 0.11. The relative percentage extinction modulation is 15%. The dynamic of the optical extinction can be fitted with a single exponential, with a relaxation constant of 1.7 ps. Both values are in qualitative accordance with the dynamics recorded experimentally, with the faster dynamics of the hybrid mode presumably related to the nonlocal behavior of the hybrid metamaterial, but this cannot confirm the experimental data, at least not on the basis of this calculation, since the dynamics of the exciton, while interacting with a plasmonic system, is also known to demonstrate ultrafast dynamics.

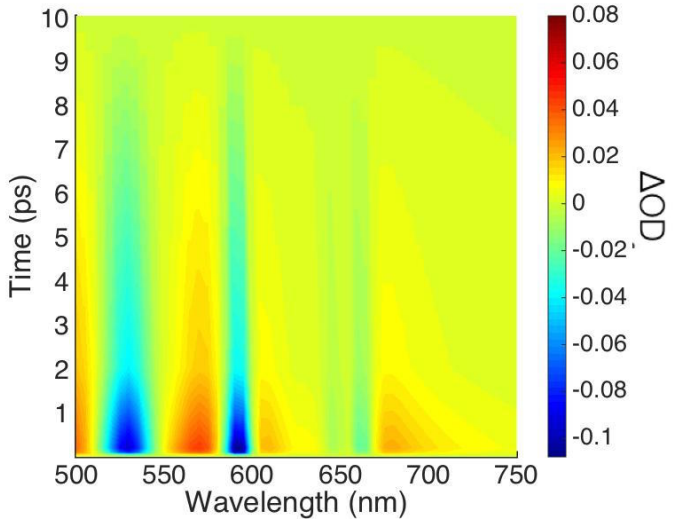

FIGURE 7.8: Pump probe calculation of the strong coupled nanorod/J-aggregate system pumped at 465 nm, 20^o incidence and probed at 10^o.

Figure 7.9 shows the dynamic evolution of the extinction modulation for a probe beam at 18^o incidence. The modulation is stronger than in the case of the probe beam at 10^o, and occurs mainly at 590 nm and 650 nm, corresponding to the modulation of the two hybrid modes.

The T-mode has a negative absolute modulation of -0.07, corresponding to a relative modulation of 8%. The time evolution can be well fitted by a linear combination of two exponentials, with time decay 0.8 ps and 1.4 ps, respectively. The absolute negative modulation of the two hybrid modes is -0.24, corresponding to a relative variation of 12%, for the high energy branch at 590 nm, and -0.28, corresponding to a relative variation of 20%, for the low energy branch at 650 nm. At 590 nm, a single decay constant can be extracted, equal to 1.3 ps. At 650 nm, a single time decay can be extracted, of 2.2 ps.

In the case of the probe at 18^o, we see a relative qualitative resemblance between the experimental pump-probe results and the numerical calculation, as can be seen in Figure 7.10. However, careful analysis of the transient calculations show that both hybrid modes experience a small red-shift upon optical coupling. This merely emphasizes that the coupling strength between exciton and plasmon have not been noticeably affected by the change in the permittivity of Au induced by the pump beam. This is in contrast with the experimental observations that

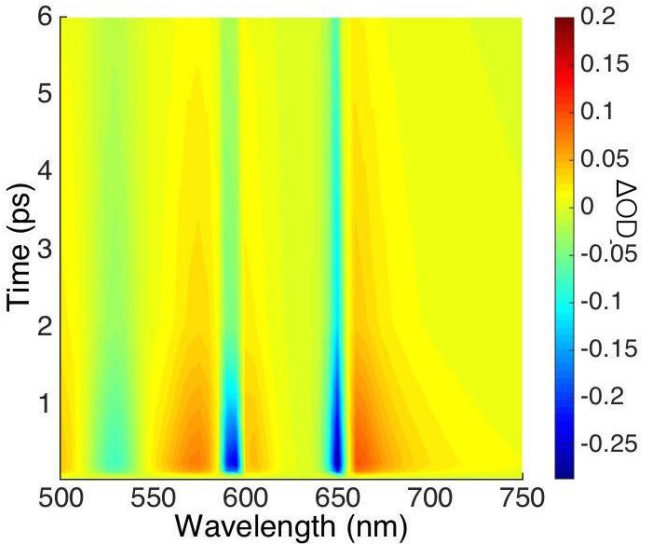

FIGURE 7.9: Pump probe calculation of the strong coupled nanorod/J-aggregate system pumped at 465 nm, 20^o incidence and probed at 18^o.

suggest that the main origin of the transient signal is in the modification of the exciton plasmon coupling strength as explained above.

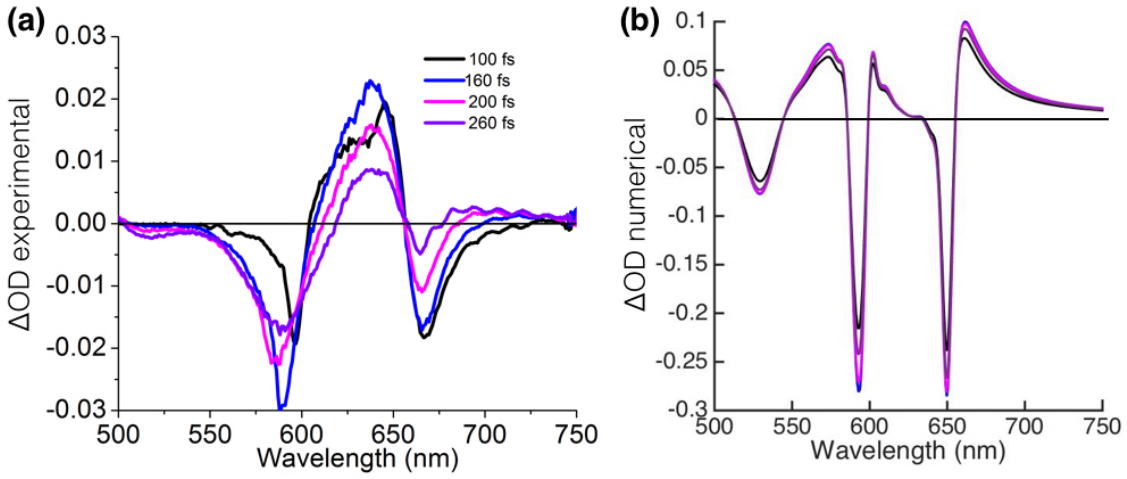

FIGURE 7.10: (a) shows the experimental measurements of the strong coupled hybrid system differential extinction when pumped at 465 nm, 20^o and probed at 18^o. (b) shows the correspondent numerical result.

Figure 7.11 shows the dynamic evolution of the differential optical extinction of the system pumped at 465 nm, 20^o incidence, and probed with TM polarized light at 20^o incidence. The main modulation feature correspond in this case to the low energy branch hybrid mode. The absolute modulation at 650 nm is negative,

and has an absolute value of 0.7, corresponding to a relative variation of 32%. The relaxation can be fitted with a single exponential, with decay constant of 2.2 ps.

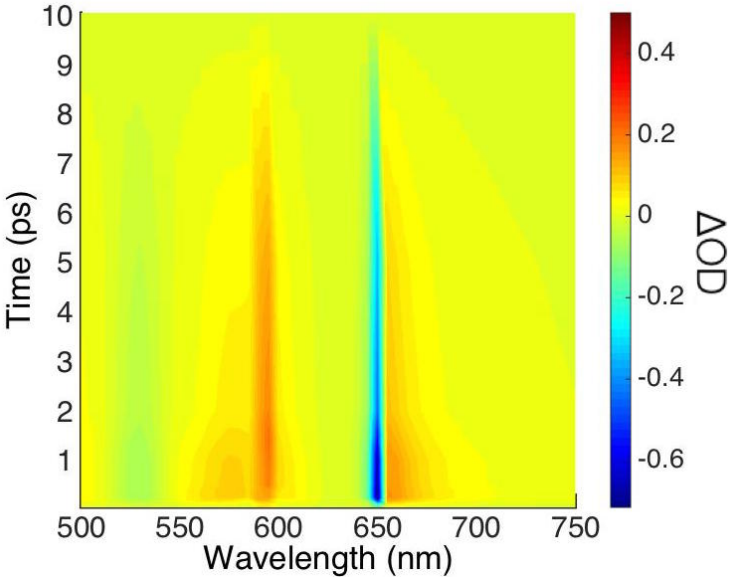

FIGURE 7.11: Pump probe calculation of the strong coupled nanorod/J-aggregate system pumped at 465 nm, 20^o incidence and probed at 20^o.

The modulation in the case of the pump centered at 590 nm, 20^o incidence and probed at 20^o, is similarly most sgnificant around the low energy hybrid mode. The low energy hibridized mode branch probes a negative modulation with absolute value of 0.7, and the dynamics can be fitted with a linear combination of two exponentials, with characteristic times of 1 and 1.2 ps. The characteristics of the nonlinear modulation at other angles of incidence are extremely similar to those obtaned using an exciting pulse centered at 465 nm and 20^o incidence, both in terms of amplitude and dynamic.

7.2.2 Nonlinear response of the coreshell naorod metamaterial: weak coupling regime

The nonlinear dynamic response of the weakly coupled system has been examined, pumping with a pulse centered at 465 nm, with an angle of incidence of 20^o. Since the transient response of the molecular aggregate is neglected in the model, the aim here is simply to examine the response of the plasmonic modes in the presence of the excitonic resonance and compare the transient contrast with

that obtained for the bare metamaterial in Chapter 6. Figure 7.12 (a) shows the dispersion of the differential extinction. The excitonic resonance is clearly visible as well at an energy of about 2.1 eV. Its transient signature, corresponding to an extinction loss at this frequency, is consistent with a partial destruction of nonlocality and a red-shift of the L-mode. The change in sign of the main transient extinction modulation is a direct result of the modulation of ohmic losses in the metal and a subsequent modulation in the nonlocal character of the optical response of the nanorod assembly as seen in Chapter 6 and experimentally in [87]. Also in the case of the weakly coupled system, the modulation amplitude obtained pumping in the interband region and pumping at 590 nm are similar. Figure 7.12 (b) shows the difference between the differential extinction in the two configurations, at a time delay corresponding to the maximum modulation.

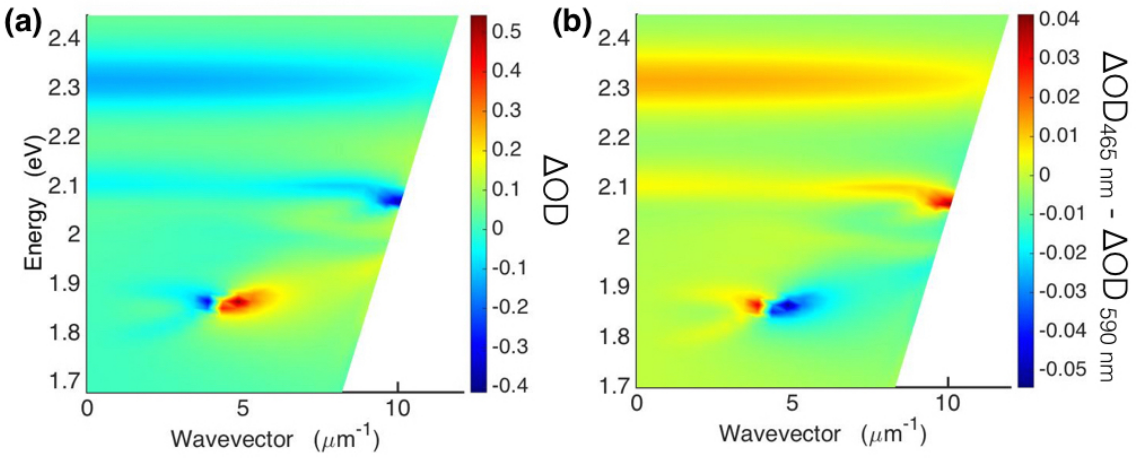

FIGURE 7.12: Pump probe dispersion calculation of the differential extinction of the weak coupled nanorod/J-aggregate system pumped at 465 nm, 20^o incidence in (a). Difference between the differential dispersion with the pump at 465 nm and the pump at 590 nm in (b), both at 20^o.

Figure 7.13 shows the dynamic of the extinction modulation of the system probed at 10^o. The strongest nonlinear modulation is obtained at 535 nm, corresponding to the region where the T-mode broadens and redshifts. The dynamic of the modulation can be fitted with one exponential function, with characteristic time of around 2 ps.

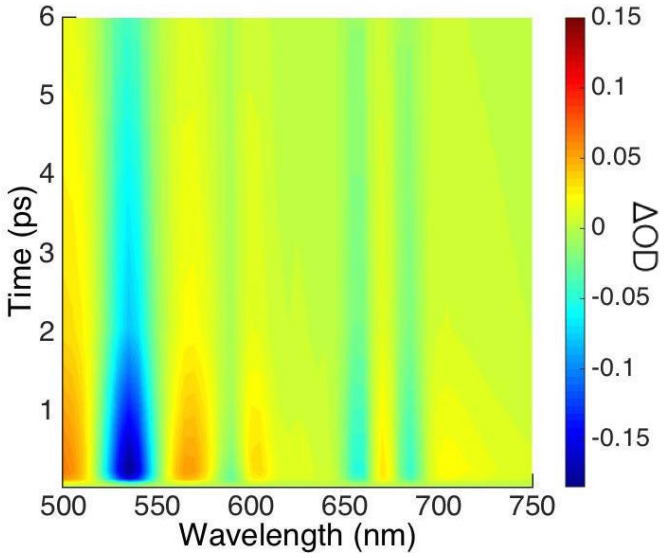

FIGURE 7.13: Pump probe calculation of the weak coupled nanorod/J-aggregate system pumped at 465 nm, 20^o incidence and probed at 10^o.

Figure 7.14 shows the dynamic of the extinction modulation of the system probed at 20^o. The modulation is strongest at 665 nm, corresponding to the L-mode, and has a value of 0.55. The relative percentage extinction modulation is in this case is 43%. The dynamic of the relaxation leads an effective characteristic time of 1.3 ps.

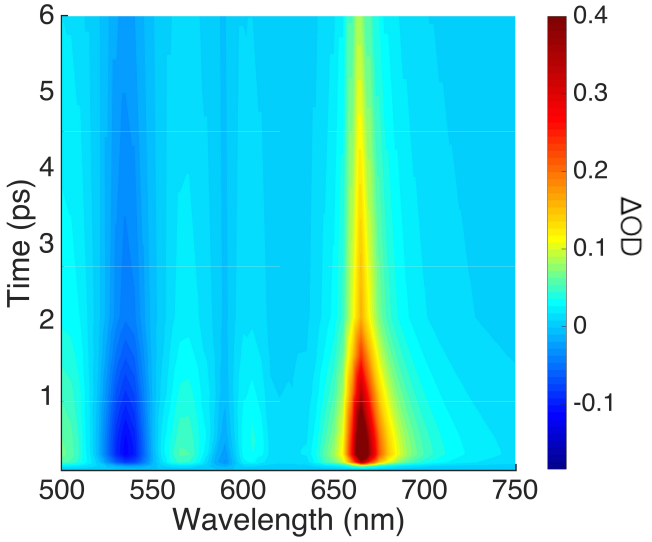

FIGURE 7.14: Pump probe calculation of the weak coupled nanorod/J-aggregate system pumped at 465 nm, 20^o incidence and probed at 20^o.

7.3 Summary

In this Chapter I have shown how the nanorod metamaterial can be coupled, thanks to its extremely flexible structure and spectral response, with an organic dye, a J-aggregate. The dye can be inserted in a void shell surrounding the gold nanorods.

The strength of the nanorod-dye coupling can be controlled, changing the thickness of the void shell. In Figure 7.5 and Figure 7.6 I have shown the variation of the linear modal response of the nanorod metamaterial due to the strong and weak coupling with the dye, respectively. I have chosen to use the L-mode of the system to perform the coupling. In the strong coupling regime, the modal structure of the metamaterial is radically changed, since the L-mode and the exciton transition hybridize and result in two new modes. These hybridized modes preserve the nonlocal character of the L-mode. The anticrossing shown in Figure 7.3 (c) is the signature of the occurrence of strong coupling, and the energy gap can be estimated in 0.15 eV. The anticrossing can be shown also with the Effective Medium approximation, as can be seen in Figure 7.4.

In the weak coupling regime, on the contrary, the L-mode and dispersionless excitonic resonance coexist without a significant interaction (other than a shift of the L-mode due to the change in the effective refractive index of the matrix).

When considering the nonlinear response of the system, the strong coupling is not destroyed. I have pumped the strong coupled system at two wavelengths, 465 nm, in the spectral region of strong interband absorption, and at 590 nm, corresponding to the high energy hybrid mode. As can be seen in Figure 7.5, the dynamic of the differential extinction is dominated by the two hybrid modes modulation. Also, the results for the two pump configurations is quite similar, both in terms of the amplitude of the modulation and the spectral shift of the modes. The abrupt sign change of the modulation as a function of the angle of incidence change is a result of the nonlocal behaviour of the hybrid modes. The most remarkable results obtained in terms of time performance correspond to the time constants extracted for the modulation of the hybrid modes. The effective time decay constant of the high energy mode is around 1.7 ps for the pump at

465 nm, 20^o incidence, probed at 10^o incidence. A strong dynamic response of the low energy mode, both in terms of the modulation (30%) and time decay constants, around 1 ps and 1.2 ps, is found for the pump at 465 nm, 20^o incidence, probed at 20^o incidence. A good qualitative correspondence between the numerical calculation and the experimental results has been observed.

Chapter 8

Conclusions and Outlook

In this thesis, the capabilities of a plasmonic metamaterial consisting of a regular array of gold nanorods to perform active, ultrafast modulation of an optical signal have been assessed theoretically and numerically. Two geometries have been considered: a metamaterial consisting of a square array of gold nanorods embedded in a Al_2O_5 (AAO) matrix and core-shell nanorod arrays, which enable to introduce functional molecules in the core or shell interacting with the gold nanorods. The third-order, Kerr-type nonlinear optical response of metamaterials in both geometries has been analysed and its ultrafast dynamic investigated.

A robust numerical model has been developed in order to simulate the linear optical response of the nanorod based plasmonic metamaterials, based on the Finite Element Method (FEM). Nonlocality has shown to allow the presence of hyperbolic modes of negative group velocity for frequencies above the effective local bulk plasma frequency. A subset of these modes have a waveguide character. The nonlocal Effective Medium Theory (EMT) developed in [57, 58] has shown to reproduce the numerical calculations in the limit of low losses in the gold. The local EMT analyzed in Chapter 2 has shown to reproduce the numerical calculations in the limit of high losses in the gold. The losses, and as a consequence the transition between the local and nonlocal regimes, can be reduced by increasing the mean free path of the electrons in the gold [60].

The dynamic, nonlinear response of the nanorod based metamaterials has

been modelled theoretically and numerically. A full vectorial analysis implementing the two-temperature model to monitor the evolution of electrons temperature in gold, has been developed. Previous experimental pump-probe results have been reproduced. The resonant modal response of the metamaterial has then been explored in order to both induce the nonlinear Kerr effect and to probe the optical nonlinear modulation. In the epsilon-near-zero regime, the metamaterial has shown numerically to induce an extinction modulation of 120%, with the recovery time as fast as 0.1 ps. It has been shown that the electromagnetic field spatial distribution at the wavelengths of control light is mapped into the resulting increased electrons temperature distribution of gold nanorods. Thus different resonant modes of the metamaterial will determine a precise spatial resolution of the electrons temperature profile. Since the electron heat capacity is temperature dependent, the presence of inhomogeneities in the electrons temperature distribution inside the gold nanorods determines different dynamics of the temperatures, depending on the location, due to the temperature rate modification at specific locations inside the nanorods. Adjusting the probe mode profile to spatially overlap the highest temperature gradients induced by control light, can effectively isolate only the fastest electrons temperature dynamics. These temperature inhomogeneities in nanorods have shown to enhance the nonlinear modulation by about 20% compared to the model with homogeneous electron temperature distribution inside the nanorods.

The linear optical response of a core-shell, J-aggregate-hybridized Au nanorod metamaterial has been analyzed numerically and analytically, with a local EMT modified in order to treat core-shell geometries. Two hybridization regimes have been identified, strong and weak coupling, between the molecular exciton and plasmonic modes. The strong coupling regime has shown to preserve the nonlocality of the bare nanorods system. The strongly coupled J-aggregate hybridized system has shown a picosecond time recovery when exploiting the high energy hybrid mode to mediate the nonlinear interaction and the low energy hybrid mode as a probe. Previous pump-probe experimental results on a J-aggregate hybridized nanorod metamaterial have been fairly reproduced, although the nonlinearity of

the J-aggregate has not been explicitly considered in the present analysis.

The core-shell EMT framework has been shown to capture the behaviour of various types of arrays of nanoparticles, core-shell spheroids and core-shell nanotubes, also for dimensions exceeding the quasistatic limit and showing a resonant response in the IR spectral region. In particular, the optical response of silicon-core/gold-shell spheroids shows a dispersionless resonance, visible also at normal incidence, able to confine the electromagnetic field in the core material. The spectral position of this resonance can be tuned by changing the ratio of the inner particle diameter to shell thickness. This resonance is present also in silicon-core/gold-shell nanotubes. The possibility of tayloring spectrally the optical response of the bare nanorod metamaterial towards the IR has also been investigated, theoretically, numerically and experimentally. High aspect ratio gold nanorods have been electrochemically deposited in an AAO matrix with small diameter, largely spaced pores. This porosity of the AAO matrix has been obtained by developing a solution containing selenic acid for the anodization [60].

8.1 Summary of the main achievements

- A comprehensive theoretical and numerical analysis of the linear and nonlinear response of nanorod and core-shell metamaterials has been performed and compared to experimental results in the visible and near-IR spectral ranges.

- A new family of hyperbolic waveguided modes above the effective plasma frequency, enabled by spatial dispersion, has been identified.

- The strong nonlinear response and the dynamic modulation capabilities associated with the excitation of the waveguideded modes of the metamaterial slab has been demonstrated.

- The presence of strong electron temperature gradients in the nanorods induced by a control light is shown to determine a stronger nonlinear modulation and to influence the dynamic response.

- The coherent interaction of molecular J-aggregates with core-shell nanorod arrays is analyzed in both the weak and strong coupling regimes.

- All-optically controlled coupling strength between exciton and plasmon modes in metamaterials has been demonstrated as a new approach to nonlinear metamaterials.

- Picosecond dynamics of the molecular excitons strongly coupled to plasmonic modes of the metamaterial has been identified and compared to the experimental results.

8.2 Future work

The established connection between the pump-induced temperature distribution and the spatial resolution of the probing beam in the nanorod/AAO metamaterial, can be used to design a metamaterial with optimized modulation efficiency. From a theoretical point of view, the immediate step forward would be that of developing a systematic mathematical method to estimate the efficiency of the different pump-probe configurations. Future developments to this work will certainly include the experimental characterization of such optimized structures. The importance of nonlocality in the remarkable nonlinear extinction modulation amplitude obtained in the simulations will need to be further examined. The dynamic, nonlinear performance of a nanorod metamaterial with the same geometrical parameters but higher and lower losses will have to be analyzed, to understand contribution of various nonlocal modes. Also, the dependence of the nonlinear modulation on the power of the incident pump beam will have to be considered extensively, as the dynamic response depends on the energy absorbed.

The optimization of the field profile of the silicon core, gold shell spheroids and nanotubes could be further exploited to induce nonlinear effects in silicon with very low operating power. Future work on these structures will include their linear and nonlinear experimental characterization. The theoretical and numerical modelling of the core-shell, J-aggregate-hybridized nanorod metamaterial can be developed by including the nonlinearity of the organic dye, and by considering the energy

exchange between the plasmonic resonance and the excitonic transition during the excitation. This would require ab initio simulations of the dye dynamics. A phenomenological model that considers broadening and blueshift of the exciton absorption resonance could be initially implemented. The increased damping and blueshift of the excitonic transition may further describe subtle features of the experimental results that show a decrease of the energy gap in the dynamic strong coupling spectra.

From a practical point of view, the integration of metamaterials in silicon photonic circuitry and/or in individual photonic circuit components, as well as optical fibers, will lead to new photonic devices with the enhanced nonlinear and dispersion management functionalities.

List of Publications

- S. Peruch, J. S. Bouillard, D. O'Connor, W. Dickson, G. A. Wurtz, G. Larrieu, X. Han, T. Akalin and A. V. Zayats, "Silicon core, gold coated nanorod metamaterials, modeling and experiment", Poster presentation in Near-field Optics, Nanophotonics and Related Techniques (NFO), Donostia, San Sebastian, 3-6 September 2012.

- S. Peruch, J. S. Bouillard, D. O'Connor, W. Dickson, G. A. Wurtz, G. Larrieu, X. Han, T. Akalin and A. V. Zayats, "Silicon core, gold coated nanorod metamaterials, modeling and experiment", Poster presentation in Lasers and Electro-Optics Europe and International Quantum Electronics Conference (CLEO EUROPE/IQEC), Munich, 12-16 May 2013.

- A. Neira, S. Peruch, M. Nasir, N. Olivier, W. Dickson, G. Wurtz and A. V. Zayats, "Third-order nonlinearity of plasmonic hyperbolic metamaterials: numerical design", Poster presentation in Faraday Discussions on Nanoplasmonics, London, 12-16 February 2015.

- S. Peruch, A. Neira, G. Wurtz and A. V. Zayats, "Ultrafast nanorod plasmonic metamaterials: elliptic, hyperbolic and epsilon near zero regimes", Oral presentation in Lasers and Electro-Optics Europe and International Quantum Electronics Conference (CLEO EUROPE/IQEC), Munich, 20-25 June 2015.

- S. Peruch, A. Neira, G. Wurtz and A. V. Zayats, "Ultrafast nanorod plasmonic metamaterials: elliptic, hyperbolic and epsilon near zero regimes",Oral prsentation in Progress In Electromagnetics Research Symposium (PIERS), Prague, 6-9 July 2015.

- M. E. Nasir, S. Peruch, N. Vasilantonakis, W. P. Wardley, W. Dickson, G. A. Wurtz, and A. V. Zayats, "Tuning the effective plasma frequency of nanorod metamaterials from visible to telecom wavelengths", *Applied Physics Letters*, 107(12), 2015 http://dx.doi.org/10.1063/1.4931687 .

- S. Peruch, A. Neira, G. A. Wurtz and A. V. Zayats, "Ultrafast nanorod plasmonic metamaterials: elliptic, hyperbolic and epsilon near zero regimes", *Optics Express*, manuscript in preparation.

- S. Peruch, A. Neira, G. A. Wurtz and A. V. Zayats, "Ultrafast dynamics of weak and strong exciton-plasmon coupling in hybrid nanorod metamaterials", manuscript in preparation.

Bibliography

[1] R. Paschotta. Field guide to optical fiber technology. In *Oxford Handbook of Innovation*. SPIE press; Spie edition, P. O. Box 10, Bellingham, Washington 98227-0010 USA, 2010.

[2] D. Colladon. Sur les réflexions d'un rayon de lumière à l'intérieur d'une veine liquide parabolique. *Comptes Rendus*, 15, October 1842.

[3] N. S. Kapani H. H. Hopkins. A flexible fiberscope using static scanning. *Nature*, 173(173):39–41, January 1954.

[4] J. Hecht. Overview of optical networking. *MIT technology review*, January 2002. URL `http://www.technologyreview.com/news/401339/overview-of-optical-networking/`.

[5] F. Poletti, N. V. Wheeler, M. N. Petrovich, N. Baddela, E. Numkam Fokoua, J. R. Hayes, D. R. Gray, Z. Li, R. Slavik, and D. J. Richardson. Towards high-capacity fiber-optic communications at the speed of light in vacuum. *Nature Photonics*, 7(1):279–284, March 2013. doi: doi:10.1038/nphoton.2013.45.

[6] E. Ozbay. Plasmonics: Merging photonics and electronics at nanoscale dimensions. *Science*, 311(5758):189–193, 2006. doi: 10.1126/science.1114849.

[7] E.D. Palik. *Handbook of Optical Constants of Solids*. Number v. 3 in Academic Press handbook series. Academic Press, 1998. ISBN 9780125444231.

[8] J. M. Shainline, J. S. Orcutt, M. T. Wade, K. Nammari, B. Moss, M. Georgas, C. Sun, R. J. Ram, V. Stojanović, and M. A. Popocić. Depletion-mode

carrier-plasma optical modulator in zero-change advanced cmos. *Optics Letters*, 38:2657–2663, August 2013. doi: 10.1364/OL.38.002657.

[9] C. Vu. Made in ibm labs: Holey optochip first to transfer one trillion bits of information per second using the power of light. *IBM press release*, March 2012. URL `http://www-03.ibm.com/press/us/en/pressrelease/37095.wss`.

[10] T. Simonite. Intel's laser chips could make data centers run better. *MIT technology review*, September 2013. URL `http://www.technologyreview.com/news/518941/intels-laser-chips-could-make-data-centers-run-better/`.

[11] G. E. Moore. Cramming more components onto integrated circuits. *Proceedings of the IEEE*, 86(1):82–85, Jan 1998. doi: 10.1109/JPROC.1998.658762.

[12] S. Kodama, T. Yoshimatsu, and H. Ito. 500 gbit/s optical gate monolithically integrating photodiode and electroabsorption modulator. *Electronics Letters*, 40(9):555–556, April 2004. doi: 10.1049/el:20040391.

[13] R.W. Boyd. *Nonlinear Optics*. Nonlinear Optics Series. Elsevier Science, 2008. ISBN 9780080485966.

[14] W. Park. Optical interactions in plasmonic nanostructures. *Nano Convergence*, 1(1):2196–2198, April 2014. doi: 10.1186/s40580-014-0002-x.

[15] S.A. Maier. *Plasmonics: Fundamentals and Applications*. Springer US, 2010. ISBN 9781441941138.

[16] H. Raether. *Surface plasmons on smooth and rough surfaces and on gratings*. Springer tracts in modern physics. Springer, 1988. ISBN 9783540173632.

[17] C. K. Sun, F. Vallée, L. H. Acioli, E. P. Ippen, and J. G. Fujimoto. Femtosecond-tunable measurement of electron thermalization in gold. *Physical Review B*, 50:15337–15348, November 1994. doi: 10.1103/PhysRevB.50.15337.

[18] N. Del Fatti, R. Bouffanais, F. Vallée, and C. Flytzanis. Nonequilibrium electron interactions in metal films. *Phys. Rev. Lett.*, 81:922–925, July 1998. doi: 10.1103/PhysRevLett.81.922.

[19] C. F. Bohren and D. R. Huffman. *Absorption and scattering of light by small particles*. Wiley science paperback series. Wiley, 1983. ISBN 9780471293408.

[20] J.D. Jackson. *Classical electrodynamics*. Wiley, 1975. ISBN 9780471431329.

[21] W. Cai and V. Shalaev. *Optical Metamaterials*. Springer, 2010. ISBN 978-1-4419-1150-6.

[22] W. E. Kock. Metallic delay lenses. *The Bell System Technical Journal*, 27 (1):58–82, January 1948. doi: 10.1002/j.1538-7305.1948.tb01331.x.

[23] V. Veselago. The electrodynamics with simultaneously negative values of ϵ and μ. *Soviet physics uspekhi*, 10(4):509–514, January-February 1968.

[24] J. B. Pendry. Negative refraction makes a perfect lens. *Physical review letters*, 85(18):3966–3969, October 2000. doi: 10.1103/PhysRevLett.85.3966.

[25] R. A. Shelby, D.R. Smith, and S. Schultz. Experimental verification of a negative index of refraction. *Science*, 292(5514):77–79, April 2001. doi: 10.1126/science.1058847.

[26] F. Ye, J. M. Merlo, M. J. Burns, and M. J. Naughton. Optical and electrical mappings of surface plasmon cavity modes. *Nanophotonics*, 3, 2014. doi: 10.1515/nanoph-2013-0038,. URL `http://nanoph.2014.3.issue-1-2/nanoph-2013-0038/nanoph-2013-0038.xml1`.

[27] G. Mie. Beträge zur optik trüber medien, speziell kolloidaler metallösungen. *Analer der Physik*, 330(3):377–445, March 1908. doi: 10.1002/andp.19083300302.

[28] P. B. Johnson and R. W. Christy. Optical constants of the noble metals. *Physical Review B*, 6(12):4370–4379, December 1972. doi: 10.1103/PhysRevB.6.4370.

[29] Guided plasmonic modes in nanorod assemblies: strong electromagnetic coupling regime. Guided plasmonic modes in nanorod assemblies: strong electromagnetic coupling regime. *Optics Express*, 16:7460–7470, 2008. doi: 10.1364/OE.16.007460.

[30] J. Elser, R. Wangberg, V. A. Poldolskiy, and E. E. Narimanov. Nanowire metamaterials with extreme optical anisotropy. *Applied Physics Letters*, 89 (26), January 2006. doi: http://dx.doi.org/10.1063/1.2422893.

[31] W. Knoll. Interfaces and film thickness as seen by electromagnetic waves. *Annual Review of Physical Chemistry*, 49:Annual Review of Physical Chemistry, 1998. doi: 10.1146/annurev.physchem.49.1.569.

[32] S. Ekgasit, C. Thammacharoen, and W. Knoll. Surface plasmon resonance spectroscopy based on evanescent field treatment. *Analytical Chemistry*, 76: 561–568, 2004. doi: 10.1021/ac035042v.

[33] P. Berini. Plasmon-polariton waves guided by thin lossy metal films of finite width: Bound modes of symmetric structures. *Physical Review B*, 61:10484–10503, 2000. doi: 10.1103/PhysRevB.61.10484.

[34] J. A. Fleck Jr. and M. D. Feit. Beam propagation in uniaxial anisotropic media. *Journal of the American Optical Society*, 73(7), 1983. doi: 10.1364/JOSA.73.000920.

[35] N. Vasilantonakis, M. E. Nasir, W. Dickson, G. A. Wurtz, and A. V. Zayats. Bulk plasmon-polaritons in hyperbolic nanorod metamaterial waveguides. *Laser and Photonics Reviews*, 9(3):345–353, 2015. doi: 10.1002/lpor.20140045.

[36] L.A. Falkovsky and E.G. Mishchenko. Electron-lattice kinetics of metals heated by ultrashort laser pulses. *Journal of Experimental and Theoretical Physics*, 88(1):84–88, 1999. doi: 10.1134/1.558768.

[37] C. Kittel. *Introduction to Solid State Physics*. Wiley, 2004. ISBN 9780471415268.

[38] L. Jiang and H.L. Tsai. Energy transport and material removal in wide bandgap materials by a femtosecond laser pulse. *Journal of Experimental and Theoretical Physics*, 48(3-4):487–499, 2005. doi: http://dx.doi.org/10.1016/j.ijheatmasstransfer.2004.09.016.

[39] J. K. Chen, W. P. Latham, and J. E. Beraun. Axisymmetric modeling of femtosecond-pulse laser heating on metal films. *Numerical Heat Transfer, Part B: Fundamentals*, 42(1):1–17, 2002. doi: 10.1080/10407790190053806. URL `http://dx.doi.org/10.1080/10407790190053806`.

[40] W. M.G. Ibrahim, H. E. Elsayed-Ali, C. E. Bonner Jr., and M. Shinn. Ultrafast investigation of electron dynamics in multi-layer metals. *Numerical Heat Transfer, Part B: Fundamentals*, 47(10-11):2261–2268, 2004. doi: 10.1016/j.ijheatmasstransfer.2003.11.029.

[41] R. W. Boyd, Z. Shi, and I. De Leon. The third-order nonlinear optical susceptibility of gold. *Optics Communications*, 326(7), 2014. doi: 10.1016/j.optcom.2014.03.005.

[42] S. J. Youn, T. H. Rho, B. I. Min, and K. S. Kim. Extended drude model analysis of noble metals. *Physica status solidi*, 244(4), 2007. doi: 10.1002/pssb.200642097.

[43] J. A. McKay and J. A. Rayne. Temperature dependence of the infrared absorptivity of the noble metals. *Physical Review B*, 13, 1976. doi: 10.1103/PhysRevB.13.673.

[44] T. Holstein. Optical and infrared volume absorptivity of metals. *Physical Review*, 96, 1954. doi: 10.1103/PhysRev.96.535.

[45] R. T. Beach and R. W. Christy. Electron-electron scattering in the intraband optical conductivity of cu, ag, and au. *Phys. Rev. B*, 16, 1977. doi: 10.1103/PhysRevB.16.5277.

[46] G. R. Parkins, W. E. Lawrence, and R. W. Christy. Intraband optical conductivity $\sigma(\omega, t)$ of cu, ag, and au: Contribution from electron-electron scattering. *Phys. Rev. B*, 23, 1981. doi: 10.1103/PhysRevB.23.6408. URL `http://link.aps.org/doi/10.1103/PhysRevB.23.6408`.

[47] J.K. Chen, D.Y. Tzou, and J.E. Beraun. A semiclassical two-temperature model for ultrafast laser heating. *International Journal of Heat and Mass Transfer*, 49:307–316, 2006. doi: 10.1016/j.ijheatmasstransfer.2005.06.022.

[48] J. K. Chen and J. E. Beraun. Numerical study of ultrashort laser pulse interactions with metal films. *Numerical Heat Transfer, Part A: Applications*, 40:1–20, 2001. doi: 10.1080/104077801300348842.

[49] S. I. Anisimov, B. L. Kapeliovich, and T. L. Perelman. Electron emission from metal surfaces exposed to ultrashort laser pulses. *Zhurnal Eksperimentalnoi i Teoreticheskoi Fiziki*, 66:776–781, 1974. URL `http://adsabs.harvard.edu/abs/1974ZhETF..66..776A`.

[50] T. Q. Qiu and C. L. Tien. Heat transfer mechanisms during short-pulse laser heating of metals. *Journal of Heat Transferi*, 115(4):835–841, 1993. doi: doi:10.1115/1.2911377.

[51] S. R. Vatsya and K. S. Virk. Solution of two-temperature thermal diffusion model of laser–metal interactions. *Journal of Laser Applications*, 15(4):273–278, 2003. doi: http://dx.doi.org/10.2351/1.1619998.

[52] L. Jiang and H. Tsai. Improved two-temperature model and its application in ultrashort laser heating of metal films. *Journal of Heater Transfer*, 127: 1167–1173, 2005. doi: 10.1115/1.2035113.

[53] J. Y. Bigot, J.Y. Merle, O. Cregut, and A. Daunois. Electron dynamics in copper metallic nanoparticles probed with femtosecond optical pulses. *Physical Review Letters*, 75:4702–4705, 1995. doi: 10.1103/PhysRevLett.75.4702.

[54] J. B. Lee, K. Kang, and S. H. Lee. Comparison of theoretical models of electron-phonon coupling in thin gold films irradiated by femtosecond pulse lasers. *Materials Transactions, JIM*, 52:547–553, 2011. doi: 10.2320/matertrans.M2010396.

[55] R. J. Pollard, A. Murphy, W. R. Hendren, P. R. Evans, R. Atkinson, G. A. Wurtz, A. V. Zayats, and V. A. Podolskiy. Optical nonlocalities and additional waves in epsilon-near-zero metamaterials. *Physical Review Letters*, 102:127405–127409, March 2009. doi: 10.1103/PhysRevLett.102.127405.

[56] T. Simonite. Comsol Multiphysics 4.2 Release notes. 2011. URL `http://www.comsol.com/support/releasenotes/4.2/`.

[57] J. Elser J., V. A. Podolskiy, I. Salakhutdinov, and I. Avrutsky. Nonlocal effects in effective medium response of nanolayered metamaterials. *Applied Physics Letters*, 90(19):350–354, 2007. doi: 10.1063/1.2737935.

[58] Wells B. M., Zayats A. V., and Podolskiy V. A. Nonlocal optics of plasmonic nanowire metamaterials. *Physical Review B*, 89:035111–035121, 2014. doi: 10.1103/PhysRevB.89.035111.

[59] K-T. Tsai, G. A. Wurtz, J-Y. Chu, H-H. Wang, A. V. Krasavin, J-H. He, M. Wells, V. A. Podolskiy, J-K. Wang, Y-L. Wang, and A. V. Zayats. Looking into meta-atoms of plasmonic nanowire metamaterial. *Nano Letters*, 14, 2014. doi: 10.1021/nl501283c. URL `http://dx.doi.org/10.1063/1.3642981`.

[60] M. E. Nasir, S. Peruch, N. Vasilantonakis, W. P. Wardley, W. Dickson, G. A. Wurtz, and A. V. Zayats. Tuning the effective plasma frequency of nanorod metamaterials from visible to telecom wavelengths. *Applied Physics Letters*, 107, 2015. doi: 10.1063/1.4931687.

[61] S. Ross. Plasmonics in the mid-infrared. *Nature Photonics*, 6(7):409–411, July 2012. doi: doi:10.1038/nphoton.2012.161.

[62] W. Suetaka. *Surface Infrared and Raman Spectroscopy*. Number v. 111 in Springer tracts in modern physics. Springer, 1988. ISBN 9783540173632.

[63] J. V. Coe, K. R. Rodriguez, S. Teeters-Kennedy, K. Cilwa, J. Heer, H. Tian, and S. M. Williams. Metal films with arrays of tiny holes: Spectroscopy with infrared plasmonic scaffolding. *The Journal of Physical Chemistry C*, 111(47):17459–17472, 2007. doi: 10.1021/jp072909a.

[64] K. R. Rodriguez, S. Shah, S. M. Williams, S. Teeters-Kennedy, and J. V. Coe. Enhanced infrared absorption spectra of self-assembled alkanethiol monolayers using the extraordinary infrared transmission of metallic arrays of subwavelength apertures. *The Journal of Chemical Physics*, 121(18):8671–8675, 2004. doi: http://dx.doi.org/10.1063/1.1814052.

[65] S. M. Teeters-Kennedy, K. R. Rodriguez, T. M. Rogers, K. A. Zomchek, S. M. Williams, A. Sudnitsyn, L. Carter, V. Cherezov, M. Caffrey, and J. V. Coe. Controlling the passage of light through metal microchannels by nanocoatings of phospholipids. *The Journal of Physical Chemistry B*, 110 (43):21719–21727, 2006. doi: 10.1021/jp062201g.

[66] S. M. Williams, K. R. Rodriguez, S. Teeters-Kennedy, A. D. Stafford, S. R. Bishop, U. K. Lincoln, and J. V. Coe. Use of the extraordinary infrared transmission of metallic subwavelength arrays to study the catalyzed reaction of methanol to formaldehyde on copper oxide. *The Journal of Physical Chemistry B*, 108(31):11833–11837, 2004. doi: 10.1021/jp0489368.

[67] T. Ishi, J. Fujikata, K. Makita, T. Baba, and K. Ohashi. Si nano-photodiode with a surface plasmon antenna. *Japanese Journal of Applied Physics*, 44 (3):364–368, 2005. doi: 10.1143/JJAP.44.L364.

[68] S. R. J. Brueck, V. Diadiuk, T. Jones, and W. Lenth. Enhanced quantum efficiency internal photoemission detectors by grating coupling to surface plasma waves. *Applied Physics Letters*, 46(10):915–917, 1985. doi: http://dx.doi.org/10.1063/1.95819.

[69] P. Bouchon, F. Pardo, B. Portier, L. Ferlazzo, P. Ghenuche, G. Dagher, C. Dupuis, N. Bardou, R. Haïdar, and J. L. Pelouard. Total funneling of light in high aspect ratio plasmonic nanoresonators. *Applied Physics Letters*, 98(19), 2011. doi: http://dx.doi.org/10.1063/1.3588393.

[70] K. Swaminathan, T. J. Grassmann, L.-M. Yang, Q. Gu, M. J. Mills, and S. A. Ringel. Optically-aligned visible/near-infrared dual-band photodetector materials and devices on gaas using metamorphic epitaxy. *J. Appl. Phys*, 110, 2011. doi: 10.1063/1.364298. URL `http://dx.doi.org/10.1063/1.3642981`.

[71] C. M. Soukoulis and M. Wegener. Past achievements and future challenges in the development of three-dimensional photonic metamaterials. *Nature Photonics*, 5(9):3532–3537, 2011. doi: 10.1038/nphoton.2011.154.

[72] S. P. Burgos, R. de Waele, A. Polman, and H. A. Atwater. A single-layer wide-angle negative-index metamaterial at visible frequencies. *Nature Material*, 9(5):407–412, 2010. doi: 10.1038/nmat2747. URL `http://dx.doi.org/10.1038/nmat2747`.

[73] C. García-Meca, J. Hurtado, J. Martí, A. Martínez, W. Dickson, and A. V. Zayats. Low-loss multilayered metamaterial exhibiting a negative index of refraction at visible wavelengths. *Physical Review Letters*, 106:067402–067406, 2011. doi: 10.1103/PhysRevLett.106.067402.

[74] A. V. Kabashin, P. Evans, S. Pastkovsky, W. Hendren, G. A. Wurtz, R. Atkinson, R. Pollard, V. A. Podolskiy, and A. V. Zayats. Plasmonic nanorod metamaterials for biosensing. *Nature Materials*, 8(11):867–871, november 2009. doi: http://dx.doi.org/10.1063/1.3588393.

[75] P. R. Evans, G. A. Wurtz, R. Atkinson, W. Hendren, D. O'Connor, W. Dickson, R. J. Pollard, and A. V. Zayats. Plasmonic core/shell nanorod arrays: Subattoliter controlled geometry and tunable optical properties. *Journal of Physical Chemistry C*, 111(11):12522–12527, july 2007. doi: 10.1021/jp0718348.

[76] M. E. Nasir, W. Dickson, G. A. Wurtz, W. P. Wardley, and A. V. Zayats. Hydrogen detected by the naked eye: Optical hydrogen gas sensors based on core/shell plasmonic nanorod metamaterials. *Advanced Materials*, 26(21): 3532–3537, 2014. doi: 10.1002/adma.201305958.

[77] J. P. O'Sullivan and G. C. Wood. The morphology and mechanism of formation of porous anodic films on aluminium. *Proceedings of the Royal Society of London A: Mathematical, Physical and Engineering Sciences*, 317(1531): 511–543, 1970. doi: 10.1098/rspa.1970.0129.

[78] K. Nielsch, J. Choi, K. Schwirn, R. B. Wehrspohn, and U. Gosele. Self-ordering regimes of porous alumina: The 10 porosity rule. *Nano Letters*, 2 (7):677–680, 2002. doi: 10.1021/nl025537k.

[79] J. Martín, C. V. Manzano, O. Caballero-Calero, and M. Martín-González. High-aspect-ratio and highly ordered 15-nm porous alumina templates. *ACS Applied Materials & Interfaces*, 5(1):72–79, 2013. doi: 10.1021/am3020718.

[80] W. Lee, R. Ji, U. Gosele, and K. Nielsch. Fast fabrication of long-range ordered porous alumina membranes by hard anodization. *Nature Material*, 5(9):1476–1122, 2006. doi: 10.1038/nmat1717.

[81] J. McPhillips, A. Murphy, M. P. Jonsson, W. R. Hendren, R. Atkinson, F. Höök, A. V. Zayats, and R. J. Pollard. High-performance biosensing using arrays of plasmonic nanotubes. *ACS Nano*, 4:2210–2216, 2010. doi: 2210-2216.

[82] M. Kauranen and A. V. Zayats. Nonlinear plasmonics. *Nature Photonics*, 6 (11):737–748, November 2012. doi: 10.1038/nphoton.2012.244.

[83] K. F. MacDonald, Z. L. Samson, M. I. Stockman, and N. I. Zheludev. Ultrafast active plasmonics. *Nature Photonics*, 3:55–58, 2009. doi: 10.1038/nphoton.2008.249.

[84] N. Rotenberg, J. N. Caspers, and H. N. van Driel. Tunable ultrafast control of plasmonic coupling to gold films. *Physical Review B*, 80:245420–245428, 2009. doi: 10.1103/PhysRevB.80.245420.

[85] M. Ren, B. Jia, J. Ou, E. Plum, J. Zhang, K. F. MacDonald, A. E. Nikolaenko, J. Xu, M. Gu, and N. I. Zheludev. Tunable ultrafast control of plasmonic coupling to gold films. *Advanced Materials*, 23:5540–5544, 2011. doi: 10.1002/adma.201103162.

[86] P. Ginzburg, F. J. Rodríguez Fortu no, G. A. Wurtz, W. Dickson, A. Murphy, F. Morgan, R. J. Pollard, I. Iorsh, A. Atrashchenko, P. A. Belov, Y. S. Kivshar, A. Nevet, G. Ankonina, M. Orenstein, and A. V. Zayats. Manipulating polarization of light with ultrathin epsilon-near-zero metamaterials. *Optics Express*, 21:14907–14917, 2013. doi: 10.1364/OE.21.014907.

[87] G. A. Wurtz, R. J. Pollard, W. R. Hendren, G. P. Wiederrecht, D. J. Gosztola, V. A. Podolskiy, and A. V. Zayats. Designed ultrafast optical nonlinearity in a plasmonic nanorod metamaterial enhanced by nonlocality. *Nature Nanotechnology*, 6(6):107–111, Febuary 2011. doi: 10.1038/nnano.2010.278.

[88] A. D. Neira, G. A. Wurtz, P. Ginzburg, and A. V. Zayats. Ultrafast all-optical modulation with hyperbolic metamaterial integrated in si photonic circuitry. *Optics Express*, 22:10987–10994, 2014. doi: 10.1364/OE.22.010987.

[89] A. Barbosa, G. A. Wurtz, and A. V. Zayats. Signal modulation. *UK Patent Application No. 1400398.2*, 2014.

[90] A. Barbosa, G. A. Wurtz, and A. V. Zayats. Enz modulator. *UK Patent Application No. 1412388.9*, 2014.

[91] D. Pacifici, H. J. Lezec, and H. A. Atwater. All-optical modulation by plasmonic excitation of cdse quantum dots. *Nature Photonics*, 1:402–406, 2013. doi: 10.1038/nphoton.2007.95.

[92] D. Traviss, R. Bruck, B. Mills, M. Abb, and O. L. Muskens. Ultrafast plasmonics using transparent conductive oxide hybrids in the epsilon-near-zero regime. *Applied Physics Letters*, 102:121112–1–4, 2013. doi: http://dx.doi.org/10.1063/1.4798833.

[93] M. Abb, P. Albella, J. Aizpurua, , and O. L. Muskens. All-optical control of a single plasmonic nanoantenna–ito hybrid. *Nano Letters*, 11:2457–2463, 2011. doi: 10.1021/nl200901w.

[94] D. J. Cho, W. Wu, E. Ponizovskaya, P. Chaturvedi, A. M. Bratkovsky, S. Wang, X. Zhang, F. Wang, and Y. R. Shen. Ultrafast modulation of optical metamaterials. *Optics express*, 17:1762–17657, 2009. doi: 10.1364/OE.17.017652.

[95] A. E. Nikolaenko, N. Papasimakis, A. Chipouline, F. De Angelis, E. Di Fabrizi, and N. I. Zheludev. Thz bandwidth optical switching with carbon nanotube metamaterial. *Optics express*, 20:6068–6079, 2012. doi: 10.1364/OE.20.006068.

[96] C. Argyropoulos, F. Monticone, N. M. Estakhri, and A. Alu. Plasmonic and hyperbolic metamaterials based on enhanced nonlinear response. *International Journal of Antennas and Propagation*, 2014, 2014. doi: 10.1155/2014/532634.

[97] G. A. Wurtz, P. R. Evans, W. Hendren, R. Atkinson, W. Dickson, R. J. Pollard, A. V. Zayats, W. Harrison, and C. Bower. Molecular plasmonics with tunable exciton plasmon coupling strength in j aggregate hybridized au nanorod assemblies. *Nano Letters*, 7, 2007. doi: 10.1021/nl070284m.

[98] D. G. Lidsey, D. Bradley, A. Armitage, S. Walker, and M. S. Skolnick. Photon-mediated hybridization of frenkel excitons in organic semiconductor microcavities. *Science*, 5741(288):1620–1623, June 2000. doi: 10.1126/science.288.5471.1620.

[99] P. A. Hobson, W. L. Barnes, D. G. Lidzey, G. A. Gehring, D. M. Whittaker, M. S. Skolnick, and S. Walker. Strong exciton–photon coupling in a low-q all-metal mirror microcavity. *Applied Physics Letters*, 81(19):3519–3521, 2002. doi: http://dx.doi.org/10.1063/1.1517714.

[100] A. Christ, S. G. Tikhodeev, N. A. Gippius, J. Kuhl, and H. Giessen. Waveguide-plasmon polaritons: Strong coupling of photonic and electronic resonances in a metallic photonic crystal slab. *Physical Review Letters*, 91: 183901–183905, October 2003. doi: 10.1103/PhysRevLett.91.183901.

[101] G. P. Wiederrecht, G. A. Wurtz, , and J. Hranisavljevic. Coherent coupling of molecular excitons to electronic polarizations of noble metal nanoparticles. *Nano Letters*, 4(11):2121–2125, 2004. doi: 10.1021/nl0488228.

[102] J. Bellessa, C. Bonnand, J. C. Plenet, and J. Mugnier. Strong coupling between surface plasmons and excitons in an organic semiconductor. *Physical Review Letters*, 93:036404–036408, July 2004. doi: 10.1103/PhysRevLett.93.036404.

[103] J. Dintinger, S. Klein, F. Bustos, W. L. Barnes, and T. W. Ebbesen. Strong coupling between surface plasmon-polaritons and organic molecules in sub-wavelength hole arrays. *Physical Review B*, 71:035424–035429, January 2005. doi: 10.1103/PhysRevB.71.035424.

[104] Y. Sugawara, T. A. Kelf, J. J. Baumberg, M. E. Abdelsalam, and P. N. Bartlett. Strong coupling between localized plasmons and organic excitons in metal nanovoids. *Physical Review Letters*, 97:266808–266812, December 2006. doi: 10.1103/PhysRevLett.97.266808.

[105] T. Kobayashi. *J-Aggregates*. World Scientific, 1996. ISBN 981-02-2737-X.

[106] E. E. Jelley. Spectral absorption and fluorescence of dyes in the molecular state. *Nature*, 138, 1936. doi: 10.1038/1381009a0.

[107] S. Sakin, A. Eisfield, S. Valleau, and A. Aspuru-Guzik. Photonics meets excitonics: Natural and artificial molecular aggregates. *Nanophotonics*, 2, 2013. doi: 10.1515/nanoph-2012-0025.

[108] D. A. Higgins, P. J. Reid, and P. F. Barbara. Structure and exciton dynamics in j aggregates studied by polarization-dependent near-field scanning optical microscopy. *The Journal of Physical Chemistry*, 100, 1996. doi: 10.1021/jp9518217.

[109] J. Hranisavljevic, N. M. Dimitrijevic, G. A. Wurtz, and G. P. Wiederrecht. Structure and exciton dynamics in j aggregates studied by polarization dependent near-field scanning optical microscopy. *Journal of the American Chemical Society*, 124, 2002. doi: 10.1021/ja012263e.

[110] P. Vasa, W. Wang, R. Pomraenke, M. Lammers, M. Maiuri, C. Manzoni, G. Cerullo, and C. Lienau. Real time observation of ultrafast rabi oscillations between excitons and plasmons in metal nanostructures with j aggregates. *Nature Photonics*, 7, 2013. doi: 10.1038/nphoton.2012.340.

[111] A. R. Shah, N. F. Scherer, M. Pelton, and S. K. Gray. Ultrafast reversal of a fano resonance in a plasmon-exciton system. *Physical Review B*, 88: 075411–075418, August 2013. doi: 10.1103/PhysRevB.88.075411.

Appendix A

TABLE A.1: Dielectric permittivity of gold (Section 2.3.1)

Parameter	Symbol	Value	Reference
electrons temperature	T_e	-	-
phonons temperature	T_p	300 K	-
electrons heat capacity	C_e	67.96 [J/(K^2m^3)]*T_e	[53, 54]
phonons heat capacity	C_p	2.49^5 [J/(Km^3)]	[53]
electron-phonon coupling constant	G	2^{16}	[54]
a_{intra}	-	0.0125/h [Hz]	[28, 44]
b_{intra}	-	0.0827/h [Hz/eV^2]	[28, 42, 45, 46]
a_{inter}	-	0.15/h [Hz]	[28]
b_{inter}	-	0.7/h [Hz/eV^2]	[28]
Debye temperature	Θ	170 K	
Energy gap in Au	E_g	1.98 eV	[13]
Fermi energy in Au	E_f	2.4 eV	[13]
Transition dipole	K	1.2695 x 10^{32}	[28, 87]

TABLE A.2: Pump-probe simulations (Chapter 6, for all data that are not considered in Table A.3).

Parameter	Symbol	Value
Maximum pump power per pulse	P_0	0.1 [W]
Pulse width	σ	100 x 10^{-15} [s]
Laser repetition rate	-	1 x 10^3 [Hz]
Nanorod length	-	350 x 10^{-9} [m]
Nanorod diameter	-	30 x 10^{-9} [m]
Nanorod period	-	90 x 10^{-9} [m]

TABLE A.3: Pump-probe simulations (Figure 6.37).

Parameter	Symbol	Value
Maximum pump power per pulse	P_0	0.01 [W]
Pulse width	σ	100 x 10^{-15} [s]
Laser repetition rate	-	1 x 10^3 [Hz]
Nanorod length	-	350 x 10^{-9} [m]
Nanorod diameter	-	35 x 10^{-9} [m]
Nanorod period	-	90 x 10^{-9} [m]

TABLE A.4: Pump-probe simulations (Chapter 7).

Parameter	Symbol	Value
Maximum pump power per pulse	P_0	0.1 [W]
Pulse width	σ	100 x 10^{-15} [s]
Laser repetition rate	-	1 x 10^3 [Hz]
Nanorod length	-	250 x 10^{-9} [m]
Nanorod diameter	-	30 x 10^{-9} [m]
Nanorod period	-	80 x 10^{-9} [m]
Shell thickness	-	20 x 10^{-9} [m]